MULTISCALE STRUCTURE-FUNCTION RELATIONSHIPS IN THE MECHANICAL BEHAVIOR OF TENDON AND LIGAMENT

by

Shawn Peter Reese

A dissertation submitted to the faculty of
The University of Utah
in partial fulfillment of the requirements for the degree of

Doctor of Philosophy

Department of Bioengineering

The University of Utah

May 2012

The University of Utah Graduate School

STATEMENT OF DISSERTATION APPROVAL

The dissertation of **Shawn Peter Reese**

has been approved by the following supervisory committee members:

Jeffrey A. Weiss	, Chair	**2/28/12** Date Approved
Richard D. Rabbit	, Member	**2/28/12** Date Approved
James E. Guilkey	, Member	**2/28/12** Date Approved
Ken L. Monson	, Member	**2/28/12** Date Approved
Andrew E. Anderson	, Member	**2/28/12** Date Approved

and by **Patrick A. Tresco**, Chair of the Department of **Biomedical Engineering**

and by Charles A. Wight, Dean of The Graduate School.

ABSTRACT

Ligaments and tendons are dense, fibrous connective tissue that transmit and bear loads within the musculoskeletal system. They are elastic and viscous, and thus are capable of storing and dissipating energy. Although soft and flexible, they can interface with materials that are orders of magnitude stiffer (e.g., bone) and orders of magnitude more compliant (e.g., muscle). These functions are mediated by a complex network of hierarchically organized fibrillar collagen and accessory proteins and molecules. Tissue constituents form unique structural motifs that span the nanoscale, microscale, mesoscale and macroscale. This multiscale organization enables both a robust mechanical response at the macroscopic joint level and simultaneously provides a microscale environment conducive to cellular proliferation and nutrient transport.

The aim of this dissertation was to gain a deeper understanding of how the organization of tissue constituents contribute to mechanical function of tendon and ligament across scale levels. At the nanoscale, the question regarding the role of the proteoglycan decorin was addressed. A novel combination of an in vitro assay, imaging techniques and mechanical testing was used to explore how decorin acts to modify the strength of collagen fibril networks. At the microscale, computational modeling was used to examine how different fibril organizations contribute to the macroscopic volumetric response of tendon and ligament during tensile loading. The volumetric response is believed to drive fluid flux within the tissue, which may play a role in nutrient

transport and the apparent viscoelastic response. This flow dependent mechanism was addressed in a study that experimentally measured the volumetric changes in mesocale fascicles during viscoelastic testing. One of the challenges in discerning structure-function relationships in tendon and ligament is the large number of uncontrolled variables, which can be difficult to account for in an experimental setting. To address this challenge, a collagen based tendon surrogate was developed for use as a physical model. The physical model was coupled to a validated micromechanical computational model. This facilitated the testing of hypotheses that would have been difficult to address experimentally. The four studies contained within this dissertation, along with a number of preliminary studies, represent a novel contribution to the field of tendon and ligament mechanics.

To my family and friends,

Thank you for your encouragement and support.

TABLE OF CONTENTS

APPENDICES

LIST OF TABLES

LIST OF FIGURES

SYMBOL LEGEND

Symbol		Symbol	
$\mathbf{a}$,$\mathbf{a_0}$	Fiber direction vector	$\mathbf{n}^r$	Elliptical axis
A_r	Area ratio	N	Dimension of vector
$\mathbf{b}$	2nd order left Cauchy deformation tensor	$\mathbf{t}$	Traction vector
B	Bulk modulus	$\mathbf{S}$	2nd order second Piola-Kirchhoff stress tensor
$\mathbf{C}$	2nd order right Cauchy deformation tensor	$\mathbf{t}_0$	Prescribed traction vector
c, τ_1, τ_2	Coefficients for the relaxation function	$\mathbf{u}$	Nodal displacement vector
d	Diameter	$\mathbf{u}_0$	Prescribed nodal displacement vector
e	Euler's number	$\mathbf{v}^s$	Solid phase velocity vector
$\mathbf{e}_1$,$\mathbf{e}_2$,$\mathbf{e}_3$	Cartesian basis vectors	$\mathbf{v}^f$	Fluid phase velocity vector
Ei( )	Exponential integral	W	Strain energy function
E	Young's modulus	α	Solid phase volume fraction
$\mathbf{f}$	Nodal force vector	α_{xy}, α_{xy}, ξ_{xy}, ξ_{xy}	EFD coefficients
$\mathbf{F}$	2nd order deformation gradient tensor	$\boldsymbol{\varepsilon}$	2nd order Green Lagrange strain tensor
$\mathbf{g}$	Acceleration vector	δ	Phase shift
G	Relaxation function	(θ,φ,r) $(\Phi\ \Theta,R)$	Spherical coordinates
H_a	Aggregate modulus	ω	Angular frequency
i	Imaginary number	η	Weighting factor
j_0, j_1	Modified Bessel functions	μ	Shear modulus
$\mathbf{I}$	2nd order identity tensor	Λ	Lame coefficient
I_1, I_2, I_3, I_4, I_5	Invariants	λ	Fiber stretch
J	Jacobian	ν	Poisson's ratio
k	Isotropic permeability	$\boldsymbol{\sigma}$	2nd order Cauchy stress tensor
$\mathbf{K}$	Stiffness matrix	$\boldsymbol{\sigma}^s$	2nd order solid phase stress tensor
M^*	Complex modulus	$\boldsymbol{\sigma}^f$	2nd order fluid phase stress tensor

Symbol		Symbol	
$\boldsymbol{\pi}$	2^{nd} order drag stress tensor	$\otimes$	Outer product operator
$\chi^*(\,)$	Push forward operator	:	Inner product operator
Γ	Surface boundary	Im( )	Imaginary component
Ω	Volumetric domain	Re( )	Real component
$\mathbb{C}$	4^{th} order elasticity tensor	$\langle\,\rangle$	Average
$\mathbb{Q}$	3^{rd} order gradient of deformation gradient tensor	$\tilde{(\,)}$	Deviatoric Component
∇	Gradient operator	r	Radius

ACKNOWLEDGEMENTS

Financial support for this work was provided by the National Institute of Health Grant R01AR47369. The University of Utah Scientific Computing and Imaging Institute and the Microscopy Core Facility are also acknowledged for their contribution to this work.

CHAPTER 1

INTRODUCTION

Motivation

Ligaments and tendons are bands of aligned, collagenous connective tissue that transmit loads within the musculoskeletal system. Ligaments are defined as connective tissue that connects bone to bone, while tendons are defined as connective tissue that connects muscle to bone. Normal joint function is contingent upon normal ligament and tendon function, with tears and ruptures leading to altered joint mechanics [1, 2]. It is estimated that 15-20 million ligament injuries occur annually in the US [3]. In the US, over 200,000 ACL related injuries occur annually, leading to over 60,000 reconstructions [4]. The prevalence of tendon disorders is high. Achilles tendinopathy affects 6% of the general population and 50% of all endurance athletes, with up to 29% of tendon disorders requiring surgery [2]. Chronic tendon overuse accounts for 30% of all running related injuries, and 5 out of every 1,000 workers report tendon problems in the upper extremity [5, 6]. Tendon disorders have also been linked to a number of other health concerns, including obesity, smoking, estrogen replacement therapy and diabetes [7-10]. Genetic diseases, such as Ehlers-Danlos Syndrome (EDS), Marfan's Syndrome and Osteogenesis Imperfecta, result in mechanically weak connective tissues [11]. Injury to tendons and ligaments lead to altered gait and joint loading patterns, which creates a predisposition for

osteoarthritis [12]. It is clear that the societal impact of ligament and tendon injury and disease is immense.

In spite of considerable research effort, tendon and ligament injury remains difficult to treat [5, 13]. A ruptured ACL ligament, for instance, will not heal on its own. Although engineered replacements have been sought for decades, the current standard of care is still reconstruction with a tendon allograft or autograft [14, 15]. Repair of ruptured tendons, such as the rotator cuff, is associated with a high failure rate [16]. Chronic overuse injuries, such as Tendinitis and Tendinosis, are notoriously difficult to treat [5]. The challenge associated with treating tendon and ligament injury is due, in part, to their underlying physiology. Tendon and ligament tissue is poorly vascularized and relatively acellular [17, 18]. This leads to slow healing, if healing occurs at all. When scar tissue is formed, it is structurally different from normal tissue and mechanically inferior [19, 20].

From an engineering perspective, these tissues achieve an astounding feat. They are capable of bearing high loads, dissipate energy and can interface with materials of varying stiffness (e.g., bone and muscle). All of this is achieved while being composed of self assembled, cell excreted proteins and approximately 65%-75% water [21]. Underlying this function is a hierarchical organization of fibrillar type I collagen in combination with other ECM components [22]. At each scale level, collagen and ECM proteins are assembled into different organizational motifs. These motifs include staggered monomeric assembly at the nanometer level, crimped fibrillar organization at the micrometer level and parallel packing of fascicles at the millimeter level [22]. Interspersed within the collagen matrix at each scale level are fibroblasts, elastic fibers

and electrically charged proteoglycans and glycosaminoglycans [17]. Understanding the function of these organizational motifs, their mechanical interactions across scale levels, their interactions with noncollagenous ECM components, as well as the process of self assembly (known as fibrillogenesis) is of fundamental importance in understanding normal tissue function as well as the etiology and treatment of injury and disease.

Research Goals

The over arching goal of this work was to understand the structure-function relationships that underlie the mechanical behavior of tendon and ligament tissue. Although considerable progress has been made in attaining this understanding, significant questions still remain. The topics addressed in this dissertation were focused on tendon and ligament, but have applications to other collagenous tissues (e.g., meniscus, skin, etc.). These topics included the role of certain ECM proteins (such as proteoglycans), the structural underpinnings of the volumetric behavior during tensile loading, the biphasic contribution to the apparent viscoelasticity and the use of physical and computational models for understanding the force transmission between scale levels. These topics are formally stated by the following hypotheses:

(1) The proteoglycan decorin indirectly influences the mechanical strength of in vitro polymerized type I collagen gels by modulating the self assembly of fibrils during fibrillogenesis.

(2) The volumetric behavior (i.e., Poisson's ratio) and nonlinear stress-strain behavior of tendon and ligament can be explained by a helical organization of collagen fibrils within a crimped fiber.

(3) The apparent viscoelastic behavior of tendon fascicles is explained, at least in part, by the fluid flux dependent mechanism described by biphasic theory.

(4) A collagen based physical model of tendon coupled to an FE micromechanical model can be used to isolate and study interactions between the macroscale and the mesoscale.

To address these hypotheses, a multidisciplinary approach was required, encompassing continuum mechanics, image analysis, nonlinear optimization, finite element analysis, microscopy, instrumentation and biochemistry. In most studies, the combined approach of experimental and computational techniques was employed. Mathematical modeling was used extensively and included the use of both analytical and computational approaches. Modeling has become an indispensable tool, as it allows for certain hypotheses and questions to be addressed that would be difficult if not impossible to test experimentally. However, a model that has not been validated is of limited use [23, 24]. Therefore, a fundamental aspect of the modeling was experimental validation. The bulk of the work in this dissertation is represented by four studies that have either been published or are in the process of submission. There is also a body of work which has not yet been published. This work is contained within the preliminary studies section (Chapter 7) and the appendices.

Summary of Chapters

Tendons and ligaments are complex biological composites. Understanding how these tissues function requires a knowledge set that encompasses many disciplines. To provide this context, a background section is presented in Chapter 2. This section is intended to introduce the important concepts behind the study of tendon mechanics,

provide a summary of what is currently known and delineate the current state of the art. The multiscale organization of tendons and ligaments is discussed, with particular attention being paid to the organization of fibrillar collagen at each scale level. The organization of other ECM components and cells is also discussed. The mechanism by which collagen self organizes, known as fibrillogenesis, is then introduced. In vivo fibrillogenesis, in vitro fibrillogenesis and the regulatory role of certain proteoglycans (with a focus on decorin) is presented. Methods for experimentally characterizing tendon and ligament are reviewed, including microscopy, mechanical testing methods and optical strain measurement techniques. The elastic and viscoelastic behavior of tendon and ligament is discussed, with continuum modeling being introduced at this time. The multiscale nature of tendon mechanics and its relevance to injury and disease is then reviewed. The chapter concludes with an introduction to computational methods, including finite element (FE) analysis, computational homogenization and multiscale modeling.

Although the primary solid phase component of ligament is type I collagen, certain proteoglycans are also present in relative abundance. Chapter 3 addresses the role of decorin, which is the most abundant of the proteoglycans found in ligament and tendon. Decorin has long been thought to make a direct contribution to the mechanical function of ligament by cross linking adjacent collagen fibrils. Recent work by our lab and others has suggested that this may not be the case. Nonetheless, knockout studies in mice reveal that an absence of decorin leads to mechanically altered tendons. It was hypothesized that decorin indirectly influences the strength of ligaments by playing a regulatory role during fibrillogenesis. To test this hypothesis, in vitro experiments were

performed on collagen gels that were polymerized in the absence or presence of decorin and or its molecular components (the core protein and dermatan sulfate). Turbidity assays, electron and confocal microscopy (coupled with image analysis algorithms) as well as uniaxial tensile testing revealed that decorin, as well as the core protein and dermatan sulfate, modulated the process of fibrillogenesis. More precisely, the presence of decorin or the core protein led to the development of a fibril network that was more interconnected, which resulted in an increased modulus and tensile strength of the gels. The presence of dermatan sulfate had the opposite effect. In addition to these findings, this study introduced new methods for measuring strain in collagen gels and a new algorithm for measuring fiber diameter distributions in SEM and confocal images.

In Chapter 4, the focus is shifted to understanding the structural underpinnings of the volumetric behavior of ligament and tendon during uniaxial tension. Experimentally measured values for the Poisson's ratio in tendon and ligament range from 1.5-3 (which is large compared to the isotropic limit of 0.5) [25, 26]. This is indicative of substantial volume loss during tensile loading. This volume loss drives fluid exudation, which is thought to contribute to the apparent viscoelastic response and nutrient transport within these tissues [27, 28]. This study postulates that a helical organization of fibrils within a fiber may contribute to this large Poisson's ratio. Experimentally verifying this hypothesis is challenging, as tracking fibril trajectories along their entire length has proven to be to be difficult [29]. To address this hypothesis, a nonlinear homogenization was performed on micromechanical FE models. The fibril organization within these models was varied and included a helical organization both with and without fiber crimp. As hypothesized, a helical organization (both with and without crimp) was capable of

predicting Poisson's ratios in the range of the experimentally measured values. In addition to providing a possible structure-function mechanism for the large Poisson's ratios, this study advanced the state of the art in computational homogenization by providing a new set of periodic boundary conditions applicable to hexagonal geometry and helical coordinate systems.

The volumetric behavior of tendon and ligament is of particular interest because it drives the exudation of fluid during tensile loading, as described by biphasic theory. In Chapter 5, it was hypothesized that biphasic theory may explain the apparent viscoelastic behavior of tendon fascicles. In particular, biphasic theory predicts that during tensile stress relaxation testing, the lateral contraction (i.e., the Poisson ratio) of the sample would proceed at a rate proportional to the decay of the stress. A new method for simultaneously measuring 2D strain in tendon fascicles was introduced and utilized in this study. As predicted by biphasic theory, there was a linear correlation between the stress and the time dependent Poisson's ratio during stress relaxation testing. This suggests that some or all of the apparent viscoelastic behavior in tendon fascicles may be attributable to a biphasic response.

The macroscopic behavior of tendon and ligament is a result of complex interactions at the mesoscale, microscale and nanoscale. Unfortunately, studying structural features at different length scales has proved challenging for a number of reasons. The process of isolating an organizational structure (e.g., a fiber or fascicles) is difficult and can alter the material properties. Furthermore, tissues and their substructures are highly inhomogeneous. At the macrolevel, material properties differ between insertion sites and the midsubstance. At the mesoscale, individual fascicles have

varying material properties [30], as do fibers at the microscale [31]. These factors are likely to blame for the conflicting experimental results seen across studies [32, 33]. In Chapter 6, the use of a physical model was introduced as a means for making the study of multiscale force transmission more tractable. In this study, a collagen based tendon surrogate was created that consisted of dense collagen fibers aligned in parallel and embedded within a collagen gel, which replicated the mesoscale fascicle organization. The geometry and the material properties of the components were well defined and simple to characterize. Because of its simplicity, many of the aforementioned challenges in isolating multiscale interactions were circumvented. The utility of the physical model was greatly extended by coupling it to a 3D micromechanical finite element model. Experimental data obtained from tensile testing of the surrogate were used to validate the FE model. The validated FE model was then used in combination with the physical model to explore force transmission between the macroscale and microscale. In particular, the problem of microscale size effects was addressed. In tendon and ligament, the size of certain microstructures (e.g., fascicles and fibers) are not infinitesimally small in comparison to the macroscale, which violates the assumption of a continuum.

The physical surrogate replicated numerous features experimentally observed in tendon, including large Poisson's ratios and inhomogeneous strain at the microscale. Through the use the FE model, it was revealed that the inhomogeneity within the microscale strain field was a result of size effects in the presence of a constrained boundary. Model simulations using physiologically relevant parameters also predicted size effects, suggesting that continuum assumptions may misrepresent the microscale behavior of tendon and ligament. The results of this study revealed that tissue mimetic

physical models provide a useful platform for studying multiscale structural relationships and provide a simplified means for developing and validating increasingly complex multiscale models.

The significance of this work is discussed in Chapter 7, which places the new findings and methods in context of what has been reported and what remains to be done. The limitations of this work are also discussed. A major focus of this section, however, is preliminary data and future work related to this topic. First, a new strain energy function to describe the volumetric behavior of ligament is derived and fit to experimental test data. Following this, poroviscoelasticity is explored as a means to more fully describe the time dependent response of tendon and ligament. Finally, preliminary results from two new 3D microscopy techniques are presented and their future applications are discussed. Contained within this dissertation is also an appendix, which includes a number of mathematical derivations.

References

[1] Georgoulis, A. D., Ristanis, S., Moraiti, C. O., Paschos, N., Zampeli, F., Xergia, S., Georgiou, S., Patras, K., Vasiliadis, H. S., and Mitsionis, G., 2010, "Acl Injury and Reconstruction: Clinical Related in Vivo Biomechanics," Orthop Traumatol Surg Res, 96(8 Suppl), pp. S119-28.

[2] Fredberg, U., and Stengaard-Pedersen, K., 2008, "Chronic Tendinopathy Tissue Pathology, Pain Mechanisms, and Etiology with a Special Focus on Inflammation," Scandinavian Journal of Medicine & Science in Sports, 18(1), pp. 3-15.

[3] Frank, C. B., 1996, "Ligament Healing: Current Knowledge and Clinical Applications," J Am Acad Orthop Surg, 4(1), pp. 74-83.

[4] Surgery, A. B. O. O., 2004, "Research Committee Report," Diplomatic Newsletter, Chapel Hill, NC.

[5] Sharma, P., and Maffulli, N., 2005, "Tendon Injury and Tendinopathy: Healing and Repair," The Journal of Bone and Joint Surgery (American Volume), 87(1), pp. 187-202.

[6] Tanaka, S., Petersen, M., and Cameron, L., 2001, "Prevalence and Risk Factors of Tendinitis and Related Disorders of the Distal Upper Extremity among U.S. Workers: Comparison to Carpal Tunnel Syndrome," Am J Ind Med, 39(3), pp. 328-35.

[7] Grant, W. P., Foreman, E. J., Wilson, A. S., Jacobus, D. A., and Kukla, R. M., 2005, "Evaluation of Young's Modulus in Achilles Tendons with Diabetic Neuroarthropathy," J Am Podiatr Med Assoc, 95(3), pp. 242-6.

[8] Gill, C. S., Sandell, L. J., El-Zawawy, H. B., and Wright, R. W., 2006, "Effects of Cigarette Smoking on Early Medial Collateral Ligament Healing in a Mouse Model," J Orthop Res, 24(12), pp. 2141-9.

[9] Biancalana, A., Veloso, L. A., and Gomes, L., 2010, "Obesity Affects Collagen Fibril Diameter and Mechanical Properties of Tendons in Zucker Rats," Connect Tissue Res, 51(3), pp. 171-8.

[10] Hansen, M., Kongsgaard, M., Holm, L., Skovgaard, D., Magnusson, S. P., Qvortrup, K., Larsen, J. O., Aagaard, P., Dahl, M., Serup, A., Frystyk, J., Flyvbjerg, A., Langberg, H., and Kjaer, M., 2009, "Effect of Estrogen on Tendon Collagen Synthesis, Tendon Structural Characteristics, and Biomechanical Properties in Postmenopausal Women," J Appl Physiol, 106(4), pp. 1385-93.

[11] Tozer, S., and Duprez, D., 2005, "Tendon and Ligament: Development, Repair and Disease," Birth Defects Res C Embryo Today, 75(3), pp. 226-36.

[12] Vairo, G. L., Mcbrier, N. M., Miller, S. J., and Buckley, W. E., 2010, "Premature Knee Osteoarthritis after Anterior Cruciate Ligament Reconstruction Dependent on Autograft," J Sport Rehabil, 19(1), pp. 86-97.

[13] Woo, S. L., Debski, R. E., Zeminski, J., Abramowitch, S. D., Saw, S. S., and Fenwick, J. A., 2000, "Injury and Repair of Ligaments and Tendons," Annu Rev Biomed Eng, 2, pp. 83-118.

[14] Wipfler, B., Donner, S., Zechmann, C. M., Springer, J., Siebold, R., and Paessler, H. H., 2011, "Anterior Cruciate Ligament Reconstruction Using Patellar Tendon Versus Hamstring Tendon: A Prospective Comparative Study with 9-Year Follow-Up," Arthroscopy, 27(5), pp. 653-65.

[15] Bernardino, S., 2010, "Acl Prosthesis: Any Promise for the Future?," Knee Surg Sports Traumatol Arthrosc, 18(6), pp. 797-804.

[16] Abrams, J. S., 2010, "Management of the Failed Rotator Cuff Surgery: Causation and Management," Sports Med Arthrosc, 18(3), pp. 188-97.

[17] Kjaer, M., 2004, "Role of Extracellular Matrix in Adaptation of Tendon and Skeletal Muscle to Mechanical Loading," Physiol Rev, 84(2), pp. 649-98.

[18] Wang, J. H., 2006, "Mechanobiology of Tendon," J Biomech, 39(9), pp. 1563-82.

[19] Abramowitch, S. D., Papageorgiou, C. D., Debski, R. E., Clineff, T. D., and Woo, S. L., 2003, "A Biomechanical and Histological Evaluation of the Structure and Function of the Healing Medial Collateral Ligament in a Goat Model," Knee Surg Sports Traumatol Arthrosc, 11(3), pp. 155-62.

[20] Scheffler, S. U., Clineff, T. D., Papageorgiou, C. D., Debski, R. E., Ma, C. B., and Woo, S. L., 2001, "Structure and Function of the Healing Medial Collateral Ligament in a Goat Model," Ann Biomed Eng, 29(2), pp. 173-80.

[21] Benjamin, M., and Ralphs, J. R., 1997, "Tendons and Ligaments--an Overview," Histol Histopathol, 12(4), pp. 1135-44.

[22] Kannus, P., 2000, "Structure of the Tendon Connective Tissue," Scand J Med Sci Sports, 10(6), pp. 312-20.

[23] Anderson, A. E., Ellis, B. J., and Weiss, J. A., 2007, "Verification, Validation and Sensitivity Studies in Computational Biomechanics," Comput Methods Biomech Biomed Engin, 10(3), pp. 171-84.

[24] Henninger, H. B., Reese, S. P., Anderson, A. E., and Weiss, J. A., 2010, "Validation of Computational Models in Biomechanics," Proc Inst Mech Eng H, 224(7), pp. 801-12.

[25] Hewitt, J., Guilak, F., Glisson, R., and Vail, T. P., 2001, "Regional Material Properties of the Human Hip Joint Capsule Ligaments," J Orthop Res, 19(3), pp. 359-64.

[26] Lynch, H. A., Johannessen, W., Wu, J. P., Jawa, A., and Elliott, D. M., 2003, "Effect of Fiber Orientation and Strain Rate on the Nonlinear Uniaxial Tensile Material Properties of Tendon," J Biomech Eng, 125(5), pp. 726-31.

[27] Lavagnino, M., Arnoczky, S. P., Kepich, E., Caballero, O., and Haut, R. C., 2008, "A Finite Element Model Predicts the Mechanotransduction Response of Tendon Cells to Cyclic Tensile Loading," Biomech Model Mechanobiol, 7(5), pp. 405-16.

[28] Yin, L., and Elliott, D. M., 2004, "A Biphasic and Transversely Isotropic Mechanical Model for Tendon: Application to Mouse Tail Fascicles in Uniaxial Tension," J Biomech, 37(6), pp. 907-16.

[29] Provenzano, P. P., and Vanderby, R., Jr., 2006, "Collagen Fibril Morphology and Organization: Implications for Force Transmission in Ligament and Tendon," Matrix Biol, 25(2), pp. 71-84.

[30] Komolafe, O. A., and Doehring, T. C., 2010, "Fascicle-Scale Loading and Failure Behavior of the Achilles Tendon," J Biomech Eng, 132(2), pp. 021004.

[31] Screen, H. R. C., and Cheng, V. W. T., 2007, "The Micro-Structural Strain Response of Tendon," Journal of Material Science, 19, pp. 1-2.

[32] Atkinson, T. S., Ewers, B. J., and Haut, R. C., 1999, "The Tensile and Stress Relaxation Responses of Human Patellar Tendon Varies with Specimen Cross-Sectional Area," J Biomech, 32(9), pp. 907-14.

[33] Miyazaki, H., and Kozaburo, H., 1999, "Tensile Tests of Collagen Fibers Obtained from the Rabbit Patellar Tendon," Biomedical Microdevices, 2(2), pp. 151-157.

CHAPTER 2

BACKGROUND

Tendon and Ligament Structure

Tendons and ligaments are multiphasic, biological composites. They are composed of a fluid phase and a solid phase, with the bulk of the tissue consisting of the fluid phase (65%-75% water by weight) [1, 2]. The solid phase consists primarily of type I collagen (60%-80%), with the remainder consisting of elastin, proteoglycans and glycosaminoglycans (GAG's), other types of collagen (types III, IV, V, VI), fibrillin and other proteins [3-5]. These tissues are poorly vascularized and relatively acellular [4]. Type I Collagen is organized into a complex hierarchy, where tropocollagen monomers form fibrils at the nanoscale, fibrils form fibers at the microscale, fibers form fascicles at the mesoscale, and fascicles form the whole tendon or ligament at the macroscale (Fig 2.1) [3, 6, 7]. Unique structural motifs are present at each scale level (Fig 2.2).

At the nanometer length scale, tropocollagen monomers are assembled into fibrils, which display a characteristic d-banding pattern. The period of this banding is created by a ¾ overlap of the tropocollagen monomers. Although reported values vary slightly between tissue types, the d-banding period is generally accepted to be 67 nm [8, 9].

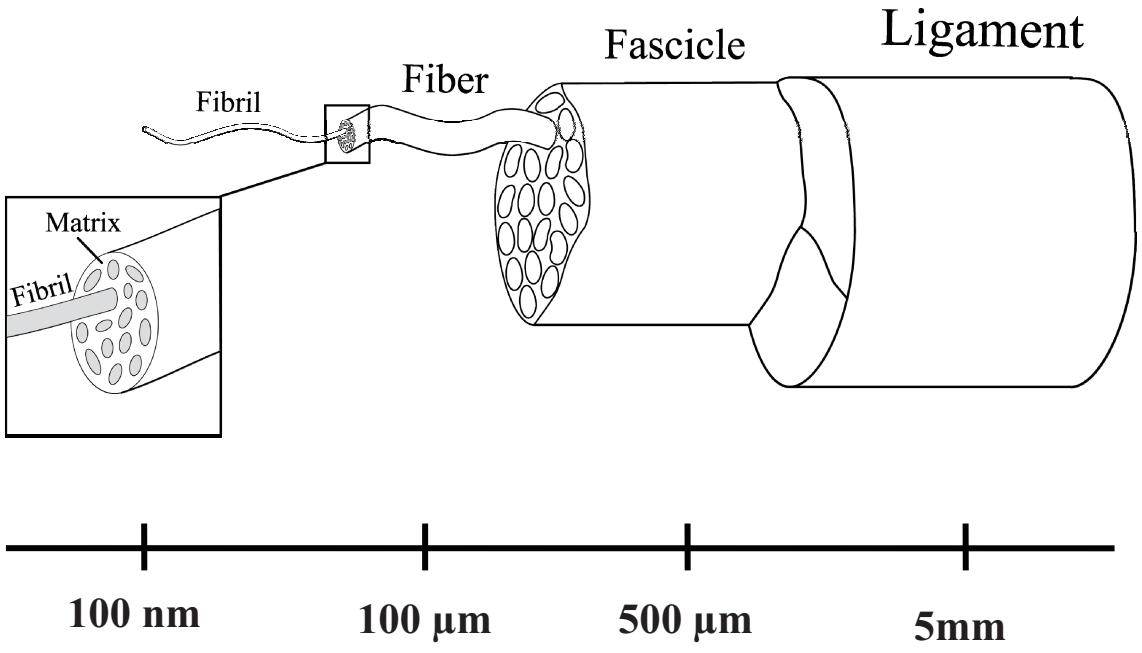

Figure 2.1: Ligament and tendon structure. At the nanoscale, collagen fibrils are regularly organized within an interfibrillar matrix. At the microscale, these fibrils organize to form fibers, which is where the characteristic crimp pattern is seen. At the mesoscale, fibers assemble to form fascicles. The macroscale is composed of groups of aligned fascicles.

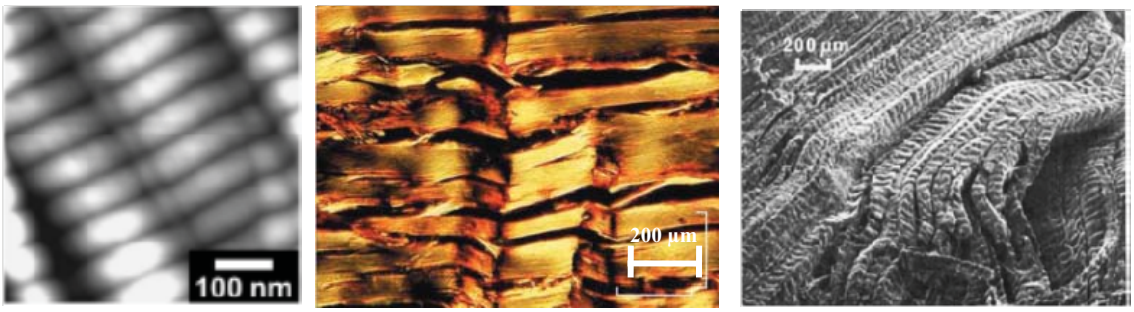

Figure 2.2: Unique structural motifs exist at each scale level. At the nanoscale, 67 nm d-banding is observed (Left) [9], at the microscale fiber crimp is present (Middle) [10] and at the macroscale fascicles align in a parallel fashion (right) [6]. Note that crimp is generally in register within fascicles.

Tropocollagen monomers are held together by a combination of hydrogen, ionic and covalent bonds [4, 5]. Experimental evidence suggests that fibrils are composed of subfibrils and microfibrils. However, the precise organization of tropocollagen is still unclear [8, 11]. Fibril diameter varies from tissue to tissue and even within tissues (e.g., insertion site vs. midsubstance), but have typical values ranging from 50-200 nm [3, 11]. Cross sectional TEM images reveal that fibrils are well organized and separated by a regular spacing within healthy tissue (Fig 2.3). Fibrils are predominantly aligned in a parallel fashion. However, limitations in microscopy techniques have made the study of their longitudinal organization difficult. Although it's been suggested that fibrils are continuous, evidence suggests that they may intertwine, split, merge and may have a helical organization [12-14].

At the microscale fibrils are assembled to form fibers, which have diameters ranging from 20-50 um [6, 15]. Fibroblasts (referred to as tenocytes in tendon) are located within the interfiber space (Fig 2.4).

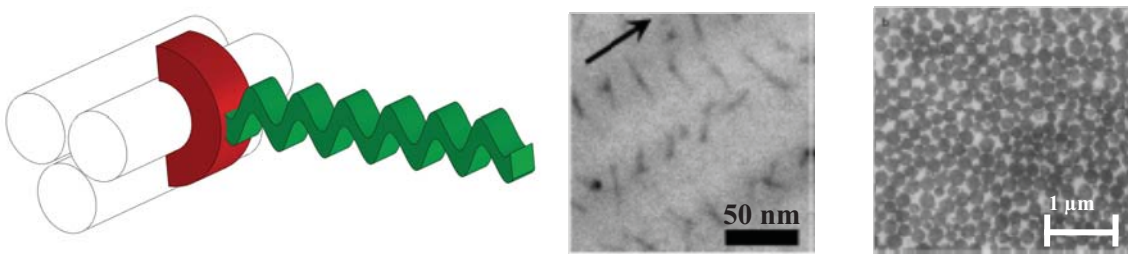

Figure 2.3: Decorin and fibril organization. (Left) Decorin consists of a core protein (red) and a dermatan sulfate side chain (green). The horseshoe shaped core protein binds to collagen on the surface of fibrils (white cylinders). (Center) A TEM image of a longitudinal ligament section stained with cupromeronic blue reveals the presence of dermatan sulfate, which is aligned perpendicular to fibrils within the interfiber space. The arrow indicates the fibril direction [16]. (Right) A TEM image of a transverse ligament section reveals a regular fibril diameter and interfiber spacing [17].

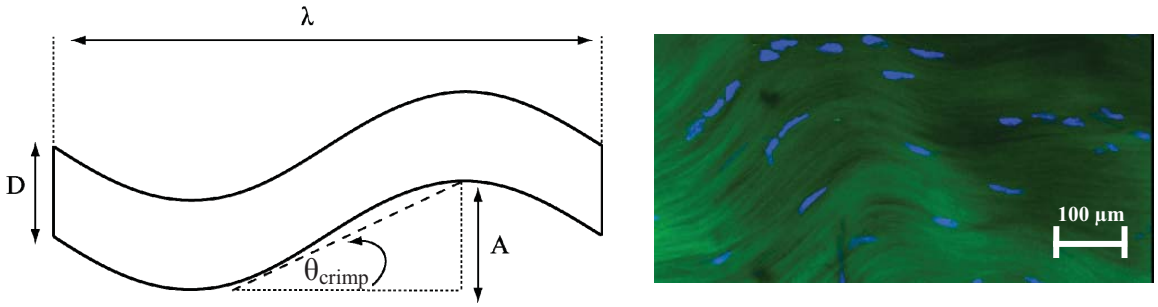

Figure 2.4: Fiber crimp. (Left) Fiber crimp is characterized by a wavelength (λ), a crimp angle (θ), an amplitude, A, and the diameter, D. (Right) Fibroblasts are located between individual crimped fibers. In this confocal image of a rat tail tendon fascicle, the cell nuclei are stained blue while the collagen is shown in green.

It is at the fiber level where the characteristic crimp pattern first takes shape. Crimping is a ubiquitous phenomenon in tendon and ligament tissue and is defined by a crimp period and crimp angle (Fig 2.4). Crimp periods typically range from 50 to 200 um, depending on the tissue [15, 18] . The crimp angle is more difficult to define, as histological preparations often result in shrinking and thus an altered crimp angle. However, crimp angles likely range between 10-60 degrees [3]. Fibers are arranged in a largely parallel fashion. However, considerable branching and merging appears to be present [3].

At the mesoscale, fibers are assembled into fascicles. Fascicle diameters range from 100-500 μm [3, 5, 6]. Crimp patterns are clearly visible at the fascicle level, indicating that fiber crimp is, to a certain extent, in register. However, studies from as early as the 70s indicate that a purely planar crimping pattern is not consistent with experimental observations [7, 19]. The precise crimping pattern is still not known. Fascicles are organized in parallel, and quite possibly span the entire bone-bone (for

ligament) or muscle-bone (for tendon) length [20]. Fascicles and fibers are surrounded by a thin fascia (referred to as endotenon), which is composed of disorganized collagen fibrils and other ECM constituents [3, 21, 22].

At the macroscale, groups of fascicles are organized into functional bands, with a diameter ranging from hundreds of micrometers to millimeters [6]. In the literature, these bands are often called fascicles as well. The number of bands varies from tissue to tissue. The MCL, for instance, has three functional bands [23]. Finally, these functional bands are assembled into the whole tendon or ligament unit. Surrounding the tendon or ligament is the epitenon [5] .

Although present in relatively small quantities (0.5%-3%), proteoglycans are believed to play an important role in tendon and ligament mechanics. The most abundant of these are the small leucine rich proteoglycans, such as decorin (~1%/wt), biglycan (~0.5%/wt) and others (fibromodulin, lumican, aggrecan, versican) [4, 24]. Decorin is the most well studied of these. Structurally, decorin consists of a core protein covalently bonded to the GAG dermatan sulfate (DS) (Fig 2.3). The decorin core protein binds the surface of collagen fibrils. Previously, it was believed that cross linking between adjacent fibrils was mediated via the DS side chains. However, recent evidence suggests that this is likely not the case [25, 26]. Nonetheless, knockout studies in mice reveal that an absence of decorin leads to altered fibrillar organization and a decrease in mechanical properties [27, 28]. It has been suggested that decorin may influence mechanical properties indirectly by regulating fibril organization during fibrillogenesis, which is supported by in vivo and in vitro evidence [29, 30]. How decorin performs this action, and to what extent, is unknown. It has been suggested that biglycan plays a similar role

in facilitating the organization of collagen, but its role is less clear. Fibromodulin and lumican have not been extensively investigated. However, studies suggest that they are capable of binding collagen fibrils, and thus they may influence fibrillar assembly as well [29, 31]. Although their role remains unclear, GAGs such as aggrecan and versican are present in small quantities and may play roles in maintaining tissue hydration via osmotic swelling [32].

Structural proteins that have seen relatively little study in tendon and ligament are elastin and fibrillin. Elastin, which occurs at 1-2% by dry weight, is found in the form of elastic fibers [3, 4]. In mature tissue, elastic fibers (d~2 um) consist of a core of amorphous elastin covered in microfibrils, which are 10-12 nm fibrils composed of fibrillin [3, 33]. Microfibrils also occur independent of elastin and are often called oxytalin fibers. Histology and immunostaining reveal that elastic fibers are sparsely populated within the interfiber space, running parallel, oblique and transverse to the fiber direction [21]. Elastic fibers are found in higher concentrations in the endotenon, which surrounds fascicles. Elastin is found in larger quantities in tissues such as arterial walls and skin, where a high level of compliance is necessary [34]. The role that elastin plays in ligament and tendon is largely unknown and unexplored. Oxytalin (fibrillin) microfibrils are found in relative abundance in the interfiber space. However, they do not appear to co-localize with elastic fibers [21]. As with elastic fibers, their mechanical function is unknown.

Although not the focus of this dissertation, the cellular components of tendon and ligament will also be discussed, as they are the components responsible for regulating the ECM in response to loading and injury. Fibroblasts (called tenocytes in tendon) are

located between fibers, having approximate dimensions of 10 um in width and 60 um in length [3]. Fibroblasts are responsible for repairing damaged collagen fibers as well as the regular turnover of collagen. It is well established that mechanotransduction plays a major role in the cellular function of fibroblasts [35]. Since fibroblasts are located in the interfiber space, the local microscopic strain seen within these fibers is of particular importance. In order for fibroblasts to function, they need a supply of nutrients. Tendons and ligament are vascularized, but not to the extent of other tissues. Some ligaments, such as the interior region of the ACL, appear to be largely avascular [1]. Passive diffusion of nutrients may play an important role. However, active fluid transport has been suggested as well. The mechanism of this fluid transport is described by biphasic theory and will be elaborated on in a following section [36].

A final note is in order regarding the difference between tendons and ligaments. Structurally, they share the same hierarchical organization and structural motifs. However, differences have been reported. These differences include fibril diameter distributions, fiber diameter and crimp morphologies, metabolic activity and the relative percentage of certain components such as water, proteoglycans and types I and III collagen [3, 4, 37, 38]. It is important to note that structure and composition not only vary between tendons and ligaments, but also vary between ligament and tendon locations and within individual tendons and ligaments [1, 3, 23].

Fibrillogenesis

The process by which collagen self assembles is known as fibrillogenesis. Fibrillogenesis has been studied primarily by the use of vitro assays, typically via the polymerization of a type I collagen hydrogel. The starting solution for these tests is a

dilute (< 1% by weight) solution of acid solubilized type I collagen in phosphate buffered saline (PBS). The solution is neutralized, which causes the collagen to precipitate out of solution. As it precipitates, it polymerizes to form collagen fibrils. During polymerization, increased scattering from the forming of collagen fibrils causes measurable changes in turbidity. In vitro, collagen polymerization occurs in three distinct phases (as measured by turbidity). These phases include the lag phase, the growth phase and the plateau phase [39]. During the lag phase, nucleation sites begin to form. Once a critical concentration is reached, these nucleation sites begin growing both laterally and longitudinally (the growth phase), eventually forming a fibril network (the plateau phase) [40, 41]. The precise mechanisms by which fibrillogenesis occurs are still poorly understood. It has been suggested that collagen first assembles into microfibrils, which further assemble into the fibril unit [41, 42]. The resultant three-dimensional network consists of d-banded fibrils with diameters ranging from 20-200 nm [43, 44], which further assembly into fibril aggregates. The diameter, fibril length and degree of aggregation are highly sensitive to the conditions present during polymerization. These factors include pH, temperature, collagen concentration, salt concentration and the presence of other proteins or molecules [45]. In order for fibrils to form, a solution must have a minimum concentration of collagen and it appears that phosphate may be necessary for normal fibril formation [46]. It has been suggested that phosphate bridges facilitate the alignment of tropocollagen monomers. Turbidity is a useful indicator of fibril structure, with less turbid gels having finer fibrils [47]. The mechanical strength of collagen gels is highly dependent on the collagen concentration and the resulting fibril network [45, 48]. In vitro studies have provided a convenient means for examining the

effect of different proteins on the process of fibrillogenesis. For instance, decorin has been found to decrease the amount of fibril aggregation as compared to controls [49, 50]. The study of fibrillogenesis in vivo is much more challenging and relies on indirect techniques, such as genetic knockouts and microscopy throughout the different stages of development [27, 28]. Such studies have revealed that in vivo fibrillogenesis begins with the formation of small diameter collagen fibrils, which first grow in length, and then laterally merge [14, 29]. The presence of proteoglycans (e.g., decorin) has found to be concurrent with such processes [28].

Microscopy of Tendon and Ligament

Imaging structural features at different scale levels requires the use of optical, confocal, electron and atomic force microscopy. Optical transmission microscopy is useful for observing mesoscale and microscale features, such as fascicular organization, cell nuclei and fibrillar organization. Hematoxalin and Eosin (HE) staining is used to visualize collagen and nuclear structures, while Verhoeff's staining is used to visualize elastic fibers [51]. Confocal imaging is used to image microscale features using fluorescence, either via autofluorescence (e.g., collagen) or fluorescent stains [52]. Nuclear stains are used to visualize fibroblasts [4, 53], while immunostaining has been used to observe certain proteins, such as fibrillin and elastin [21]. Laser scanning confocal imaging is an inherently 3D technique. However, the high density and scattering properties of collagen within tendon and ligament make similar methods, such as 2nd harmonic imaging, attractive [54]. Confocal fluorescence imaging has been utilized for investigating microscale strains in both tendon fascicles and in vitro polymerized collagen gels [53, 55, 56]. Scanning electron microscopy is used to

visualize microscale and nanoscale features such as collagen fascicles, fibers and fibrils [6, 57, 58]. By combining multiple fields of view, SEM has been used to trace the course of single fibrils [57]. Transmission electron microscopy is used to visualize nanoscale features, such as fibril diameter and spacing [17, 59]. Certain ECM molecules, such as the GAG dermatan sulfate, can be stained and visualized using TEM [16, 60] (Fig 2.3). One drawback to electron microscopy techniques is the need to dehydrate samples, which can alter the structure being observed. For TEM, the samples must be embedded and sectioned, which may lead to further structural alterations. Atomic force microscopy (AFM) has been used to observe the topology of single collagen fibrils, revealing the d-banding patterns, the surface shape of fibril tips, noncollagenous components as well as the topography and organization of type I collagen gels [9, 61-63].

Mechanical Testing of Tendon and Ligament

To quantify the stress-strain response of tendon and ligament, mechanical testing is utilized. Since these tissues are primarily subjected to tensile loading in vivo, uniaxial tensile testing in the fiber direction is most frequently performed [64]. However, tensile testing transverse to the fiber direction, shear testing and compression testing has been reported [65-68]. Common to all test types are the need to grip the sample, measure strain and cross sectional area, control the testing environment and utilize a proper testing protocol.

When mechanically testing tendons and ligament, the method used for clamping the samples is of considerable importance. The bony insertions for ligaments can be utilized for clamping, either by directly gripping the bones or potting a bone plug in epoxy [2, 69-71]. Although this method is useful for characterizing whole ligament

mechanics, obtaining information regarding the constitutive response of the tissue is problematic. Material properties differ between the insertion sites and the midsubstance and even within functional bands [72-74]. A common approach for obtaining a homogenous test specimen is to cut a sample of tissue from the midsubstance using straight edge razors or a dog bone punch [25, 67]. The sample is then gripped using toothed tissue clamps. One challenge with this approach is gripping the sample, so sand paper is often used (without or without the use of a cyanoacrylate adhesive) to aid in gripping the tissue [75, 76]. An alternative approach, especially applicable to large tendons, is the use of a freeze clamp. A freeze clamp is chilled with dry ice, liquid nitrogen or a thermoelectric cooler, which hardens the tissue and facilitates gripping [77].

It has been experimentally observed that the tissue strain in the midsubstance is typically less than the applied strain. Thus, optical strain measurement methods must be utilized if the true stress-strain response is to be measured [78]. Optical methods include tracking of individual markers and pattern matching algorithms (e.g., texture correlation). Markers can been glued on with cyanoacrylate, made from Verhoeff's stain or sprayed on using acrylic paint [76, 79]. Markerless tracking methods using digital image correlation are also used [80, 81]. The use of optical methods allows the measurement of 2D strain (longitudinal and transverse strain), which can be used for examining the volumetric behavior (e.g., measurement of the Poisson's ratio).

Another considerable challenge is measuring the sample cross sectional area, which is necessary for stress calculations. The simple use of calipers may be sufficient if the sample is planar [25]. Optical methods, such as laser micrometers and image based techniques, have been used [76, 82]. Real time measurement of the cross sectional area

using laser scanning techniques has been reported for the testing of flexor tendons [83-85].

Since tendon and ligament are highly hydrated, the testing environment is of considerable importance. Larger tissue specimens are often tested in air. This has several advantages, such as allowing the use of a freeze clamp or a laser micrometer for cross sectional area measurement. The disadvantages are the potential for tissue dehydration and difficulty in controlling the temperature of the test environment. Testing in PBS is common; however ligament and tendon swelling can be problematic [26]. Testing has also been performed in a humidity chamber [86]. The material properties of tendon and ligament are temperature dependent, and thus testing in PBS provides the ability for controlling bath temperature [87].

A phenomenon common to all biological tissues is the presence of hysteresis. This necessitates the need to include a preconditioning phase prior to testing. This consists of a cyclic application of stress or displacement, a step displacement and subsequent relaxation period, or a combination of the two. Although the origin of this hysteresis is not clear, it may result from the release of prestrain that is present within tendons and ligaments in situ [64]. This prestrain (evidenced by a recoil when tendons and ligament are cut), may align the fibers. It has been suggested that preconditioning may act to realign the fibers [88, 89]. A number of different testing protocols are performed, including constant strain rate testing, incremental stress relaxation testing, creep testing and harmonic testing [2, 25, 26]. Since these tissues are viscoelastic, the strain rate is of considerable importance, with higher strain rates resulting in stiffer behavior and slower strain rates resulting in more compliant behavior [64]. Incremental

stress relaxation testing consists of applying a preset strain in increments and then holding at this strain level until the stress has decayed to the level determined by the equilibrium elastic behavior. Creep testing is similar; however incremental force levels are applied and the strain is allowed to equilibrate. Harmonic testing consists of applying sinusoidal strains of varying frequencies (typically at the end of a stress relaxation test). This allows for the loss modulus and dynamic modulus to be tested in a frequency dependent manner [90].

Elastic Behavior of Tendon and Ligament

The 3D quasistatic (i.e., equilibrium elastic) behavior of tendon and ligament is complex and difficult to fully characterize. These tissues are generally assumed to be transversely isotropic, with the axis of symmetry being defined by the predominant collagen fiber direction [64, 91]. The tensile stress-strain response in the fiber direction is nonlinear and consists of a toe region and a linear region (Fig 2.5). The tensile stress-strain response transverse to the fiber direction is nearly linear and has a stiffness that is several orders of magnitude less than the fiber direction. The stress-strain response in shear testing is highly nonlinear, as is the response when tested in unconfined compression [67, 92, 93] (Fig 2.5). The experimentally measured Poisson's ratios are between 1-3, which greatly exceeds the isotropic limit of 0.5 [73, 75].

The 3D stress-strain behavior is traditionally modeled using a continuum approach. Although these tissues are highly nonlinear, concepts from the theory of linear elasticity provide useful insights. For a linear transversely isotropic material, a total of 5 independent coefficients are required. These coefficients include the fiber modulus (E_1),

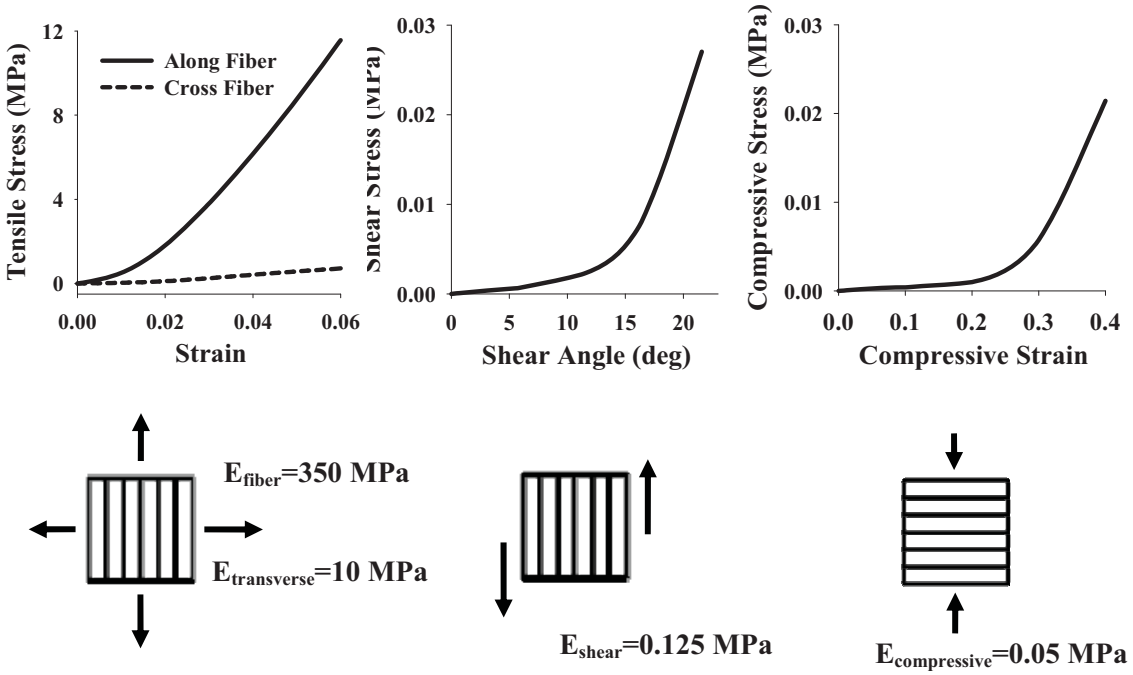

Figure 2.5: The elastic behavior of ligament is anisotropic and nonlinear. The tensile stiffness along the fiber direction is an order of magnitude stiffer than in the transverse direction (left). In shear, ligament is two orders of magnitude more compliant than in the transverse direction (center). In compression, ligament is over three times more compliant than in tension, indicating compression-tension nonlinearity (right).

transverse fiber modulus (E_2), two Poisson's ratios (ν_{12}, ν_{13}) and a shear modulus, where $\mathbf{e}_1$ is the fiber direction. The permissible values for these coefficients are determined by the requirement that the elasticity tensor remains positive definite, and allows for Poisson's ratios in excess of the isotropic limit [94].

When addressing nonlinearity, strain energy approaches (referred to as hyperelasticity) based on the invariants of the deformation tensor (I_1, I_2, I_3, I_4, I_5), are commonly utilized. Such an approach is particularly attractive because it automatically satisfies a number of constraints, such that the formulation will be objective (i.e., invariant to rigid body rotation and displacement) and the tangent elasticity tensor (i.e.,

the linearization) will be positive definite for a polyconvex strain energy function [95]. Of these approaches, both coupled and uncoupled formulations have been presented. An uncoupled formulation is based on decomposing the stress and strain into volumetric and isochoric (or deviatoric) components. This formulation is particularly well suited for addressing the common assumption of incompressibility. When a biphasic material is loaded at a high strain rate, the fluid does not have time to exude, making the volumetric behavior of the tissue take on the incompressible behavior of the fluid phase [96]. This assumption is valid for high loading rates, which is representative of in vivo conditions during many activities. One such formulation, which has been successful in modeling the stress-strain behavior in the fiber direction, is given by the following strain energy equation [91]:

$$W(\tilde{\lambda},\tilde{I}_1)=\frac{c_1}{2}(\tilde{I}_1-1)+W_f\left(\tilde{\lambda}\right)+\frac{K}{2}\left[\ln(J)\right]^2 \tag{2.1}$$

$$\tilde{\lambda}\frac{\partial W_{f2}}{\partial\tilde{\lambda}}=\begin{Bmatrix} 0 & \tilde{\lambda}\le 1 \\ c_2\left(e^{c_3\left(\tilde{\lambda}-1\right)}-1\right) & 1<\tilde{\lambda}<\tilde{\lambda}^* \\ c_4\tilde{\lambda}+c_5 & \tilde{\lambda}\ge\tilde{\lambda}^* \end{Bmatrix} \tag{2.2}$$

where $\tilde{I}_1$ is the 1st deviatoric invariant of the right Cauchy deformation tensor **C**, $\tilde{\lambda}$ is the deviatoric fiber stretch along the fiber direction, which is defined as $\tilde{\lambda}=\sqrt{\tilde{I}_4}$, J is the Jacobian (or volume ratio) and K is the bulk modulus. The fiber strain energy term (W_f) is defined using its derivative relative to the fiber stretch, as it provides for an easier implementation in computing the stress from the strain energy function. For the assumption of incompressibility, the bulk modulus is given a large value (e.g., the value

of water). This is an example of a structurally motivated formulation, as it consists of a nonlinear fiber term and an isotropic matrix term. The fiber term captures the nonlinear toe region via the constants c_2 and c_3, and the linear region via the constants c_4 and c_5. The matrix term captures the transverse and shear behavior via c_1. Expressions for the stress-strain response are obtained by taking a first order derivative of the strain energy function:

$$\mathbf{S} = 2\frac{\partial W}{\partial \mathbf{C}} \tag{2.3}$$

where $\mathbf{S}$ is the 2nd Piola-Kirchhoff stress tensor, which is in the spatial (or reference) frame, and $\mathbf{C}$ is the right Cauchy deformation tensor. The Cauchy stress tensor can be obtained by performing a push forward into the material frame (See Appendix C). The elasticity tensor is found by taking a second order derivative of the strain energy function:

$$\mathbb{C} = 4\frac{\partial^2 W}{\partial \mathbf{C} \partial \mathbf{C}} \tag{2.4}$$

where $\mathbb{C}$ is the fourth ordered spatial elasticity tensor, which can be transformed to the material frame via a push forward. Generalized results for the above equations are available in the literature [91]. This formulation captures the stress-strain response in the fiber direction for situations of fast loading. If a more realistic shear behavior is desired, the matrix term could be replaced with a more appropriate formulation [67]. The tension compression nonlinearity present in these tissues (Fig 2.5) could also be included with an appropriate matrix term [97]. Such a formulation has been particularly amenable to finite

element modeling, as the decoupled volumetric response can be utilized to enforce incompressibility via the use of Lagrange multipliers. This overcomes the issue of volumetric locking, which is problematic in standard FE implementations when an incompressible material is being simulated [98].

Although such a formulation has proved useful for modeling in vivo behavior at high loading rates [96], it does possess several shortcomings. Because of the deviatoric split, it cannot accommodate the experimentally observed large Poisson's ratios seen during quasistatic loading. A fully coupled formulation can be created which can account for this (see Preliminary Studies in Chapter 7). By adding new terms when appropriate, a structurally motivated strain energy based continuum approach is capable of capturing many of the complex material behaviors experimentally observed in tendon and ligament.

Viscoelastic Behavior of Tendon and Ligament

Tendons and ligaments display time dependent (viscoelastic) behaviors. These behaviors include hysteresis during loading and unloading, stress relaxation in response to a step displacement, creep in response to a step loading, strain rate dependent modulus (dynamic modulus) and damping (loss modulus) as well as "memory" to the loading history [26, 99-103]. This behavior is attributed to a solid phase component (e.g., caused by a viscous fibrillar sliding), and/or a fluid phase component (e.g., caused by fluid flux within the tissue). Regardless of the source, tissue viscoelasticity is believed to play an important role in absorbing energy during loading [86].

Tendon and ligament viscoelasticity is most commonly modeled using a solid phase theory. Representations include discrete element models, quasilinear viscoelastic (QLV) models and nonlinear viscoelastic models. Discrete element models, such as a

Kelvin solid (a spring and a spring-dashpot in parallel), are applied to whole tendon or ligament simulations. In continuum theory, QLV models are most commonly used. QLV theory postulates that the time response and the elastic response are independent, and thus can be described via a multiplicative split. In this split, the time response is described using a relaxation function which is convolved with the stress response. The most general formulation is given by:

$$\boldsymbol{\sigma}(t,\varepsilon) = \int_{t=0}^{t} G(t-\tau)\frac{\partial \boldsymbol{\sigma}(\varepsilon)}{\partial \boldsymbol{\varepsilon}} : \frac{\partial \boldsymbol{\varepsilon}}{\partial \tau} d\tau \tag{2.5}$$

where the Cauchy stress $\boldsymbol{\sigma}(\varepsilon)$ is given by an appropriate constitutive model, $\frac{\partial \boldsymbol{\varepsilon}}{\partial \tau}$ is the strain rate tensor and the time response is given by a relaxation function, G(t). G(t) is generally taken to be a scalar (i.e., isotropic viscoelasticity); however a stress relaxation tensor could be defined for an anisotropic viscoelastic response. In practical terms, the relaxation function is the stress relaxation curve obtained from an instantaneous step displacement. A relaxation function proposed by Fung is commonly used [99]:

$$G(t) = \frac{1 + c\left[Ei(t/\tau_2) - Ei(t/\tau_1)\right]}{1 + c\ln(\tau_1/\tau_2)} \tag{2.6}$$

where Ei is the exponential integral function, defined as:

$$Ei(y) = \int_{y}^{\infty} \frac{e^{-x}}{x} dx \tag{2.7}$$

The relaxation function can be converted to a dynamic modulus (the real part of the complex modulus) and the damping (the imaginary part of the loss modulus). For this relaxation function, the damping is approximately constant for frequencies between $1/\tau_2$ and $1/\tau_1$ [90]. This allows for a constant damping over several decades of frequency, which is consistent with the experimental observations that hysteresis is relatively independent of strain rate [104]. Although strain independence is commonly assumed in the stress relaxation function, several studies suggest that this may not be an accurate assumption [100], [105]. According to linear viscoelastic theory, the relaxation function is implicitly related to the creep function via a convolution [106]. Thus, an experimentally measured relaxation function should predict an experimentally measured creep function. Several studies suggest this is not the case; thus nonlinear viscoelastic models have been proposed to account for this [107].

The apparent viscoelasticity of ligament and tendon can also be described using biphasic theory. Biphasic theory postulates an interaction between a porous, incompressible elastic solid phase and an incompressible fluid phase. The total stress is defined as the sum of the elastic and fluid stress components:

$$\boldsymbol{\sigma} = \boldsymbol{\sigma}^s + \boldsymbol{\sigma}^f \tag{2.8}$$

The equilibrium equations for the solid and fluid phase are given by:

$$\begin{aligned} \nabla \cdot \boldsymbol{\sigma}^s &= -\boldsymbol{\pi} \\ \nabla \cdot \boldsymbol{\sigma}^f &= \boldsymbol{\pi} \end{aligned} \tag{2.9}$$

where $\boldsymbol{\pi}$ is a term that represents the drag force that couples the fluid and solid phase. The statement of the conservation of mass is given by the continuity equation:

$$\nabla \cdot \left(\mathbf{v}^f + \alpha \mathbf{v}^s \right) = 0 \tag{2.10}$$

where $\mathbf{v}^s$ and $\mathbf{v}^f$ are the solid and fluid phase velocities and α is the ratio of solid volume to fluid volume. The solid phase stress, fluid phase stress and drag stress are specified via an appropriate constitutive model. To obtain quasianalytic solutions, a number of simplifications are often made, including the use of linear elasticity, an inviscid Newtonian fluid and a linear form for the drag:

$$\boldsymbol{\pi} = \frac{\left(\mathbf{v}^s - \mathbf{v}^f \right)}{k\left(1+\alpha\right)} \tag{2.11}$$

in which k is the isotropic permeability. Quasianalytic solutions to these equations have only been presented for simplified geometries and loading scenarios. These include confined and unconfined loading of a cylinder subjected to ramp loading, step loading and harmonic loading for isotropic and transversely isotropic linear elastic materials [108, 109] and certain nonlinear materials [110, 111]. In biphasic theory, fluid flux is driven by the volumetric behavior of the solid phase, with fluid exudation being caused by volume loss of the solid phase and fluid influx being caused by a volume gain of the solid phase. Stress relaxation, creep and hysteresis are all predicted by biphasic theory; thus it may potentially explain the apparent viscoelastic behavior of tendon and ligament. Of central importance in biphasic theory is properly modeling the volumetric behavior of the elastic solid phase. In practice, this volumetric behavior is driven by the Poisson's ratio of the tissue. Incremental stress relaxation data from tendon fascicles can be accurately

described using biphasic theory [112]. The optimized coefficients resulted in Poisson's ratios of 2.3, which is consistent with experimentally measured values in macroscopic tissue samples [75]. While QLV can describe stress relaxation behavior using a 1D formulation, biphasic theory is inherently 3D, where stress relaxation is only predicted in response to a lateral strain and a resulting volume change. This presents the opportunity to perform experimental validation in multiple dimensions, which is presented in Chapter 5. One of the drawbacks for biphasic theory is that analytical solutions only exist for simple geometries and loading condition. If complicated geometries, material properties and loading conditions are to be simulated, numerical methods must be used.

It has been suggested that a both solid and fluid dependent mechanism may be needed to fully describe the apparent viscoelasticity of these tissues. Poroviscoelastic formulations have been proposed that utilize a viscoelastic continuum model within the solid phase. This method has been found utility in the field of cartilage mechanics [97, 111, 113]. Refer to Chapter 7 for preliminary results regarding the application of poroviscoelasticity to ligament.

Multiscale Properties of Ligament and Tendon

Although continuum based approaches are useful for modeling the macroscopic behavior of tendon and ligament, they fail to address the multiscale nature of these tissues. There are three trademarks of multiscale behavior that are experimentally observed. First, the stiffness of the tissue depends on which scale level is being tested. Although conflicting behavior has been reported [69, 81, 114-116], it appears that single fascicles are stiffer than macroscopic tissue. The second trademark is an inhomogeneous strain field in response to homogeneous loading, which is not predicted by continuum

theories [55, 117]. Neither fascicles within a tendon nor fibers within a fascicle respond homogeneously. The third trademark is the significance of microstructural size effects in the presence of a constrained boundary [118, 119]. Fibers and fascicles are only one or two orders of magnitude smaller than the whole ligament or tendon. This violates the continuum assumption of microstructures being infinitely small compared to the macroscale.

Understanding the multiscale behavior of tendon and ligament is particularly important, as these behaviors may be responsible for many of the functional properties of these tissues. Tendon damage and failure appears to occur at the fascicle and fiber level [120-122]. Furthermore, the rupture of individual fascicles may lead to stress shielding of damaged tissue, which may have important implications regarding chronic tendon disease such as tendinitis [20, 81]. Another important consideration is that vascularization and innervation occurs at the mesoscale level, with vessels growing in between fascicles [4, 123]. At the microscale, strains observed at the fiber level are inhomogeneous, which may protect fibroblasts from excessive strain while still facilitating mechanotransduction [53, 117].

Computational Modeling

Analytical stress-strain expressions can only be obtained for simplified geometries and loading (e.g., uniaxial loading of a rectangle). For complex geometries and loading patterns (e.g., simulation of an MCL within a knee joint), the geometry and governing equations must be discretized and solved numerically. A formal statement of a problem in elasticity includes the equations of motion in combination with the appropriate boundary conditions:

$$\nabla \cdot \boldsymbol{\sigma}(\mathbf{u}) - \mathbf{g} = 0 \text{ in } \Omega \tag{2.12}$$

$$\begin{aligned} \mathbf{u} &= \mathbf{u}_0 \\ \boldsymbol{\sigma}(\mathbf{u}) \cdot \mathbf{n} &= \mathbf{t}_0 \end{aligned} \text{ on } \Gamma \tag{2.13}$$

where Ω is a volume in space bounded by the surface Γ. The stress $\boldsymbol{\sigma}(\mathbf{u})$, is specified by a constitutive model and is a function of displacement, while $\mathbf{g}$ represents body forces (e.g., gravity). A well posed problem must include boundary conditions on the surface of the domain, which include displacement boundary conditions $\mathbf{u_0}$ and/or traction boundary conditions, $\mathbf{t_0}$. The displacement enters the constitutive stress model via a strain measure (e.g., engineering strain for linear theory, the deformation gradient for nonlinear theory). The strain or deformation gradient takes the form of a first order partial derivative with respect to the spatial coordinates. With this substitution into the constitutive model, Equations 2.12 and 2.13 result in a system of coupled partial differential equations. The domain (e.g., the simulation geometry) is discretized using a 3D set of points called nodes. Most methods (including the finite element method) require that these nodes form a conformal mesh consisting of elements. The governing equations are then discretized and solved at the nodal points. A number of computational methods are used to solve the discretized equations, including the finite element method, finite volume method, boundary element method, finite difference method and the material point method. The finite element method is used extensively in the field of biomechanics. The finite element method utilizes shape functions that interpolate the unknown nodal displacements over an element domain. The shape functions, in combination with the constitutive model for the stress, are used to define a so called stiffness matrix, $\mathbf{K}$, for the

element. The stiffness matrix for each element is assembled, creating a global stiffness matrix. For linear elasticity, the problem takes the following form:

$$\mathbf{K}\mathbf{u} = \mathbf{f} \tag{2.14}$$

where **K** is the global stiffness matrix (NxN), **u** is a vector assembled from all of the unknown nodal displacements (N) and **f** is a vector consisting of all the known forces (N), where N is the total degrees of freedom (e.g., unknowns) in the system. Note that **K** is singular until boundary conditions are applied. Two kinds of nonlinearity can be introduced into the system: geometric nonlinearity and material nonlinearity. Geometric nonlinearity requires the use of an objective strain measure (e.g., the Green Lagrange strain, which is a function of the deformation gradient, **F**). For the nonlinear case, the finite element problem must be solved using optimization methods. In this case, the solution is found by minimizing the residual between the applied nodal loads (determined from applied tractions and displacements to the boundary) and the nodal reaction forces:

$$\begin{aligned} &\min\left(\mathbf{f}\left(\mathbf{u}\right)-\mathbf{f}_0\right) \\ &\mathbf{u}\in\mathbb{R} \end{aligned} \tag{2.15}$$

where a nonlinear optimization routine is employed to find the set of unknown nodal displacement, **u**, that minimize the residual. Newton's method is commonly employed, which utilizes the following difference equation:

$$\mathbf{u}^{m+1} = \mathbf{u}^{m} - \left(\mathbf{K}\left(\mathbf{u}\right)^{m}\right)^{-1}\left(\mathbf{f}\left(\mathbf{u}\right)^{m} - \mathbf{f}_0\right) \tag{2.16}$$

where $\mathbf{u}^m$ is the vector of the estimated nodal displacements, $\mathbf{f}(\mathbf{u})^m$ is computed from the stress update and $\mathbf{K}(\mathbf{u})^m$ is the stiffness update. When the residual is zero (within a specified tolerance), the problem has converged to the solution $\mathbf{u}^M$, where M is the final number of iterations. For a more in depth discussion regarding finite element theory, refer to the references [124, 125]. Numerous software packages are available that provide a means for preprocessing (generating a mesh and applying boundary conditions), solving and postprocessing (visualize/extracting results) finite element problems. Hundreds of studies are present in the literature that utilize FE models for the simulation of ligament and tendon mechanics (e.g., [98, 126, 127]). In addition to elastic problems, the finite element method can also be used to solve viscoelastic problems and biphasic problems. The finite element method has also been applied to homogenization and multiscale modeling techniques, which are described in the following section.

Computational Homogenization and Multiscale Modeling

Homogenization is the process of obtaining a macroscopic stress-strain response from a material with a known heterogeneous microstructure. A representative volume element is defined that is large enough to be statistically representative of the material microstructure, but still satisfies the continuum assumption of being much smaller than the macroscale dimension [128]. For the case of a perfectly periodic microstructure (e.g., a lattice of spherical particles), the representative volume element reduces to a unit cell. For a periodic unit cell, the exact homogenized effective material properties are obtained. For a statistically representative volume element, the so called apparent material properties are obtained [129, 130]. The concept of a homogenization is based upon the Hill principle [131]:

$$\langle \boldsymbol{\sigma} : \boldsymbol{\varepsilon} \rangle = \langle \boldsymbol{\sigma} \rangle : \langle \boldsymbol{\varepsilon} \rangle \tag{2.17}$$

which states that the volume averaged strain energy at the macroscale is equal to the volume averaged strain energy at the microscale (i.e., energy is conserved). To satisfy the Hill condition, special boundary conditions are required. For a periodic unit cell, this takes the form of so called periodic boundary conditions, which states that opposing faces of the unit cell must deform identically and that the traction forces on opposing faces must be antiperiodic [132]:

$$\begin{aligned} \mathbf{u}^{k+}\left(\mathbf{x}^{+}\right) - \mathbf{u}^{k-}\left(\mathbf{x}^{-}\right) &= \varepsilon_0\left(\mathbf{x}^{+} - \mathbf{x}^{-}\right) \\ \mathbf{t}^{k+}\left(\mathbf{x}^{+}\right) &= -\mathbf{t}^{k-}\left(\mathbf{x}^{-}\right) \end{aligned} \quad \text{on } \Gamma \tag{2.18}$$

where $\mathbf{u}^{k+}$ and $\mathbf{u}^{k-}$ are the displacements on opposing faces and $\mathbf{t}^{k+}$ and $\mathbf{t}^{k-}$ are traction forces on opposing faces (both on the boundary Γ), ε_0 is the applied strain and $\mathbf{x}^{+}$ and $\mathbf{x}^{-}$ are the position vectors on opposing faces. For RVE's with simple geometry, analytic approaches have been employed (for a comprehensive summary of these approaches, see [133]) . Analytical approaches lack the ability to address the complex 3D microstructural features seen in tendon and ligament [133]. Thus, finite element based methods are particularly appealing. For a properly discretized RVE, the finite element method can be used to perform the homogenization. To obtain a full set of material coefficients (in the linear case) a sufficient number of loading conditions (e.g., tensile testing in orthogonal directions and shear testing in orthogonal shearing directions) must be applied to obtain the unique material coefficients. For a unit cell with an orthotropic symmetry (as in [134]) a total of 6 unique loading simulations must be performed to obtain the 9

independent coefficients within the elasticity tensor. For a finite element simulation, the periodic displacement boundary conditions (Equation 2.18) must be explicitly enforced [135]. This can be done by converting the periodic boundary equations into a set of linear constraint equations (e.g., via a master node approach) within the FE solver. It is of note that periodic boundary conditions require that a mesh has identical nodal distributions on opposing faces and edges (i.e., are conformal). For homogenizations that utilize a representative volume element that does not have conformal faces, other permissible boundary conditions must be used. These include kinematic boundary conditions, traction boundary conditions and mixed boundary conditions [130]. For these cases, the resulting homogenization is not exact, leading to the so called apparent material properties.

The discussion thus far has concerned the homogenization of linear materials. However, the use of a unit cell and periodic boundary conditions can also be applied to nonlinear materials [136]. In this case, a simple stiffness tensor is no longer applicable. This makes obtaining a homogenized material response more difficult. Strain energy based approaches have been proposed, including an approach based on the generation and interpolation of lookup tables. In this approach, a large number of simulations are performed to populate the six dimensional strain energy function space W(**C**), where **C** is the right Cauchy deformation tensor [137]. Once populated, cubic splines are then used to compute the 1^{st} and 2^{nd} order derivatives for the stress and tangent stiffness computations.

As an alternative to these approaches, computational multiscale modeling has been proposed. This method, also referred to as FE^2, utilizes a nested FE problem (Fig

2.6). Every time the macroscale problem needs to evaluate the stress or tangent stiffness (e.g., at an integration point) a homogenization is performed on an RVE [138, 139]. This method allows the established methods of a linear homogenization to be applied to nonlinear problems. Currently, the most significant limitation of this method is the computational demand. Every time stress is evaluated at an integration point, multiple microscale FE problems must be solved. It is clear that even small simulations will be computationally demanding. Parallelization methods have been proposed which significantly decrease computational time [140].

For linear, nonlinear and multiscale homogenization approaches, a fundamental assumption is that the RVE is infinitesimally small in comparison to the macroscale. When this assumption is valid, homogenization methods are referred to as 1st order methods.

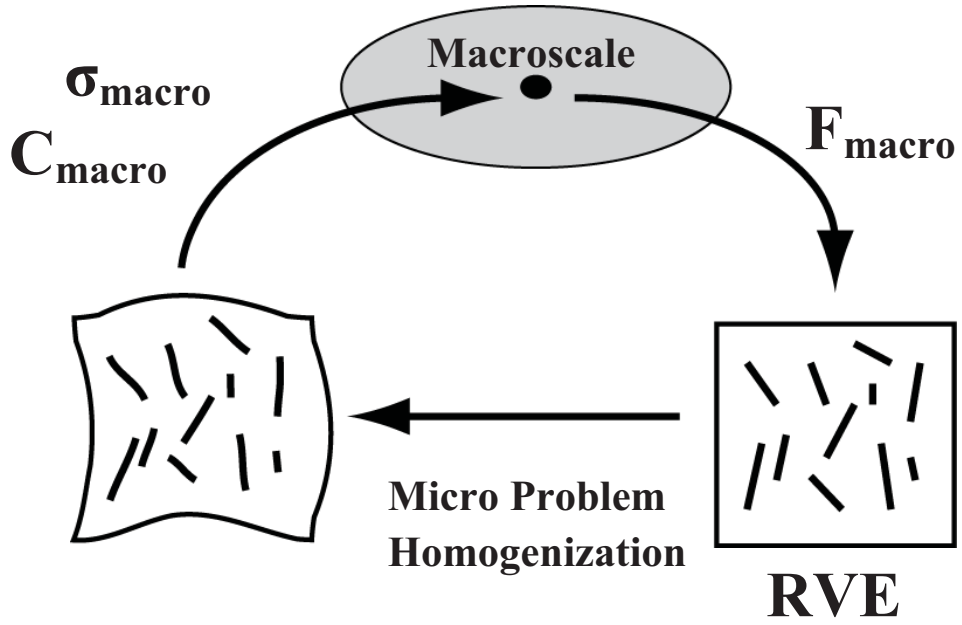

Figure 2.6: FE^2 homogenization procedure. The FE^2 method solves a nested FE problem in which the deformation gradient computed at a macroscale point is passed to the microscale RVE. A homogenization is performed using suitable boundary conditions, and the resulting stress tensor and stiffness tensor are passed back to the macroscale.

However, some homogenization problems feature RVE's that do not satisfy this requirement. In these cases, microstructural size effects must be taken into account [118, 119]. Several methods have been proposed for taking size effects into consideration, including the use of generalized continua [141, 142] and 2nd order homogenization methods [118]. In either case, the gradient of the deformation gradient, $\mathbb{Q} = \nabla \mathbf{F}$ (where $\mathbb{Q}$ is a third order tensor), is used to account for the scale effects. The most generalized approach is to utilize 2nd order FE^2 strategies. In these methods, a microscale RVE problem is still used. However, the homogenization utilizes both the deformation gradient and the gradient of the deformation gradient for the computation of the stress and tangent stiffness. Second order methods are particularly attractive for biological materials, as scale separation is not well defined (e.g., fascicles are not infinitesimally small in comparison to the macroscale).

Multiscale modeling is relevant to tendon and ligament, as the function of these tissues is driven by their multiscale organization. The RVE concept provides a tool for linking force transmission across scale levels. The use of nested FE^2 simulations is particularly powerful, as it dynamically links macroscale and microscale strains. This allows joint level forces to be translated to lower scale levels. However, the use of multiscale modeling in biological tissue is in its infancy. At present, only a few 1D analytic models have been proposed for tendon [143-145], while several FE^2 approach have been utilized for modeling fibrillar mechanics of type I collagen gels [146, 147]. No computational multiscale models (e.g., FE^2) have been applied to tendon or ligament. It is clear that ample opportunity exists for advancement of the field in this regard.

References

[1] Benjamin, M., and Ralphs, J. R., 1997, "Tendons and Ligaments--an Overview," Histol Histopathol, 12(4), pp. 1135-44.

[2] Thornton, G. M., Shrive, N. G., and Frank, C. B., 2001, "Altering Ligament Water Content Affects Ligament Pre-Stress and Creep Behaviour," J Orthop Res, 19(5), pp. 845-51.

[3] Kannus, P., 2000, "Structure of the Tendon Connective Tissue," Scand J Med Sci Sports, 10(6), pp. 312-20.

[4] Kjaer, M., 2004, "Role of Extracellular Matrix in Adaptation of Tendon and Skeletal Muscle to Mechanical Loading," Physiol Rev, 84(2), pp. 649-98.

[5] Wang, J. H., 2006, "Mechanobiology of Tendon," J Biomech, 39(9), pp. 1563-82.

[6] Danylchuk, K. D., Finlay, J. B., and Krcek, J. P., 1978, "Microstructural Organization of Human and Bovine Cruciate Ligaments," Clin Orthop Relat Res, (131), pp. 294-8.

[7] Kastelic, J., Galeski, A., and Baer, E., 1978, "The Multicomposite Structure of Tendon," Connect Tissue Res, 6(1), pp. 11-23.

[8] Ottani, V., Raspanti, M., and Ruggeri, A., 2001, "Collagen Structure and Functional Implications," Micron, 32(3), pp. 251-60.

[9] Venturoni, M., Gutsmann, T., Fantner, G. E., Kindt, J. H., and Hansma, P. K., 2003, "Investigations into the Polymorphism of Rat Tail Tendon Fibrils Using Atomic Force Microscopy," Biochem Biophys Res Commun, 303(2), pp. 508-13.

[10] Franchi, M., Fini, M., Quaranta, M., De Pasquale, V., Raspanti, M., Giavaresi, G., Ottani, V., and Ruggeri, A., 2007, "Crimp Morphology in Relaxed and Stretched Rat Achilles Tendon," J Anat, 210(1), pp. 1-7.

[11] Ottani, V., Martini, D., Franchi, M., Ruggeri, A., and Raspanti, M., 2002, "Hierarchical Structures in Fibrillar Collagens," Micron, 33(7-8), pp. 587-96.

[12] Vidal, D. C., 2003, "Image Analysis of Tendon Helical Superstructure Using Interference and Polarized Light Microscopy," Micron, 34(8), pp. 423-432.

[13] Starborg, T., Lu, Y., Huffman, A., Holmes, D. F., and Kadler, K. E., 2009, "Electron Microscope 3d Reconstruction of Branched Collagen Fibrils in Vivo," Scand J Med Sci Sports, 19(4), pp. 547-52.

[14] Birk, D. E., Zycband, E. I., Woodruff, S., Winkelmann, D. A., and Trelstad, R. L., 1997, "Collagen Fibrillogenesis in Situ: Fibril Segments Become Long Fibrils as the Developing Tendon Matures," Dev Dyn, 208(3), pp. 291-8.

[15] Jarvinen, T., Jarvinen, T. L., Kannus, P., Jozsa, L., and Jarvinen, M., 2004, "Collagen Fibres of the Spontaneously Ruptured Human Tendons Display Decreased Thickness and Crimp Angle," Journal of Orthopaedic Research, 22(6), pp. 1303-1309.

[16] Henninger, H. B., Maas, S. A., Underwood, C. J., Whitaker, R. T., and Weiss, J. A., 2007, "Spatial Distribution and Orientation of Dermatan Sulfate in Human Medial Collateral Ligament," J Struct Biol, 158(1), pp. 33-45.

[17] Lavagnino, M., Arnoczky, S. P., Frank, K., and Tian, T., 2005, "Collagen Fibril Diameter Distribution Does Not Reflect Changes in the Mechanical Properties of in Vitro Stress-Deprived Tendons," J Biomech, 38(1), pp. 69-75.

[18] Hurschler, C., Provenzano, P. P., and Vanderby, R., Jr., 2003, "Scanning Electron Microscopic Characterization of Healing and Normal Rat Ligament Microstructure under Slack and Loaded Conditions," Connect Tissue Res, 44(2), pp. 59-68.

[19] Niven, H., Baer, E., and Hiltner, A., 1982, "Organization of Collagen Fibers in Rat Tail Tendon at the Optical Microscope Level," Coll Relat Res, 2(2), pp. 131-42.

[20] Haraldsson, B. T., Aagaard, P., Qvortrup, K., Bojsen-Moller, J., Krogsgaard, M., Koskinen, S., Kjaer, M., and Magnusson, S. P., 2008, "Lateral Force Transmission between Human Tendon Fascicles," Matrix Biol, 27(2), pp. 86-95.

[21] Smith, K. D., Vaughan-Thomas, A., Spiller, D. G., Innes, J. F., Clegg, P. D., and Comerford, E. J., 2011, "The Organisation of Elastin and Fibrillins 1 and 2 in the Cruciate Ligament Complex," J Anat, 218(6), pp. 600-7.

[22] Gotoh, T., Murashige, N., and Yamashita, K., 1997, "Ultrastructural Observations on the Tendon Sheath of the Rat Tail," J Electron Microsc (Tokyo), 46(3), pp. 247-52.

[23] Robinson, J. R., Bull, A. M., and Amis, A. A., 2005, "Structural Properties of the Medial Collateral Ligament Complex of the Human Knee," J Biomech, 38(5), pp. 1067-74.

[24] Ilic, M. Z., Carter, P., Tyndall, A., Dudhia, J., and Handley, C. J., 2005, "Proteoglycans and Catabolic Products of Proteoglycans Present in Ligament," Biochem J, 385(Pt 2), pp. 381-8.

[25] Lujan, T. J., Underwood, C. J., Henninger, H. B., Thompson, B. M., and Weiss, J. A., 2007, "Effect of Dermatan Sulfate Glycosaminoglycans on the Quasi-Static Material Properties of the Human Medial Collateral Ligament," J Orthop Res, 25(7), pp. 894-903.

[26] Lujan, T. J., Underwood, C. J., Jacobs, N. T., and Weiss, J. A., 2009, "Contribution of Glycosaminoglycans to Viscoelastic Tensile Behavior of Human Ligament," J Appl Physiol, 106(2), pp. 423-31.

[27] Robinson, P. S., Huang, T. F., Kazam, E., Iozzo, R. V., Birk, D. E., and Soslowsky, L. J., 2005, "Influence of Decorin and Biglycan on Mechanical Properties of Multiple Tendons in Knockout Mice," J Biomech Eng, 127(1), pp. 181-5.

[28] Zhang, G., Ezura, Y., Chervoneva, I., Robinson, P. S., Beason, D. P., Carine, E. T., Soslowsky, L. J., Iozzo, R. V., and Birk, D. E., 2006, "Decorin Regulates Assembly of Collagen Fibrils and Acquisition of Biomechanical Properties During Tendon Development," J Cell Biochem, 98(6), pp. 1436-49.

[29] Banos, C. C., Thomas, A. H., and Kuo, C. K., 2008, "Collagen Fibrillogenesis in Tendon Development: Current Models and Regulation of Fibril Assembly," Birth Defects Res C Embryo Today, 84(3), pp. 228-44.

[30] Scott, J. E., 1988, "Proteoglycan-Fibrillar Collagen Interactions," Biochem J, 252(2), pp. 313-23.

[31] Neame, P. J., Kay, C. J., Mcquillan, D. J., Beales, M. P., and Hassell, J. R., 2000, "Independent Modulation of Collagen Fibrillogenesis by Decorin and Lumican," Cell Mol Life Sci, 57(5), pp. 859-63.

[32] Lujan, T. J., Dalton, M. S., Thompson, B. M., Ellis, B. J., and Weiss, J. A., 2007, "Effect of Acl Deficiency on Mcl Strains and Joint Kinematics," Journal of Biomechanical Engineering, 129(3), pp. 386-92.

[33] Rosenbloom, J., 1982, "Elastin: Biosynthesis, Structure, Degradation, and Role in Disease Processes," Connective Tissue Research, 10, pp. 73-91.

[34] Ushiki, T., 2002, "Collagen Fibers, Reticular Fibers and Elastic Fibers. A Comprehensive Understanding from a Morphological Viewpoint," Arch Histol Cytol, 65(2), pp. 109-26.

[35] Wang, C. J., Walker, P. S., and Wolf, B., 1973, "The Effects of Flexion and Rotation on the Length Patterns of the Ligaments of the Knee," Journal of Biomechanics, 6, pp. 587-596.

[36] Adeeb, S., Ali, A., Shrive, N., Frank, C., and Smith, D., 2004, "Modelling the Behaviour of Ligaments: A Technical Note," Comput Methods Biomech Biomed Engin, 7(1), pp. 33-42.

[37] Amiel, D., Frank, C., Harwood, F., Fronek, J., and Akeson, W., 1984, "Tendons and Ligaments: A Morphological and Biochemical Comparison," Journal of Orthopaedic Research, 1(3), pp. 257-265.

[38] Rumian, A. P., Wallace, A. L., and Birch, H. L., 2007, "Tendons and Ligaments Are Anatomically Distinct but Overlap in Molecular and Morphological Features--a Comparative Study in an Ovine Model," J Orthop Res, 25(4), pp. 458-64.

[39] Na, G. C., Butz, L. J., and Carroll, R. J., 1986, "Mechanism of in Vitro Collagen Fibril Assembly. Kinetic and Morphological Studies," J Biol Chem, 261(26), pp. 12290-9.

[40] Brightman, A. O., Rajwa, B. P., Sturgis, J. E., Mccallister, M. E., Robinson, J. P., and Voytik-Harbin, S. L., 2000, "Time-Lapse Confocal Reflection Microscopy of Collagen Fibrillogenesis and Extracellular Matrix Assembly in Vitro," Biopolymers, 54(3), pp. 222-34.

[41] Cisneros, D. A., Hung, C., Franz, C. M., and Muller, D. J., 2006, "Observing Growth Steps of Collagen Self-Assembly by Time-Lapse High-Resolution Atomic Force Microscopy," J Struct Biol, 154(3), pp. 232-45.

[42] Forgacs, G., Newman, S. A., Hinner, B., Maier, C. W., and Sackmann, E., 2003, "Assembly of Collagen Matrices as a Phase Transition Revealed by Structural and Rheologic Studies," Biophys J, 84(2 Pt 1), pp. 1272-80.

[43] Silver, F. H., Freeman, J. W., and Seehra, G. P., 2003, "Collagen Self-Assembly and the Development of Tendon Mechanical Properties," J Biomech, 36(10), pp. 1529-53.

[44] Raub, C. B., Suresh, V., Krasieva, T., Lyubovitsky, J., Mih, J. D., Putnam, A. J., Tromberg, B. J., and George, S. C., 2007, "Noninvasive Assessment of Collagen Gel Microstructure and Mechanics Using Multiphoton Microscopy," Biophys J, 92(6), pp. 2212-22.

[45] Roeder, B. A., Kokini, K., Sturgis, J. E., Robinson, J. P., and Voytik-Harbin, S. L., 2002, "Tensile Mechanical Properties of Three-Dimensional Type I Collagen Extracellular Matrices with Varied Microstructure," J Biomech Eng, 124(2), pp. 214-22.

[46] Mertz, E. L., and Leikin, S., 2004, "Interactions of Inorganic Phosphate and Sulfate Anions with Collagen," Biochemistry, 43(47), pp. 14901-12.

[47] Kaya, M., Toyama, Y., Kubota, K., Nodasaka, Y., Ochiai, M., Nomizu, M., and Nishi, N., 2005, "Effect of DNA Structure on the Formation of Collagen-DNA Complex," Int J Biol Macromol, 35(1-2), pp. 39-46.

[48] Roeder, B. A., Kokini, K., and Voytik-Harbin, S. L., 2009, "Fibril Microstructure Affects Strain Transmission within Collagen Extracellular Matrices," J Biomech Eng, 131(3), pp. 031004.

[49] Iwasaki, S., Hosaka, Y., Iwasaki, T., Yamamoto, K., Nagayasu, A., Ueda, H., Kokai, Y., and Takehana, K., 2008, "The Modulation of Collagen Fibril Assembly and Its Structure by Decorin: An Electron Microscopic Study," Arch Histol Cytol, 71(1), pp. 37-44.

[50] Raspanti, M., Viola, M., Sonaggere, M., Tira, M. E., and Tenni, R., 2007, "Collagen Fibril Structure Is Affected by Collagen Concentration and Decorin," Biomacromolecules, 8(7), pp. 2087-91.

[51] Smith, L. J., and Fazzalari, N. L., 2006, "Regional Variations in the Density and Arrangement of Elastic Fibres in the Anulus Fibrosus of the Human Lumbar Disc," J Anat, 209(3), pp. 359-67.

[52] Benjamin, M., Kaiser, E., and Milz, S., 2008, "Structure-Function Relationships in Tendons: A Review," J Anat, 212(3), pp. 211-28.

[53] Screen, H. R., Lee, D. A., Bader, D. L., and Shelton, J. C., 2004, "An Investigation into the Effects of the Hierarchical Structure of Tendon Fascicles on Micromechanical Properties," Proc Inst Mech Eng [H], 218(2), pp. 109-19.

[54] Houssen, Y. G., Gusachenko, I., Schanne-Klein, M. C., and Allain, J. M., 2011, "Monitoring Micrometer-Scale Collagen Organization in Rat-Tail Tendon Upon Mechanical Strain Using Second Harmonic Microscopy," J Biomech, 44(11), pp. 2047-52.

[55] Screen, H. R. C., and Cheng, V. W. T., 2007, "The Micro-Structural Strain Response of Tendon," Journal of Material Science, 19, pp. 1-2.

[56] Vader, D., Kabla, A., Weitz, D., and Mahadevan, L., 2009, "Strain-Induced Alignment in Collagen Gels," PLoS One, 4(6), pp. e5902.

[57] Provenzano, P. P., and Vanderby, R., Jr., 2006, "Collagen Fibril Morphology and Organization: Implications for Force Transmission in Ligament and Tendon," Matrix Biol, 25(2), pp. 71-84.

[58] Yahia, L. H., and Drouin, G., 1989, "Microscopical Investigation of Canine Anterior Cruciate Ligament and Patellar Tendon: Collagen Fascicle Morphology and Architecture," J Orthop Res, 7(2), pp. 243-51.

[59] Baek, G. H., Carlin, G. J., Vogrin, T. M., Woo, S. L., and Harner, C. D., 1998, "Quantitative Analysis of Collagen Fibrils of Human Cruciate and Meniscofemoral Ligaments," Clin Orthop Relat Res, (357), pp. 205-11.

[60] Henninger, H. B., Maas, S. A., Shepherd, J. H., Joshi, S., and Weiss, J. A., 2009, "Transversely Isotropic Distribution of Sulfated Glycosaminoglycans in Human Medial Collateral Ligament: A Quantitative Analysis," J Struct Biol, 165(3), pp. 176-83.

[61] Raspanti, M., Alessandrini, A., Ottani, V., and Ruggeri, A., 1997, "Direct Visualization of Collagen-Bound Proteoglycans by Tapping-Mode Atomic Force Microscopy," J Struct Biol, 119(2), pp. 118-22.

[62] Raspanti, M., Congiu, T., and Guizzardi, S., 2001, "Tapping-Mode Atomic Force Microscopy in Fluid of Hydrated Extracellular Matrix," Matrix Biol, 20(8), pp. 601-4.

[63] Raspanti, M., Congiu, T., and Guizzardi, S., 2002, "Structural Aspects of the Extracellular Matrix of the Tendon: An Atomic Force and Scanning Electron Microscopy Study," Arch Histol Cytol, 65(1), pp. 37-43.

[64] Weiss, J. A., and Gardiner, J. C., 2001, "Computational Modeling of Ligament Mechanics," Crit Rev Biomed Eng, 29(3), pp. 303-71.

[65] Weiss, J. A., 2000, "Behavior of Human Medial Collateral Ligament in Unconfined Compression," Othopaedic Research Society 46th Annual Meeting, Orlando, FL.

[66] Weiss, J. A., France, E. P., Bagley, A. M., and Blomstrom, G., 1992, "Measurement of 2-D Strains in Ligaments under Uniaxial Tension," Trans 38th Meeting Orthop Res Soc, 17(2), pp. 662.

[67] Weiss, J. A., Gardiner, J. C., and Bonifasi-Lista, C., 2002, "Ligament Material Behavior Is Nonlinear, Viscoelastic and Rate-Independent under Shear Loading," Journal of Biomechanics, 35, pp. 943-950.

[68] Bonifasi-Lista, C., Lake, S. P., Small, M. S., and Weiss, J. A., 2003, "Multiaxial Viscoelastic Properties of the Human Mcl," 49th Annual Orthopaedic Research Society Meeting, 28, pp. 808.

[69] Atkinson, T. S., Ewers, B. J., and Haut, R. C., 1999, "The Tensile and Stress Relaxation Responses of Human Patellar Tendon Varies with Specimen Cross-Sectional Area," J Biomech, 32(9), pp. 907-14.

[70] Abramowitch, S. D., Papageorgiou, C. D., Debski, R. E., Clineff, T. D., and Woo, S. L., 2003, "A Biomechanical and Histological Evaluation of the Structure and Function of the Healing Medial Collateral Ligament in a Goat Model," Knee Surg Sports Traumatol Arthrosc, 11(3), pp. 155-62.

[71] Woo, S. L.-Y., Gomez, M. A., Seguchi, Y., Endo, C. M., and Akeson, W. H., 1983, "Measurement of Mechanical Properties of Ligament Substance from a Bone-Ligament-Bone Preparation," Journal of Orthopaedic Research, 1, pp. 22-29.

[72] Butler, D. L., Guan, Y., Kay, M. D., Cummings, J. F., Feder, S. M., and Levy, M. S., 1992, "Location-Dependent Variations in the Material Properties of the Anterior Cruciate Ligament," Journal of Biomechanics, 25(5), pp. 511-518.

[73] Hewitt, J., Guilak, F., Glisson, R., and Vail, T. P., 2001, "Regional Material Properties of the Human Hip Joint Capsule Ligaments," J Orthop Res, 19(3), pp. 359-64.

[74] Thomopoulos, S., Williams, G. R., Gimbel, J. A., Favata, M., and Soslowsky, L. J., 2003, "Variation of Biomechanical, Structural, and Compositional Properties Along the Tendon to Bone Insertion Site," J Orthop Res, 21(3), pp. 413-9.

[75] Lynch, H. A., Johannessen, W., Wu, J. P., Jawa, A., and Elliott, D. M., 2003, "Effect of Fiber Orientation and Strain Rate on the Nonlinear Uniaxial Tensile Material Properties of Tendon," J Biomech Eng, 125(5), pp. 726-31.

[76] Lake, S. P., Miller, K. S., Elliott, D. M., and Soslowsky, L. J., 2009, "Effect of Fiber Distribution and Realignment on the Nonlinear and Inhomogeneous Mechanical Properties of Human Supraspinatus Tendon under Longitudinal Tensile Loading," J Orthop Res, 27(12), pp. 1596-602.

[77] Kiss, M. O., Hagemeister, N., Levasseur, A., Fernandes, J., Lussier, B., and Petit, Y., 2009, "A Low-Cost Thermoelectrically Cooled Tissue Clamp for in Vitro Cyclic Loading and Load-to-Failure Testing of Muscles and Tendons," Med Eng Phys, 31(9), pp. 1182-6.

[78] Lujan, T. J., Lake, S. P., Plaizier, T. A., Ellis, B. J., and Weiss, J. A., 2005, "Simultaneous Measurement of Three-Dimensional Joint Kinematics and Ligament Strains with Optical Methods," J Biomech Eng, 127(1), pp. 193-7.

[79] Elliott, D. M., and Setton, L. A., 2001, "Anisotropic and Inhomogeneous Tensile Behavior of the Human Anulus Fibrosus: Experimental Measurement and Material Model Predictions," J Biomech Eng, 123(3), pp. 256-63.

[80] Doehring, T. C., Kahelin, M., and Vesely, I., 2009, "Direct Measurement of Nonuniform Large Deformations in Soft Tissues During Uniaxial Extension," J Biomech Eng, 131(6), pp. 061001.

[81] Komolafe, O. A., and Doehring, T. C., 2010, "Fascicle-Scale Loading and Failure Behavior of the Achilles Tendon," J Biomech Eng, 132(2), pp. 021004.

[82] Moon, D. K., Abramowitch, S. D., and Woo, S. L., 2006, "The Development and Validation of a Charge-Coupled Device Laser Reflectance System to Measure the Complex Cross-Sectional Shape and Area of Soft Tissues," J Biomech, 39(16), pp. 3071-5.

[83] Pokhai, G. G., Oliver, M. L., and Gordon, K. D., 2009, "A New Laser Reflectance System Capable of Measuring Changing Cross-Sectional Area of Soft Tissues During Tensile Testing," J Biomech Eng, 131(9), pp. 094504.

[84] Vergari, C., Pourcelot, P., Holden, L., Ravary-Plumioen, B., Laugier, P., Mitton, D., and Crevier-Denoix, N., 2010, "A Linear Laser Scanner to Measure Cross-Sectional Shape and Area of Biological Specimens During Mechanical Testing," J Biomech Eng, 132(10), pp. 105001.

[85] Vergari, C., Pourcelot, P., Holden, L., Ravary-Plumioen, B., Gerard, G., Laugier, P., Mitton, D., and Crevier-Denoix, N., 2011, "True Stress and Poisson's Ratio of Tendons During Loading," J Biomech, 44(4), pp. 719-24.

[86] Bonifasi-Lista, C., Lake, S. P., Small, M. S., and Weiss, J. A., 2005, "Viscoelastic Properties of the Human Medial Collateral Ligament under Longitudinal, Transverse and Shear Loading," J Orthop Res, 23(1), pp. 67-76.

[87] Huang, C. Y., Wang, V. M., Flatow, E. L., and Mow, V. C., 2009, "Temperature-Dependent Viscoelastic Properties of the Human Supraspinatus Tendon," J Biomech, 42(4), pp. 546-9.

[88] Schatzmann, L., Brunner, P., and Staubli, H. U., 1998, "Effect of Cyclic Preconditioning on the Tensile Properties of Human Quadriceps Tendons and Patellar Ligaments," Knee Surg Sports Traumatol Arthrosc, 6 Suppl 1, pp. S56-61.

[89] Sverdlik, A., and Lanir, Y., 2002, "Time-Dependent Mechanical Behavior of Sheep Digital Tendons, Including the Effects of Preconditioning," J Biomech Eng, 124(1), pp. 78-84.

[90] Lakes, R. S., 2009, *Viscoelastic Materials*, Cambridge University Press, New York, NY.

[91] Weiss, J. A., Maker, B. N., and Govindjee, S., 1996, "Finite Element Implementation of Incompressible, Transversely Isotropic Hyperelasticity," Comp Meth Appl Mech Eng, 135, pp. 107-28.

[92] Quapp, K. M., and Weiss, J. A., 1998, "Material Characterization of Human Medial Collateral Ligament," J Biomech Eng, 120, pp. 757-63.

[93] Weiss, J., Lai, A., Loui, S., and Nisbet, J., 2000, "Behavior of Human Medial Collateral Ligament in Unconfined Compression," 46th Annual Meeting of the Orthopaedic Research Society, Orlando, FL.

[94] Batra, R., 2006, *Elements of Continuum Mechanics*, American Institute of Aeronautics and Astronautics, Reston, Va.

[95] Holzapfel, G. A., 2000, *Nonlinear Solid Mechanics*, John Wiley and Sons, Ltd, Chichester, United Kingdom.

[96] Ateshian, G. A., Ellis, B. J., and Weiss, J. A., 2007, "Equivalence between Short-Time Biphasic and Incompressible Elastic Material Responses," J Biomech Eng, 129(3), pp. 405-12.

[97] Huang, C. Y., Mow, V. C., and Ateshian, G. A., 2001, "The Role of Flow-Independent Viscoelasticity in the Biphasic Tensile and Compressive Responses of Articular Cartilage," J Biomech Eng, 123(5), pp. 410-7.

[98] Weiss, J. A., Gardiner, J. C., Ellis, B. J., Lujan, T. J., and Phatak, N. S., 2005, "Three-Dimensional Finite Element Modeling of Ligaments: Technical Aspects," Medical Engineering & Physics, 27(10), pp. 845-61.

[99] Puso, M. A., and Weiss, J. A., 1998, "Finite Element Implementation of Anisotropic Quasilinear Viscoelasticity," Journal of Biomechanical Engineering, 120(1), pp. 62-70.

[100] Thornton, G. M., Oliynyk, A., Frank, C. B., and Shrive, N. G., 1997, "Ligament Creep Cannot Be Predicted from Stress Relaxation at Low Stresses: A Biomechanical Study of the Rabbit Medial Collateral Ligament," Journal of Orthopaedic Research, 15, pp. 652-656.

[101] Woo, S. L.-Y., 1982, "Mechanical Properties of Tendons and Ligaments I. Quasi-Static and Nonlinear Viscoelastic Properties," Biorheology, 19, pp. 385-396.

[102] Woo, S. L.-Y., Gomez, M. A., and Akeson, W. H., 1981, "The Time and History-Dependent Viscoelastic Properties of the Canine Medial Collateral Ligament," Journal of Biomechanical Engineering, 103, pp. 293-298.

[103] Woo, S. L.-Y., Peterson, R. H., Ohland, K. J., Sites, T. J., and Danto, M. I., 1990, "The Effects of Strain Rate on the Properties of the Medial Collateral Ligament in Skeletally Immature and Mature Rabbits: A Biomechanical and Histological Study," Journal of Orthopaedic Research, 8, pp. 712-721.

[104] Fung, Y. C., 1993, *Biomechanics: Mechanical Properties of Living Tissues*, Springer-Verlag, New York.

[105] Provenzano, P., Lakes, R., Keenan, T., and Vanderby, R., Jr., 2001, "Nonlinear Ligament Viscoelasticity," Ann Biomed Eng, 29(10), pp. 908-14.

[106] Lakes, R. S., and Vanderby, R., 1999, "Interrelation of Creep and Relaxation: A Modeling Approach for Ligament," Journal of Biomechanical Engineering, 121(6), pp. 612-615.

[107] Provenzano, P. P., Lakes, R. S., Corr, D. T., and R, R., Jr., 2002, "Application of Nonlinear Viscoelastic Models to Describe Ligament Behavior," Biomech Model Mechanobiol, 1(1), pp. 45-57.

[108] Armstrong, C. G., Lai, W. M., and Mow, V. C., 1984, "An Analysis of the Unconfined Compression of Articular Cartilage," J Biomech Eng, 106(2), pp. 165-73.

[109] Cohen, B., Lai, W. M., and Mow, V. C., 1998, "A Transversely Isotropic Biphasic Model for Unconfined Compression of Growth Plate and Chondroepiphysis," J Biomech Eng, 120(4), pp. 491-6.

[110] Ateshian, G. A., Warden, W. H., Kim, J. J., Grelsamer, R. P., and Mow, V. C., 1997, "Finite Deformation Biphasic Material Properties of Bovine Articular Cartilage from Confined Compression Experiments," J Biomech, 30(11-12), pp. 1157-64.

[111] Huang, C. Y., Soltz, M. A., Kopacz, M., Mow, V. C., and Ateshian, G. A., 2003, "Experimental Verification of the Roles of Intrinsic Matrix Viscoelasticity and Tension-Compression Nonlinearity in the Biphasic Response of Cartilage," J Biomech Eng, 125(1), pp. 84-93.

[112] Yin, L., and Elliott, D. M., 2004, "A Biphasic and Transversely Isotropic Mechanical Model for Tendon: Application to Mouse Tail Fascicles in Uniaxial Tension," J Biomech, 37(6), pp. 907-16.

[113] Mak, A. F., 1986, "Unconfined Compression of Hydrated Viscoelastic Tissues: A Biphasic Poroviscoelastic Analysis," Biorheology, 23(4), pp. 371-83.

[114] Hirokawa, S., 2003, "An Experimental Study of the Microstructures and Mechanical Properties of Swine Cruciate Ligaments," JSME International Journal, 46(4), pp. 1417-1425.

[115] Miyazaki, H., and Kozaburo, H., 1999, "Tensile Tests of Collagen Fibers Obtained from the Rabbit Patellar Tendon," Biomedical Microdevices, 2(2), pp. 151-157.

[116] Yamamoto, E., Hayashi, K., and Yamamoto, N., 1999, "Mechanical Properties of Collagen Fascicles from the Rabbit Patellar Tendon," J Biomech Eng, 121(1), pp. 124-31.

[117] Screen, H. R. C., Bader, D. L., Lee, D. A., and Shelton, J. C., 2004, "Local Strain Measurement within Tendon," Strain, 40(4), pp. 157-163.

[118] Kouznetsova, V. G., Geers, M. G. D., and Brekelmans, W. a. M., 2004, "Multi-Scale Second-Order Computational Homogenization of Multi-Phase Materials: A Nested Finite Element Solution Strategy," Computer Methods in Applied Mechanics and Engineering, 193(48-51), pp. 5525-5550.

[119] Buechner, P. M., and Lakes, R. S., 2003, "Size Effects in the Elasticity and Viscoelasticity of Bone," Biomech Model Mechanobiol, 1(4), pp. 295-301.

[120] Fung, D. T., Wang, V. M., Laudier, D. M., Shine, J. H., Basta-Pljakic, J., Jepsen, K. J., Schaffler, M. B., and Flatow, E. L., 2009, "Subrupture Tendon Fatigue Damage," J Orthop Res, 27(2), pp. 264-73.

[121] Nakama, L. H., King, K. B., Abrahamsson, S., and Rempel, D. M., 2005, "Evidence of Tendon Microtears Due to Cyclical Loading in an in Vivo Tendinopathy Model," J Orthop Res, 23(5), pp. 1199-205.

[122] Ritter, M. C., Jesudason, R., Majumdar, A., Stamenovic, D., Buczek-Thomas, J. A., Stone, P. J., Nugent, M. A., and Suki, B., 2009, "A Zipper Network Model of the Failure Mechanics of Extracellular Matrices," Proc Natl Acad Sci U S A, 106(4), pp. 1081-6.

[123] Fenwick, S. A., Hazleman, B. L., and Riley, G. P., 2002, "The Vasculature and Its Role in the Damaged and Healing Tendon," Arthritis Res, 4(4), pp. 252-60.

[124] Zienkiewicz, O. C., and Taylor, R. L., 1989, *The Finite Element Method, Volume 1: Basic Formulation and Linear Problems*, London, England.

[125] Zienkiewicz, O. C., and Taylor, R. L., 2000, *The Finite Element Method Volume 2: Solid Mechanics, Fifth Edition*, Butterworth-Heinemann, Woburn, Ma.

[126] Ellis, B. J., Drury, N. J., Moore, S. M., Mcmahon, P. J., Weiss, J. A., and Debski, R. E., 2010, "Finite Element Modelling of the Glenohumeral Capsule Can Help Assess the Tested Region During a Clinical Exam," Computer Methods in Biomechanics and Biomedical Engineering, 13(3), pp. 413-8.

[127] Gardiner, J. C., and Weiss, J. A., 2002, "Subject-Specific Finite Element Modeling of the Human Medial Collateral Ligament," Proc 4th World Congress on Biomechanics, pp. 1099.

[128] Gitman, I. M., Askes, H., and Sluys, L. J., 2007, "Representative Volume: Existence and Size Determination," Engineering Fracture Mechanics, 74(16), pp. 2518-2534.

[129] Hazanov, S., 1998, "On Apparent Properties of Nonlinear Heterogeneous Bodies Smaller Than the Representative Volume " Acta Mechanica, 134(3-4), pp. 1619-6937.

[130] Pahr, D. H., and Zysset, P. K., 2008, "Influence of Boundary Conditions on Computed Apparent Elastic Properties of Cancellous Bone," Biomech Model Mechanobiol, 7(6), pp. 463-76.

[131] Hazanov, S., 1998, "Hill Condition and Overall Properties of Composites," Archive of Applied Mechanics, 68(6), pp. 385-394.

[132] Kanit, T., Forest, S., Galliet, I., Mounoury, V., and Jeulin, D., "Determination of the Size of the Representative Volume Element for Random Composites: Statistical and Numerical Approach," International Journal of Solids and Structures, 40(13-14), pp. 3647-3679.

[133] Kanouté, P., Boso, D., Chaboche, J., and Schrefler, B., 2009, "Multiscale Methods for Composites: A Review," Archives of Computational Methods in Engineering, 16(1), pp. 31-75.

[134] Garnich, M. R., and Karami, G., 2004, "Finite Element Micromechanics for Stiffness and Strength of Wavy Fiber Composites," Journal of Composite Materials, 38(4), pp. 273.

[135] Xia, Z., Zhou, C., Yong, Q., and Wang, X., 2006, "On Selection of Repeated Unit Cell Model and Application of Unified Periodic Boundary Conditions in Micro-Mechanical Analysis of Composites," International Journal of Solids and Structures, 43(2), pp. 266-278.

[136] Pennock, G. R., and Clark, K. J., 1990, "An Anatomy Based Coordinate System for the Description of the Kinematic Displacements in the Human Knee," J Biomechanics, 23, pp. 1209-1218.

[137] Yvonnet, J., Gonzalez, D., and He, Q. C., 2009, "Numerically Explicit Potentials for the Homogenization of Nonlinear Elastic Heterogeneous Materials," Computer Methods in Applied Mechanics and Engineering, 198(33-36), pp. 2723-2737.

[138] Geers, M. G. D., Kouznetsova, V. G., and Brekelmans, W. a. M., 2010, "Multi-Scale Computational Homogenization: Trends and Challenges," Jnl. Comp. Appl. Math., 234, pp. 2175-2182.

[139] Kouznetsova, V., Brekelmans, W. a. M., and Baaijens, F. P. T., 2001, "An Approach to Micro-Macro Modeling of Heterogeneous Materials," Computational Mechanics, 27(1), pp. 37-48.

[140] Okada, J.-I., Washio, T., and Hisada, T., 2010, "Study of Efficient Homogenization Algorithms for Nonlinear Problems," Computational Mechanics, 46(2), pp. 247-258.

[141] Feyel, F., 2003, "A Multilevel Finite Element Method (Fe2) to Describe the Response of Highly Non-Linear Structures Using Generalized Continua," Computer Methods in Applied Mechanics and Engineering, 192(28-30), pp. 3233-3244.

[142] Fatemi, J., Van Keulen, F., and Onck, P. R., 2002, "Generalized Continuum Theories: Application to Stress Analysis in Bone," Meccanica, 37, pp. 385-396.

[143] Freed, A. D., and Doehring, T. C., 2005, "Elastic Model for Crimped Collagen Fibrils," J Biomech Eng, 127(4), pp. 587-93.

[144] Grytz, R., and Meschke, G., 2009, "Constitutive Modeling of Crimped Collagen Fibrils in Soft Tissues," J Mech Behav Biomed Mater, 2(5), pp. 522-33.

[145] Maceri, F., Marino, M., and Vairo, G., 2010, "A Unified Multiscale Mechanical Model for Soft Collagenous Tissues with Regular Fiber Arrangement," J Biomech, 43(2), pp. 355-63.

[146] Breuls, R. G., Sengers, B. G., Oomens, C. W., Bouten, C. V., and Baaijens, F. P., 2002, "Predicting Local Cell Deformations in Engineered Tissue Constructs: A Multilevel Finite Element Approach," J Biomech Eng, 124(2), pp. 198-207.

[147] Sander, E. A., Stylianopoulos, T., Tranquillo, R. T., and Barocas, V. H., 2009, "Image-Based Multiscale Modeling Predicts Tissue-Level and Network-Level Fiber Reorganization in Stretched Cell-Compacted Collagen Gels," Proc Natl Acad Sci U S A, 106(42), pp. 17675-80.

CHAPTER 3

EFFECTS OF DECORIN PROTEOGLYCAN ON FIBRILLOGENESIS, ULTRASTRUCTURE AND MECHANICS OF TYPE I COLLAGEN GELS

Abstract

The proteoglycan decorin is known to affect both the fibrillogenesis and the resulting ultrastructure of in vitro polymerized collagen gels. However, little is known about its effects on mechanical properties. In this study, 3D collagen gels were polymerized into tensile test specimens in the presence of decorin proteoglycan, decorin core protein or dermatan sulfate. Collagen fibrillogenesis, ultrastructure, and mechanical properties were then quantified using a turbidity assay, 2 forms of microscopy (SEM and confocal), and tensile testing. The presence of decorin proteoglycan or core protein decreased the rate and ultimate turbidity during fibrillogenesis and decreased the number of fibril aggregates (fibers) compared to control gels. The addition of decorin or core protein increased the linear modulus by a factor of 2 compared to controls, while the addition of DS reduced the linear modulus by a factor of 3. Adding decorin after fibrillogenesis had no effect, suggesting that decorin must be present during fibrillogenesis to increase the mechanical properties of the resulting gels. These results show that the inclusion of decorin proteoglycan increases the mechanical properties of

collagen gels, and it appears to do so by reducing the aggregation of fibrils into larger order structures such as fibers and fiber aggregates.

Introduction

Type I collagen is the fundamental building block of connective tissues such as tendon, ligament, skin and bone. It is organized into fibrillar structures via a guided self-assembly process known as fibrillogenesis. Collagen fibril diameter, length and organization are tightly regulated during fibrillogenesis to produce tissues with different functional properties. In tendon and ligament, highly aligned collagen fibrils are necessary to facilitate force transmission [1], while a lamellar organization is necessary in the cornea to maintain transparency [2]. The small leucine-rich proteoglycans (SLRPs), including decorin, biglycan, fibromodulin and lumican are believed to play a vital role in guiding the proper assembly of collagen during fibrillogenesis [3-6]. As evidenced by a number of knockout studies in mice, a deficiency in one or more of these proteoglycans (PGs) leads to altered tissue structure and function [6, 7].

Of the SLRPs relevant to fibrillogenesis, decorin is arguably one of the most important, and certainly the most well studied [4, 6-8]. Decorin is present in nearly all tissues [4, 9] and has been implicated in fibrillogenesis and the regulation of certain growth factors such as EGF and TGF-beta [10]. Structurally, decorin consists of a core protein covalently bonded to a highly electronegative dermatan sulfate glycasaminoglycan (GAG). The core protein has a high binding affinity for collagen. Developmental studies have found that increased decorin concentration in tendons of developing mice is concurrent with the lateral and linear growth of fibrils [6], suggesting a role in the regulation of fibril diameter, length and organization. Knockout studies have

shown that mice with a decorin deficiency display abnormal fibril structure and organization, as well as fragile tissues with decreased strength and stiffness [6, 7]. However, in vivo studies make isolating the effects of decorin nearly impossible due to genetic compensation. Thus, in vitro studies have been crucial in the effort to understand the role that decorin plays in the fibrillogenesis of collagen. Decorin inhibits fibrillogenesis in cell-free constructs of polymerized type I collagen [9, 11], and decorin prevents the aggregation of fibrils into fibers [12, 13]. There are conflicting reports that decorin regulates the fibril diameter of in vitro collagen constructs [9, 14, 15] .

Given that decorin deficient mice developed mechanically inferior connective tissues, it is natural to hypothesize that the presence of decorin during fibrillogenesis will increase the strength of collagen gels in vitro. The purpose of this study was to test whether the presence of decorin during the polymerization of type I collagen gels increases the stiffness and tensile strength of the resulting gels. To understand the mechanisms by which decorin modifies this mechanical behavior, this study also sought to characterize how the decorin proteoglycan and its individual components (core protein and GAG) affect fibrillogenesis kinetics and the resulting fibrillar organization. This research demonstrates the role that decorin plays in the fibrillogenesis of type I collagen in vitro and its role in modifying force transmission and mechanical behavior of collagen gels.

Methods

Decorin purification

Decorin was originally obtained from a commercial resource (D8428, Sigma) as cited in previous studies [12, 16], but it was found to be contaminated with approximately

50% biglycan, another SLRP (Fig 3.1 lanes 1 and 2). To ensure that the results of the experiments described were due to decorin and not biglycan, decorin was purified from bovine tendon [17]. Purified decorin proteoglycan and the protein core following treatment with chondroitinase ABC treatment are shown in Figure 3.1 (lanes 3 and 4 respectively). The absorbance of decorin solutions at 280 nm was verified by SDS-PAGE and used to calculate the protein concentration using an extinction coefficient of 19285 $M^{-1}cm^{-1}$. The concentration of GAG in the decorin solution was also determined, using the dimethyl methylene blue (DMB) assay [18].

Gel preparation

Type I collagen gels (2 mg/ml, rat tail, BD Biosciences) were prepared for fibrillogenesis assays and mechanical gel testing. Collagen solutions were mixed on ice, with the reagents added in the following order: collagen, H_2O, test molecules (decorin, dermatan sulfate, etc. in 1X PBS), 10X PBS containing phenol red, and 1N NaOH. One mL of solution was pipetted into dog-bone shaped silicone molds, which were pressed onto glass plates with identical dimensions to those used in previous work [19]. Immediately after pouring, four black microbeads (300 um) were placed on the surface to act as markers for tracking strain during testing. Gels were polymerized at room temperature unless stated otherwise. One hundred and fifty microliters of the solution was also pipetted in duplicate into 96 well plates for monitoring fibrillogenesis and polymerization pH. Changes in turbidity (or light scattering) at a wavelength of 405 nm were monitored over time and used to quantify the kinetics of fibrillogenesis including rate, ultimate turbidity and lag time.

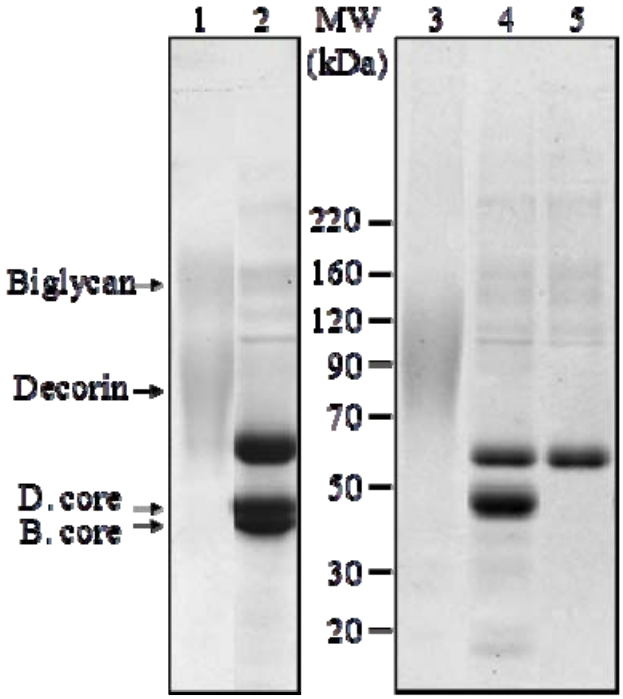

Figure 3.1: SDS-PAGE of decorin proteoglycan and core protein. Decorin obtained from a commercial source (lanes 1 and 2) and decorin purified on site (lanes 3 and 4, 10 μg) were resolved on a 4-16% acrylamide gel and then stained with coomassie blue. Lanes 2, 4, and 5 were treated with 7 mU of chondroitinase ABC to degrade the glycosaminoglycan side chains, and thus proteoglycans migrate according to their core protein molecular weight. Commercial decorin was contaminated with approximately 50% biglycan, as demonstrated by a higher molecular weight species in lane 1, and a smaller molecular weight species (41 kDa) in lane 2. Decorin purified on site consisted of a single core species (43.4 kDa). The major band in lane 5 (chondroitinase treatment only) has a calculated molecular weight of 61.5 kDa and is bovine serum albumin added to the chondroitinase as a stabilizer.

Since the polymerization pH can significantly alter the mechanical properties and structure of collagen gels [19], polymerization pH for each sample was determined using the phenol red absorbance spectrum change that occurs as a function of pH. The absorption peak for phenol red shifts from 430 nm under acidic conditions to 560 nm under basic conditions. A standard curve of phenol red solutions was generated as a function of pH using the absorbance ratio of 560 nm / 430 nm vs pH. This standard

curve was then used to determine the polymerization pH of each collagen gel solution prior to polymerization based on the absorbance ratio.

Material testing

A mechanical testing system was assembled following previous studies [19]. Briefly, it consisted of a movable linear stage, a 10 g load cell (resolution ±0.005 g), an acrylic test chamber and two plastic clamps for gripping the sample (Fig 3.2). Two cameras (Allied Vision, resolution 1360x1024) were placed above and to the side of the test chamber to measure the sample cross section and to track strain. Two white LED lamps were placed at an angle to illuminate the sample. Stage movement, data acquisition and video acquisition were controlled via a PC. The stage and data

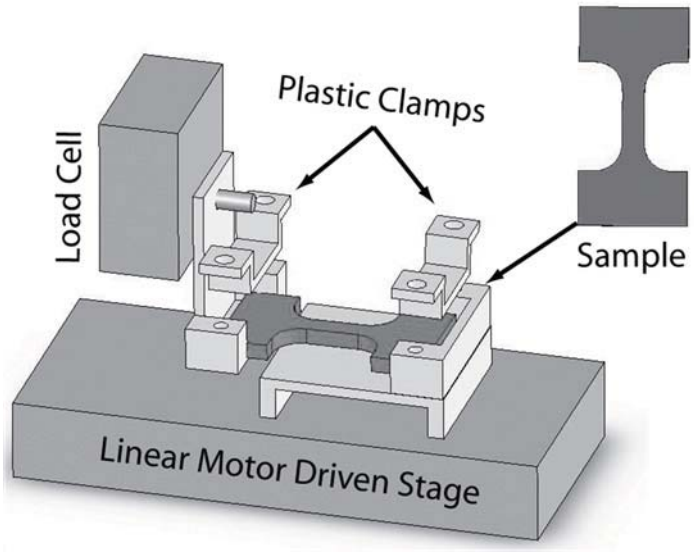

Figure 3.2: Gel mechanical testing apparatus. The gels were tested using an apparatus consisting of a linear motor stage, a load cell, plastic gel clamps and a PBS test chamber [19]. The sample geometry was given a dog bone shape to obtain a homogenous strain distribution in the testing region.

acquisition was controlled using Aerotech A3200 software (Aerotech Inc., Pittsurgh, PA) and the image acquisition was controlled using DMAS 6 software (Spica Technologies, Kihei, Maui). The acrylic chamber was filled with room temperature PBS prior to testing.

Samples were polymerized in groups of 12 (N=3 for each of the four groups) and mechanically tested the following day. The material properties of the gels stabilized approximately 16 hours following the onset of polymerization [19]. A total of three groups of 12 were tested, giving a sample of N=9 for each group. Samples were removed from the molds, attached to the tissue clamps, which were secured using nylon screws. The gels were then subjected to constant strain rate testing at 10 mm/min (50%/min) until failure. The force was recorded at 20 Hz during testing and images were acquired from the top and the side at 2 Hz. A total of 58 samples were included in the data analysis, nine for each of the four groups and 24 for the dose-response study (described in a following section).

Strain analysis

Images were acquired from the top and bottom cameras prior to testing to measure cross sectional area. The cameras were calibrated with a plastic blank, which had identical dimensions to the test sample. The strain was computed in the three principal directions using custom code written in Matlab (MathWorks, Natick, MA). The program tracked the strain along the test direction from the displacements of the black micro beads, while strains along the width and thickness were determined by tracking the sample edges. For each frame, the center of the image corresponding to the test area was extracted and thresholded. An automated thresholding algorithm was used based on

Otsu's method ('graythresh' function in Matlab) [20]. The thresholded image was segmented using the 'bwtraceboundary' function in Matlab, and then lines were fit to the top and bottom edges of the segmented boundary. The differences between the center points of the best fit lines were taken to be the width or thickness of the sample. Changes in this distance were used to compute the engineering strain in these directions. The outlines of the beads were extracted from the thresholded image of the top video camera and a circle was fit to each bead. The centroids were then tracked to measure strain in the test direction [8].

The cross sectional area in the reference configuration was computed from the reference width and thickness. The engineering stress was then computed for each sample by dividing the force by the reference area. The differential Poisson's ratio [21] was computed using $\nu_{ij} = -\frac{\partial e_i}{\partial e_j}$. The strain derivatives were found by fitting cubic splines to the strain data and then computing the derivatives of the splines relative to sampling time. The Poisson's ratio was then computed using the chain rule: $v_{ij} = -\frac{\partial e_i}{\partial t}\left(\frac{\partial e_j}{\partial t}\right)^{-1}$. To obtain the linear modulus, the derivative of the stress-strain curve was obtained. Since clamp strain is not representative of the strain in the gel mid-substance, the optical strain was used. The stress-strain derivative was computed numerically by finding the slope of the best fit line, which was fit to a window of ±5 points to reduce errors due to noise. The maximal value for this derivative was taken to be the linear modulus of the sample, which typically occurred at ~20% clamp-to-clamp strain. The maximal stress attained during testing was taken to be the tensile strength.

The modulus, tensile strength and maximal Poisson's ratios were compared between groups using a one way ANOVA (alpha=0.05).

Microscopy

Immediately following mechanical testing the gels were fixed in 4% formaldehyde in PBS. Gels were prepared for scanning electron microscopy (SEM) analysis as previously described [12]. Gels were sputter coated with gold using a Pelco auto sputter coater (SC-7). Gels were imaged on an environmental SEM (FEI Quanta 600 FEG, Company, City, State) at high vacuum. Images were obtained at both 5,000X and 15,000X for gels from 3 independent days of polymerization. Images were acquired at a resolution of 3,775×4,096 pixels. Six images were acquired of each sample at each magnification. A total of 18 images from three different days were acquired for each group at both magnifications.

For confocal reflection microscopy (CRM), gels were placed on a glass cover slip, kept moist with PBS and imaged using a 60X water lens at a wavelength of 458 nm. A total of 9 slices were imaged per stack using a 1 μm step size at a resolution of 2,048×2,048 pixels. Twelve samples were imaged, three from each group.

Image analysis

An automated image analysis algorithm was used to extract the diameter of structures that will be denoted as fibers [20, 22-24]. Fibers were considered to consist of two or more fibrils bundled together (Fig 3.3). The image analysis algorithm did not distinguish between fibers and fibrils. Thus, individual fibrils were measured as small diameter fibers.

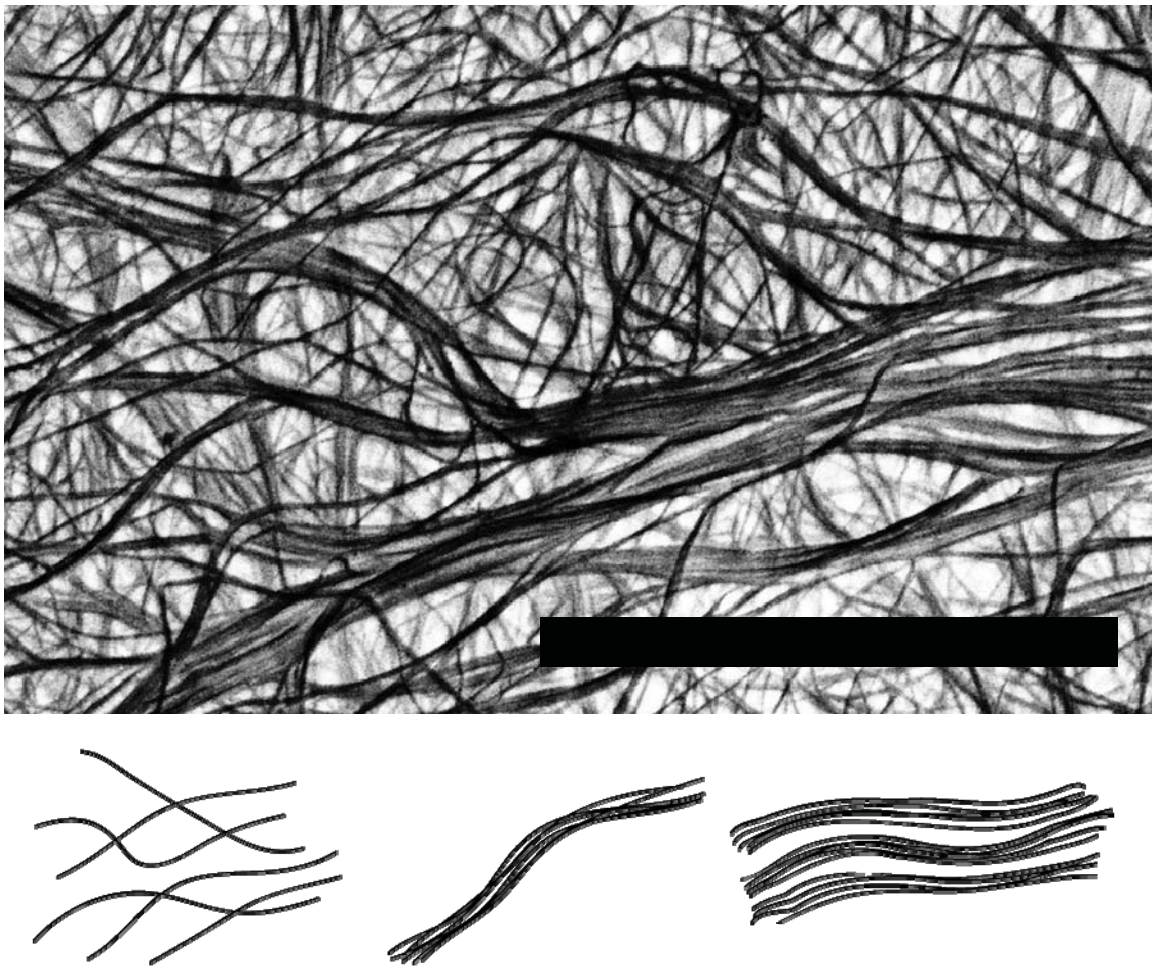

Figure 3.3: Organizational patterns within collagen gels. A 5000X SEM image of a 2 mg/ml gel shows that single fibrils (bottom, left) fibril bundles or fibers, (bottom, middle) and fiber bundles (bottom, right) are present. Image has been inverted so that the fibrils and fibers appear black. Scale bar=5 um.

The images were conditioned using a 3×3 median filter, a Gaussian smoothing filter (window=6 pixels, standard deviation=2 pixels) and histogram equalization (for SEM images only) to remove noise, increase contrast and smooth the image [20]. Images were then thresholded using Otsu's method [20]. A skeletonization was then performed on the binary image (bwmorph('skel') function in Matlab), followed by spur removal (bwmorph('spur') function in Matlab). The branch points of the skeleton were determined (bwmorph('branchoints') function in Matlab) and used as nucleation points

for a direct tracking algorithm [24]. Starting at a nucleation point, a fiber was tracked until it either ended or intersected with another nucleation point. This fiber was then removed from the image, and another fiber was then tracked and removed. This process was repeated until no fibers remained within the image. The length of each fiber was computed using a line integral along the fiber. The width of each fiber was determined by overlaying the skeleton on the distance transform of the thresholded image and then computing the average of distance values along the fiber [22]. The area of each fiber was determined by multiplying the average fiber width by the fiber length.

Dose-response study

Collagen gels were prepared with concentrations of 0, 1, 10, 25, 50 and 100 μg/ml of decorin (243, 24.3, 9.7, 4.9, and 2.4 : 1 molar ratios of tropocollagen to decorin, respectively). A set of twelve gels were tested, with two samples for each concentration. Both the turbidity assay and mechanical testing were performed. Based on the results of this study, a concentration of 50 μg/ml was used for investigations described below unless stated otherwise.

Decorin component study

To determine the part of the decorin proteoglycan that was responsible for altering collagen gel mechanics, collagen gels were prepared with 50 μg/ml decorin proteoglycan, decorin core protein, dermatan sulfate (DS), or bovine serum albumin (BSA) as a control. Decorin core protein was obtained by treating 350 μl of decorin (0.6 mg/ml) with 0.02 units of chondoitinase ABC (Sigma) at 37^{o}C overnight. Dermatan sulfate purified from

porcine intestinal mucosa was obtained from EMD chemicals. The turbidity assay, material testing and microscopy were performed as previously described.

Effects of temperature

To determine if decorin had the same effect at higher polymerization temperatures, gels were polymerized with and without decorin at 37°C. A total of three gels were polymerized for both the control and decorin gels at 37°C. After the completion of polymerization, gels were subjected to the previously described material test protocol and SEM imaging protocol.

Post polymerization addition of decorin

To test whether decorin must be present during polymerization to affect the material properties of collagen gels, three groups of gels were tested: control gels (without decorin), gels with 70 μg/ml decorin added prior to polymerization and gels with decorin added one hour after the initiation of polymerization. All gels were poured into the molds at RT and allowed to polymerize for one hour, at which point 125 μl of PBS was applied to the surface (test area) of the control and decorin containing gels. The third set of gels had 125 μl of PBS containing decorin (87.5 μg) applied to the test area surface. Gels were then incubated at 37^{o}C to facilitate diffusion of the decorin into the gels. To verify that decorin had penetrated into the test area of the gels, an extra set of gels not used for testing was stained with dimethyl methyl blue, which changes color from blue to pink as it binds to glycosaminoglycans [25]. A total of 6 gels were subjected to material testing for each group.

Results

The inclusion of decorin proteoglycan during the polymerization of type I collagen gels affected the process of fibrillogenesis, the material properties and the fibril organization of the resultant gels. The modulus of the gels increased in a dose dependent manner that was well described by a sigmoidal curve fit (Fig 3.4). The linear modulus was over two times larger for gels containing 50 μg/ml of decorin as compared to the control (5.8 vs. 2.4 kPa). The tensile strength also increased in a similar fashion (data not shown). The modulus did not increase appreciably from 50 μg/ml (decorin to collagen ratios) to 100 μg/ml (decorin to collagen ratios). Decorin also affected the kinetics of fibrillogenesis in a dose-dependent manner as demonstrated by the turbidity curves (Fig 3.4). The ultimate turbidity and rate of fibrillogenesis (slope of linear region) decreased with an increasing concentration of decorin. Adding decorin proteoglycan after polymerization did not change the process of fibrillogenesis nor the material properties of the resultant gels (Fig 3.5).

To determine the part of the decorin proteoglycan that was responsible for these effects, decorin core protein and dermatan sulfate were individually polymerized with collagen. Their effects on fibrillogenesis and gel mechanics were then tested. All the gels displayed a linear stress-strain behavior between 10% and 40% tensile strain, with clear differences between the groups tested (Fig 3.6 upper left). Decorin core protein significantly increased the modulus ($p<0.001$) and tensile strength ($p<0.001$) relative to BSA control, while DS significantly reduced the modulus ($p<0.001$) and tensile strength ($p<0.001$) of the gels relative to control (Fig 3.6 lower left).

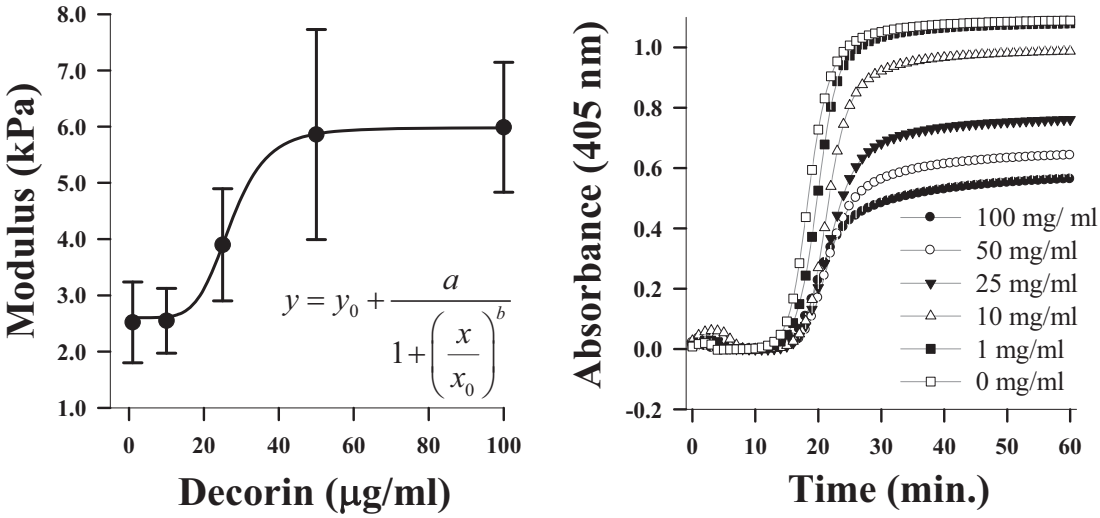

Figure 3.4: Dose response study. (Left) The addition of decorin resulted in a dose dependent increase in the linear modulus of the gels. A logistic growth curve provided an excellent fit to the data. Since each data point represents only two samples, the error bars are given to represent the range of the results, not the standard deviation. Curve fit values: y_o=2.60, x_o=27.2, a=3.38, b=-5.59. (Right) Decorin changes the kinetics of fibrillogenesis, demonstrated by the turbidity assay. Increasing concentrations of decorin led to increasing lag times, a decreasing in rates of fibrillogenesis (slope of linear region) and a decreasing ultimate turbidity.

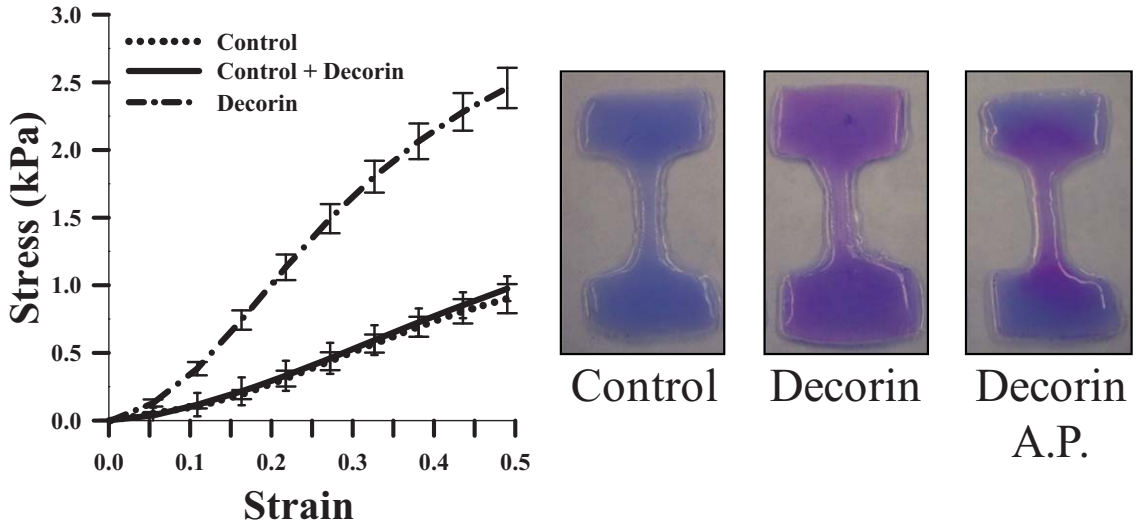

Figure 3.5: Timing of decorin addition alters the mechanical properties. (Left) The addition of decorin after the polymerization of the gels did not change the mechanical properties relative to control. (Right) Gels stained with dimethyl methylene blue demonstrate the presence of proteoglycan (purple color) within the test region of the decorin polymerized gel and the gel which had decorin added after polymerization (AP).

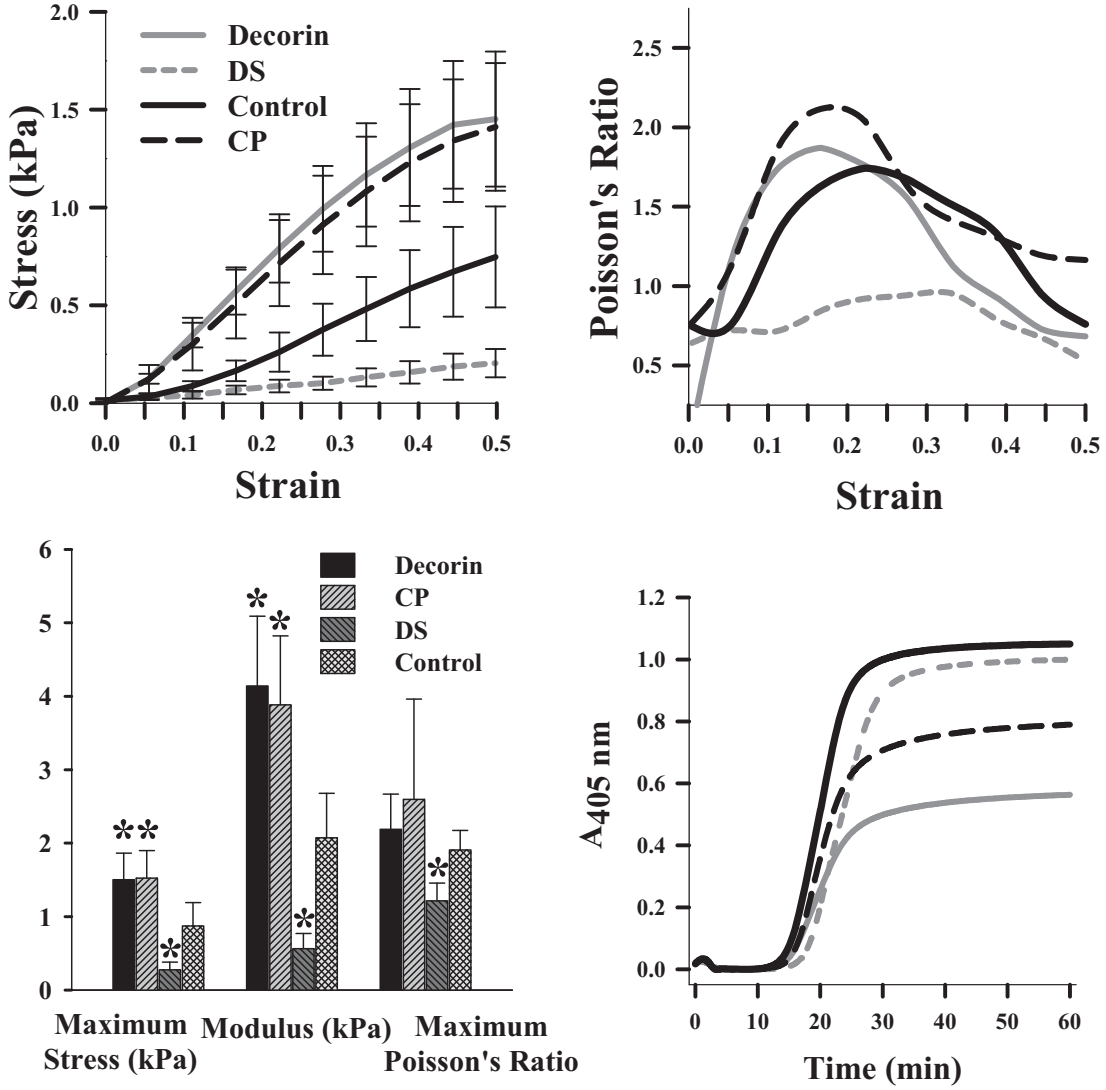

Figure 3.6: Effects of decorin, core protein and DS on fibrillogenesis and mechanical properties. (Upper Left) The stress-strain behavior was nonlinear. However, a distinct linear region was present. Curves represent the average of all samples while error bars represent the standard deviation. (Upper Right) The differential Poisson's ratio was a nonlinear function of strain. Curves represent the average for all samples. Error bars were removed for clarity. (Lower Left) The decorin and core protein gels had a higher modulus and tensile strength than the control gels, while the control gels had a higher modulus and tensile strength than the DS gels. The DS gels had a maximum Poisson's ratio that was significantly less than the control gel. Significant differences from control are indicated with asterisks. (Lower Right) The ultimate turbidity varied between groups, with decreasing turbidity seen in the DS, decorin core and decorin relative to the control. The lag times also varied, with the DS gels having the largest increase in lag time, followed by the core protein and the decorin gels. Curves represent the average for all samples. Error bars removed for clarity.

The modulus and tensile strength of gels polymerized with the core protein was double that of the control gels, while the DS gels had a modulus and tensile strength that was reduced by 1/3 as compared to the control. There was no significant difference between the modulus and tensile strength of the decorin and core protein gels. The addition of DS slightly decreased the ultimate turbidity of the gels relative to BSA control, while the core protein and decorin reduced the turbidity, but only decorin PG had a significant effect ($p< 0.05$, Fig 3.6 upper right). The decrease in turbidity was greatest with the addition of decorin, followed by the core protein and then DS. There was a significant linear correlation between the modulus and the ultimate turbidity (Fig 3.7).

Since the strain dependent Poisson's ratio of a fiber network is determined by the fiber network structure [26, 27], Poisson's ratios were used to determine how the addition of decorin and other molecules changed the structure of the fibrillar network. The Poisson's ratio was a nonlinear function of the strain for all gels, and it greatly exceeded the isotropic limit of 0.5 (Fig 3.6 upper right). The maximum values of the Poisson's ratio were 2.19±0.48 for the decorin gels, 2.60±1.37 for the core protein gels, 1.21±0.24 for the DS gels and 1.91±0.27 for the control gels (Fig 3. 6 lower left). Only the DS gels had a maximum Poisson's ratio that was significantly different from the control gel ($p<0.05$). The strain at which the maximum Poisson's ratio was attained varied between the gel groups, but the differences were not statistically significant.

To determine the effect of decorin proteoglycan and its constituents on fibril structure and organization, the collagen gels were examined using SEM. Three distinct organizational patterns were seen, including single fibrils, fibrils grouped into fibers and fibers grouped into fiber bundles (Fig 3.3). The decorin and core protein gels consisted

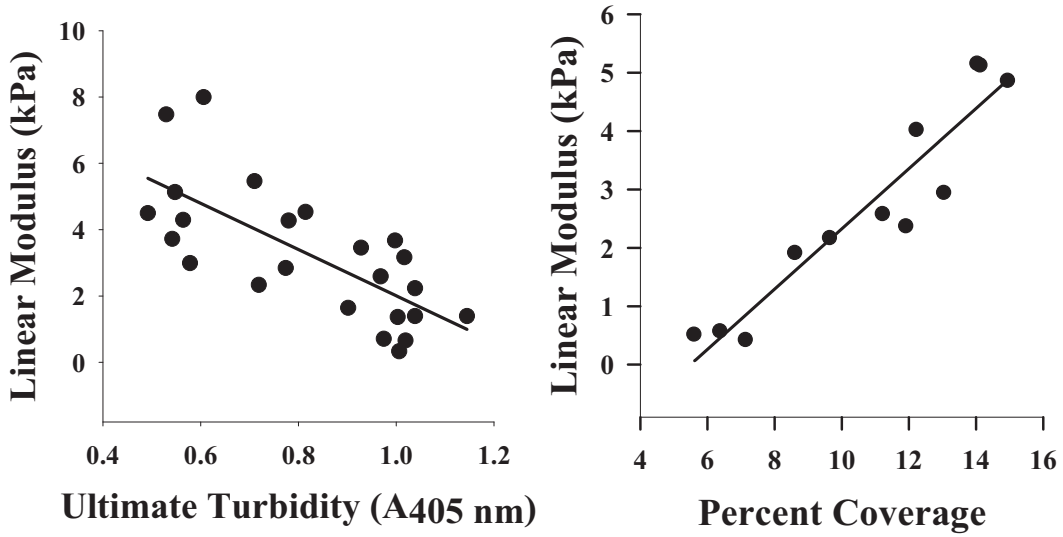

Figure 3.7: Correlations between linear modulus, ultimate turbidity, and fibril density. (Left) Linear regression of the linear modulus vs. the ultimate turbidity (for all data sets) revealed a significant negative linear correlation ($R^2 = 0.5209$, $p<.0001$). (Right) A linear regression of the linear modulus vs. confocal fibril area coverage shows a significant positive linear correlation ($R^2=.8786$, $p<.0001$).

primarily of either single fibrils or small fibers, while the control gels consisted of both single fibrils and larger fibers. The DS gels consisted primarily of fibers and fiber-bundles.

At a magnification of 15,000X there were noticeable qualitative differences between the SEM images from different groups (Fig 3.8 top row). Compared to control, the decorin and core protein gels had denser fibril networks with less grouping of fibrils into fibers. As with the results for material testing, decorin proteoglycan and core protein gels were very similar. Compared to control, the fibrils in the DS gels aggregated more frequently to form a large number of fibers, which often aggregated further into multi-fiber, bundled structures. The resulting histograms of the fiber diameters show that the diameter distributions varied between groups (Fig 3.8 bottom row).

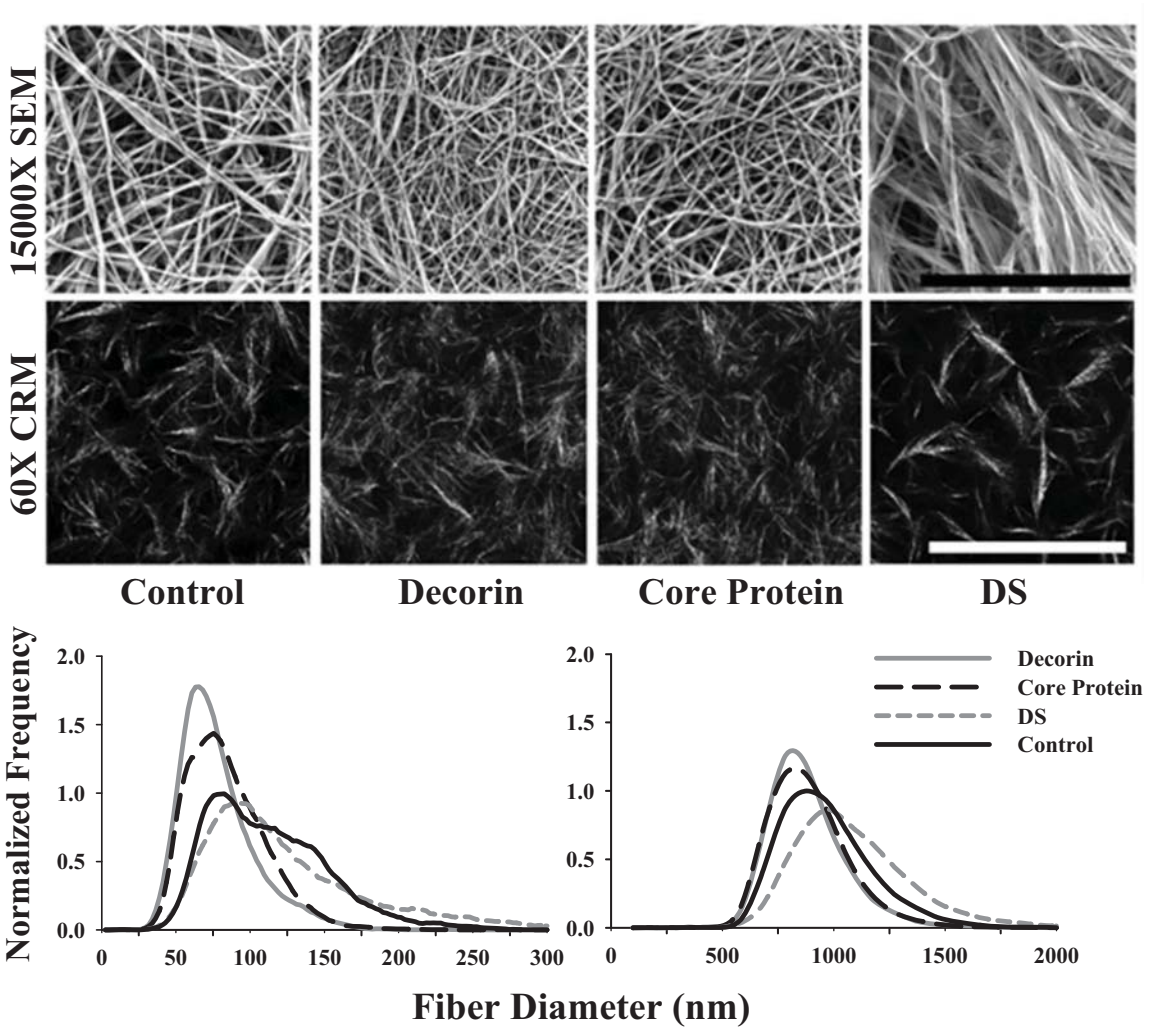

Figure 3.8: SEM and confocal imaging results. Top Row: A 15000X SEM images reveal that the control (left) had more bundling of fibrils into fibers than the decorin (center left) and core protein (center right) gels. Fibrils in the DS gels (right) were grouped into fibers, which were further grouped into fiber bundles. Black scale bars = 5um. Center Row: Confocal imaging at 60X revealed longer, thinner fibers in the decorin (center left) and DS (center right) gels as compared to the control (left), while the DS gels had shorter and thicker fibers. White scale bar = 75 um. Bottom Row: The normalized fiber diameter distributions for the 15000X images (left) reveal a significant difference in fiber diameter for the Decorin and CP gels as compared to the control and DS gels. The fiber diameter distribution for the confocal images (right) reveals a significant difference for the fiber diameter between the decorin, core protein and DS gels relative to the control. All distributions were normalized relative to the control.

The mean fiber diameter computed from the SEM images was 78±11 nm for the decorin gels, 84±11 nm for the core protein gels, 125±26 nm for the DS gels and 113±26 nm for the control gels. The mean diameter of both the decorin and core protein gels were significantly different from the control ($p<0.001$), while the mean diameter of the DS gels was not different. Since SEM only examines the surface structure of dehydrated gels, confocal reflection microscopy (CRM) was also utilized to study the interior of hydrated collagen gels. CRM images revealed similar qualitative observations to that of the SEM. The decorin and core protein gels had fibers with a smaller diameter relative to control, while the DS gels had much thicker and shorter fibers as compared to the control (Fig 3.8 middle row). The image analysis algorithm revealed that the decorin and core protein gels had distributions with smaller fiber diameters relative to control, while the DS gels had a distribution with larger fiber diameters. The mean fiber diameter computed from the CRM images was 883±13 nm for the decorin gels, 888±20 nm for the core protein gels, 1090±43 nm for the DS gels and 965±40 nm for the control gels. The mean fiber diameter for the decorin and core protein gels was significantly less than the control ($p<0.001$), while the mean fiber diameter was significantly larger for the DS gels relative to control ($p<0.001$). In addition, the area occupied by fibril structures was significantly greater in the decorin containing gels ($p<0.001$), and significantly less in the DS-containing gels ($p<0.001$).

In the absence of decorin, gels polymerized at 37^{o}C had a stiffness that was nearly double that of the RT control. In the presence of decorin, gels polymerized at 37^{o}C were nearly 4 times stiffer than the RT control and twice as stiff as the 37^{o}C control (Fig 3.9).

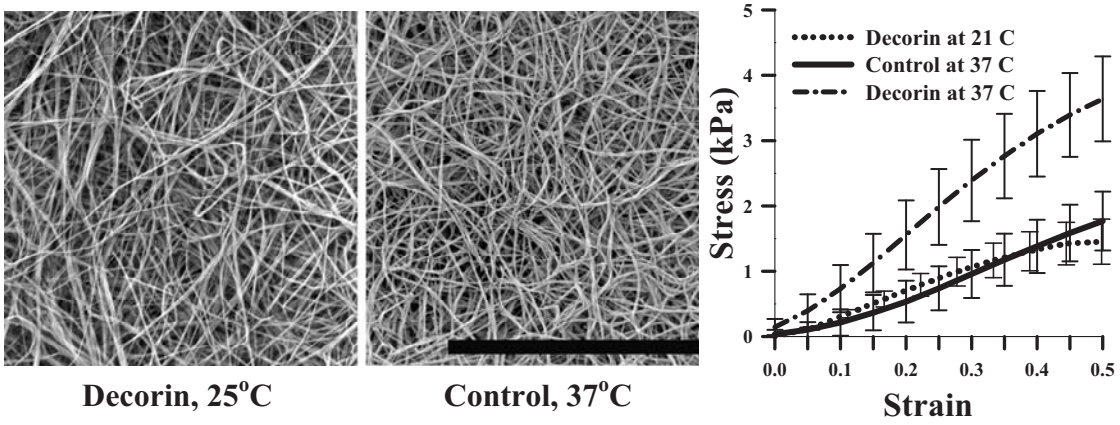

Figure 3.9: Temperature dependence study. (Left) The SEM images (15000X) revealed that the decorin gels polymerized at RT had similar fibril networks to the control gels polymerized at 37°C. Scale bar = 5 μm. (Right) The stress-strain curves revealed that the decorin gels polymerized at RT had a similar stiffness to the control gels polymerized at 37°C.

SEM imaging revealed that the control gels polymerized at 37°C had dense networks primarily consisting of single fibrils. The network topology of the decorin gels polymerized at RT and 37°C was indistinguishable from the control gels polymerized at 37°C.

Discussion

The addition of decorin during polymerization of type I collagen significantly increased the modulus and tensile strength of the resulting gels. We hypothesize that the mechanism by which decorin increases the mechanical strength of the gels is through modification of collagen fibril organization. This is evidenced by the significant decrease in the mean fiber diameter induced by the presence of decorin. This correlation is consistent with previous observations, which found that decreased fiber diameter was associated with increased gel strength in collagen gels [19, 28]. It has been suggested that decreased fiber diameters result in a network with increased interconnectedness, thus

facilitating more efficient force transfer [26]. Similarly, experiments using organogels, which are thermoreversible 3D cross linked networks with a liquid organic phase, found that increasing the junction density (i.e., number of fiber connections) increased the storage modulus [29]. Along these lines, measurements of the area occupied by collagen fibrils/fibers using CRM revealed that decorin-containing gels had a greater area than control or DS-containing gels. This is in agreement with TEM results by Iwasaki et al., which found that decorin significantly increased the cross-sectional area of fibril occupied space. Taken together with the data obtained here, decorin appears to increase the mechanical properties of collagen gels by preventing the lateral aggregation of fibrils into higher order structures, which in turn may promote longer fibrils that are more interconnected, resulting in a stronger collagen gel.

Although previous studies have examined the effects of decorin proteoglycan on fibrillogenesis, collagen gel structure, and mechanical properties, none have evaluated all three of these parameters or made correlations between them. Only a single study has examined the effects of decorin on the tensile properties of collagen [16]. This study saw a 1.8 fold increase in the tangent modulus when decorin was added, but due to the large variability in their system, there was not a statistical significance when compared to the appropriate control. That study tested extruded collagen fibers which were dried prior to mechanical testing, which changes the material properties of collagen. Numerous studies have examined the effects of decorin on collagen fibrillogenesis using the turbidity assay. Most have found that decorin decreases the ultimate turbidity, although some cite no change or an increase in turbidity. This decrease in turbidity has been directly attributed to smaller diameter fibers [30].

Other mechanisms that may explain the increased mechanical strength of the decorin gels include the presence of more end to end fibril fusions [31], a change in mean fibril length [32] as well as an altered mean fibril diameter [5]. SEM imaging did not allow for the direct measurement of fibril length or the observation of fibril fusions, as tracking single fibrils is not possible given the overlap that results from gel dehydration. As a consequence, this study was unable to explore the mechanisms of increased fibril length and increased frequency of fibril fusions. Individual fibril diameters were not quantified in the present study. However, there did not appear to be change in this diameter across groups, as has been reported by others [9, 15]. In addition, previous results show that an increased mean fibril diameter will only generate a slight increase in fibril strength [5]. In this study the linear modulus and tensile strength was doubled, suggesting that changes in fibril diameter are not the mechanism responsible for this change.

Previous studies have reported that decorin modifies the grouping of fibrils into fibers [12, 13]. It was suggested that decorin prevented side to side fibril aggregation. Structural studies indicate that decorin may preferentially bind to whole fibrils, suggesting decorin's regulatory role at the fibril level [33]. It is interesting to observe that the decrease in fiber diameter resulting from the addition of decorin is similar to the decrease in fiber diameter seen from increasing the temperature during polymerization [19]. We found that the increase in mechanical strength and decrease in fiber diameter was similar between decorin gels polymerized at room temperature and control gels polymerized at 37^{o}C (Fig 3.9). The mechanism by which this occurs is still under investigation.

In vivo, decorin is known to play a role in collagen fibrillogenesis and as a molecule that can bind growth factors [10]. It has also been suggested to contribute to the material properties of connective tissues by bridging adjacent collagen fibrils, and thus allowing the transfer of force between fibrils [8]. Mechanical testing of connective tissue from decorin-deficient mice also support this role for decorin since changes in the material properties were observed. However, due to genetic compensation (e.g., upregulation of other SLRPs such as biglycan), interpretation of these phenotypes is difficult. Recently, the model of how decorin can bridge adjacent fibrils was challenged by testing the material properties of connective tissue following chondroitinase treatment. Complete degradation of the DS side chain of decorin in human ligament, which would eliminate the proposed mechanism of fibril cross linking, had no effect on the tensile properties of connective tissue [8]. It is possible, however, that decorin does crosslink fibrils, but through an unknown mechanism that is independent of the GAG side chain. The in vitro data presented here also do not favor a cross linking mechanism that can explain the increase in the material properties of collagen gels. It was found that decorin must be present during fibrillogenesis, and that decorin added after fibrillogenesis had no effect on the tensile properties. If decorin was responsible for transferring forces between fibrillar structures in gels, the addition of decorin after polymerization would yield similar results as that added before polymerization. Also, it was found that the core protein facilitates a similar increase in mechanical strength to that of the whole decorin molecule. This again rules out the possibility of a mechanical contribution from direct interaction of the DS gag chains, which was integral to the long standing cross-linking model.

The results of this study suggest a possible in vivo role for decorin, namely that its primary function during fibrillogenesis is to prevent the aggregation of fibrils. According to proposed morphogenesis models, small diameter, immature fibrils fuse to form large diameter, mature fibrils [3]. By preventing the aggregation of fibrils, decorin would act to prevent further lateral growth of fibrils. This is consistent with the experimental observation that a decorin deficiency leads to abnormally large fibrils during development [6].

The addition of DS during the polymerization of collagen was found to have an effect opposite to that of adding the core protein, which was to increase the aggregation of fibrils into fibers and the aggregation of fibers into fiber bundles. This is very interesting considering that when an equivalent amount of DS is added by the addition of decorin proteoglycan to gels, this effect is not observed. This suggests that DS may be localizing differently, or held in a different conformation when attached to decorin. However a recent study suggests that DS localizes to the same D-period of collagen fibrils whether the core protein is present or absent [34]. It is also possible that there are compositional differences between DS from intestinal mucosa and tendon. The observed change in fiber organization ultimately led to a significant decrease in linear modulus and tensile strength of the gels. Whereas the core protein increased the gel stiffness by decreasing the fiber diameter, the DS decreased the stiffness by increasing the fiber diameter. We hypothesize that this is a result of decreased fiber connectivity, and thus reduced efficiency of force transfer. The decrease in force transfer would, in turn, reduce the percolation of force through the fiber network. This reduced connectivity and the

reduced area occupied by fibrils/fibers can be easily seen in the confocal images of the DS gels (Fig 3.7).

Although not a primary focus of this study, the Poisson's ratios were reported since they provide information regarding the structure of the fiber network [27]. Previous studies in collagen found that decreased Poisson's ratios were associated with larger fibers and less fiber connectivity [26]. The DS gels had larger fibers, less area coverage in the CRM images and lower Poisson's ratios, which is consistent with this observation. The nonlinear shape of the Poisson's ratio versus strain is a result of increasing fiber recruitment and has a similar shape to that predicted for random fiber networks [35]. According to analytic models, maximal Poisson's ratios will occur at a critical strain during the alignment of the initially random network, and decrease as fibers became more aligned. This is consistent with multiscale modeling studies that found progressive alignment of the collagen networks under strain [36]. This indicates that the collagen gels are behaving in a manner consistent with random fiber networks.

The maximal Poisson's ratios were similar between the control and decorin gels, implying a similar organization of the fiber networks. This suggests that something inherent to the increased fiber diameter is the source of the lowered mechanical strength, and not altered network organization. We hypothesize that, although the network organization is similar, larger fibers result in fewer network connections and a net decrease in force transmission, thus resulting in lower strength but unmodified Poisson's ratios.

One of the challenges in the current study was the automated measurement of the multiscale fibril organization. In the SEM images it was not possible to distinguish

individual fibrils within a fiber. However, it was possible to distinguish individual fibrils that were not in a fiber. Thresholding of the image resulted in touching and overlapping fibrils being grouped into a single fiber. Thus, only the fiber diameter distributions were able to be computed, which in many cases (e.g., the decorin containing gels) could be the fibril diameter. Likewise, the fibers and fiber bundles were difficult to distinguish, as often the fibers within a fiber bundle were not touching, resulting in their appearing as adjacent, but separate fibers. This resulted in the fiber diameter distributions of the control and DS gels overlapping for the SEM images, even though qualitative observations revealed that they had different organizations. Interestingly, image analysis of the CRM images did detect this difference. This is a result of the fact that the interfiber spacing in the bundles was too small to be resolved due to the diffraction limit of light. Thus, fiber bundles appeared as single fibers in the CRM images, resulting in distinctly different fiber diameter distributions between the control and DS gels. It was found that the 15000X images were most useful for resolving the fine scale differences between the decorin, core protein and control gels, while the 60X CRM images were most useful for resolving the differences between the DS and control gels. This highlights the importance of observing the fiber structure at multiple level of magnification, as the regulation of fibrillogenesis is clearly multiscale. Also noteworthy was a shift in magnitude of the fiber diameters between SEM and CRM, as previously described by Raub et al. [28]. CRM diameters were approximately an order of magnitude larger than that of SEM. This is due, in part, to the diffraction limit of light. The point spread function is proportional to the wavelength of light. Thus nanometer sized objects (i.e., fibrils) will appear larger than they actually are. The increased diameter has also

been ascribed to hydration of fibrils observed with CRM, and dehydrated fibrils/fibers observed using SEM.

In conclusion, it was found that decorin modifies the strength of collagen gels, and appears to do so by inhibiting the aggregation of fibrils into fibers. This information provides an approach to increase (or decrease in the case of DS) the material properties of collagen gels. Collagen and other types of hydrogels have been utilized as medium to deliver cells and other soluble factors to diseased or injured tissues. Inclusion of decorin within these constructs could possibly serve two functions: 1) increasing the strength of the constructs to better withstand surgical manipulation or in vivo mechanical forces and 2) the DS side chain of decorin can act as a reservoir for growth factors [10] exogenously added or secreted by implanted cells. The role of other SLRPs, including biglycan, in collagen gel mechanics is unknown. It is likely that they too alter the collagen fibril structure, but possibly in other ways.

References

[1] Provenzano, P. P., Heisey, D., Hayashi, K., Lakes, R., and Vanderby, R., Jr., 2002, "Subfailure Damage in Ligament: A Structural and Cellular Evaluation," J Appl Physiol, 92(1), pp. 362-71.

[2] Hassell, J. R., and Birk, D. E., "The Molecular Basis of Corneal Transparency," Exp Eye Res, 91(3), pp. 326-35.

[3] Banos, C. C., Thomas, A. H., and Kuo, C. K., 2008, "Collagen Fibrillogenesis in Tendon Development: Current Models and Regulation of Fibril Assembly," Birth Defects Res C Embryo Today, 84(3), pp. 228-44.

[4] Scott, J. E., 1988, "Proteoglycan-Fibrillar Collagen Interactions," Biochem J, 252(2), pp. 313-23.

[5] Silver, F. H., Freeman, J. W., and Seehra, G. P., 2003, "Collagen Self-Assembly and the Development of Tendon Mechanical Properties," J Biomech, 36(10), pp. 1529-53.

[6] Zhang, G., Ezura, Y., Chervoneva, I., Robinson, P. S., Beason, D. P., Carine, E. T., Soslowsky, L. J., Iozzo, R. V., and Birk, D. E., 2006, "Decorin Regulates Assembly of Collagen Fibrils and Acquisition of Biomechanical Properties During Tendon Development," J Cell Biochem, 98(6), pp. 1436-49.

[7] Robinson, P. S., Huang, T. F., Kazam, E., Iozzo, R. V., Birk, D. E., and Soslowsky, L. J., 2005, "Influence of Decorin and Biglycan on Mechanical Properties of Multiple Tendons in Knockout Mice," J Biomech Eng, 127(1), pp. 181-5.

[8] Lujan, T. J., Underwood, C. J., Henninger, H. B., Thompson, B. M., and Weiss, J. A., 2007, "Effect of Dermatan Sulfate Glycosaminoglycans on the Quasi-Static Material Properties of the Human Medial Collateral Ligament," J Orthop Res, 25(7), pp. 894-903.

[9] Kuc, I. M., and Scott, P. G., 1997, "Increased Diameters of Collagen Fibrils Precipitated in Vitro in the Presence of Decorin from Various Connective Tissues," Connect Tissue Res, 36(4), pp. 287-96.

[10] Ruhland, C., Schonherr, E., Robenek, H., Hansen, U., Iozzo, R. V., Bruckner, P., and Seidler, D. G., 2007, "The Glycosaminoglycan Chain of Decorin Plays an Important Role in Collagen Fibril Formation at the Early Stages of Fibrillogenesis," Febs J, 274(16), pp. 4246-55.

[11] Douglas, T., Heinemann, S., Bierbaum, S., Scharnweber, D., and Worch, H., 2006, "Fibrillogenesis of Collagen Types I, Ii, and Iii with Small Leucine-Rich Proteoglycans Decorin and Biglycan," Biomacromolecules, 7(8), pp. 2388-93.

[12] Iwasaki, S., Hosaka, Y., Iwasaki, T., Yamamoto, K., Nagayasu, A., Ueda, H., Kokai, Y., and Takehana, K., 2008, "The Modulation of Collagen Fibril Assembly and Its Structure by Decorin: An Electron Microscopic Study," Arch Histol Cytol, 71(1), pp. 37-44.

[13] Raspanti, M., Viola, M., Sonaggere, M., Tira, M. E., and Tenni, R., 2007, "Collagen Fibril Structure Is Affected by Collagen Concentration and Decorin," Biomacromolecules, 8(7), pp. 2087-91.

[14] Brightman, A. O., Rajwa, B. P., Sturgis, J. E., Mccallister, M. E., Robinson, J. P., and Voytik-Harbin, S. L., 2000, "Time-Lapse Confocal Reflection Microscopy of Collagen Fibrillogenesis and Extracellular Matrix Assembly in Vitro," Biopolymers, 54(3), pp. 222-34.

[15] Vogel, K. G., and Trotter, J. A., 1987, "The Effect of Proteoglycans on the Morphology of Collagen Fibrils Formed in Vitro," Coll Relat Res, 7(2), pp. 105-14.

[16] Pins, G. D., Christiansen, D. L., Patel, R., and Silver, F. H., 1997, "Self-Assembly of Collagen Fibers. Influence of Fibrillar Alignment and Decorin on Mechanical Properties," Biophys J, 73(4), pp. 2164-72.

[17] Danielson, K. G., Baribault, H., Holmes, D. F., Graham, H., Kadler, K. E., and Iozzo, R. V., 1997, "Targeted Disruption of Decorin Leads to Abnormal Collagen Fibril Morphology and Skin Fragility," J Cell Biol, 136(3), pp. 729-43.

[18] Farndale, R. W., Buttle, D. J., and Barrett, A. J., 1986, "Improved Quantitation and Discrimination of Sulphated Glycosaminoglycans by Use of Dimethylmethylene Blue," Biochim Biophys Acta, 883(2), pp. 173-7.

[19] Roeder, B. A., Kokini, K., Sturgis, J. E., Robinson, J. P., and Voytik-Harbin, S. L., 2002, "Tensile Mechanical Properties of Three-Dimensional Type I Collagen Extracellular Matrices with Varied Microstructure," J Biomech Eng, 124(2), pp. 214-22.

[20] D'amore, A., Stella, J. A., Wagner, W. R., and Sacks, M. S., "Characterization of the Complete Fiber Network Topology of Planar Fibrous Tissues and Scaffolds," Biomaterials, 31(20), pp. 5345-54.

[21] Vader, D., Kabla, A., Weitz, D., and Mahadevan, L., 2009, "Strain-Induced Alignment in Collagen Gels," PLoS One, 4(6), pp. e5902.

[22] Pourdeyhimi, B., and Dent, R., 1999, "Measuring Fiber Diameter Distribution in Nonwovens," Textile Research Journal, 69(4), pp. 233-236.

[23] Pourdeyhimi, B., Ramanathan, R., and Dent, R., 1996, "Measuring Fiber Orientation in Nonwovens. Part Ii: Direct Tracking," Textile Research Journal, pp. 747-753.

[24] Stein, A. M., Vader, D. A., Jawerth, L. M., Weitz, D. A., and Sander, L. M., 2008, "An Algorithm for Extracting the Network Geometry of Three-Dimensional Collagen Gels," J Microsc, 232(3), pp. 463-75.

[25] Kiraly, K., Lapvetelainen, T., Arokoski, J., Torronen, K., Modis, L., Kiviranta, I., and Helminen, H. J., 1996, "Application of Selected Cationic Dyes for the Semiquantitative Estimation of Glycosaminoglycans in Histological Sections of Articular Cartilage by Microspectrophotometry," Histochem J, 28(8), pp. 577-90.

[26] Roeder, B. A., Kokini, K., and Voytik-Harbin, S. L., 2009, "Fibril Microstructure Affects Strain Transmission within Collagen Extracellular Matrices," J Biomech Eng, 131(3), pp. 031004.

[27] Tatlier, M., and Berhan, L., 2009, "Modelling the Negative Poisson's Ratio of Compressed Fused Fibre Networks," Phys. Status Solidi B, 246(9), pp. 2018-2024.

[28] Raub, C. B., Suresh, V., Krasieva, T., Lyubovitsky, J., Mih, J. D., Putnam, A. J., Tromberg, B. J., and George, S. C., 2007, "Noninvasive Assessment of Collagen Gel Microstructure and Mechanics Using Multiphoton Microscopy," Biophys J, 92(6), pp. 2212-22.

[29] Shi, J. H., Liu, X. Y., Li, L. J., Strom, C. S., and Xu, H. Y., 2009, "Spherulitic Networks: From Structure to Rheological Property," J. Phys. Chem. B, 113, pp. 4549-4554.

[30] Kaya, M., Toyama, Y., Kubota, K., Nodasaka, Y., Ochiai, M., Nomizu, M., and Nishi, N., 2005, "Effect of DNA Structure on the Formation of Collagen-DNA Complex," Int J Biol Macromol, 35(1-2), pp. 39-46.

[31] Cheema, U., Chuo, C. B., Sarathchandra, P., Nazhar, N. S., and Brown, R. A., 2007, "Engineering Functional Collagen Scaffolds: Cyclid Loading Increases Material Strength and Fibril Aggregation," Advanced Functional Materials, 17, pp. 2426-2431.

[32] Craig, A. S., Birtles, M. J., Conway, J. F., and Parry, D. A., 1989, "An Estimate of the Mean Length of Collagen Fibrils in Rat Tail-Tendon as a Function of Age," Connect Tissue Res, 19(1), pp. 51-62.

[33] Orgel, J. P., Irving, T. C., Miller, A., and Wess, T. J., 2006, "Microfibrillar Structure of Type I Collagen in Situ," Proc Natl Acad Sci U S A, 103(24), pp. 9001-5.

[34] Raspanti, M., Viola, M., Forlino, A., Tenni, R., Gruppi, C., and Tira, M. E., 2008, "Glycosaminoglycans Show a Specific Periodic Interaction with Type I Collagen Fibrils," J Struct Biol, 164(1), pp. 134-9.

[35] Ateshian, G. A., Rajan, V., Chahine, N. O., Canal, C. E., and Hung, C. T., 2009, "Modeling the Matrix of Articular Cartilage Using a Continuous Fiber Angular Distribution Predicts Many Observed Phenomena," J Biomech Eng, 131(6), pp. 061003.

[36] Sander, E. A., Stylianopoulos, T., Tranquillo, R. T., and Barocas, V. H., 2009, "Image-Based Multiscale Modeling Predicts Tissue-Level and Network-Level Fiber Reorganization in Stretched Cell-Compacted Collagen Gels," Proc Natl Acad Sci U S A, 106(42), pp. 17675-80.

CHAPTER 4

MICROMECHANICAL MODELS OF HELICAL SUPERSTRUCTURES IN LIGAMENT AND TENDON FIBERS PREDICT LARGE POISSON'S RATIOS

Abstract

Experimental measurements of the Poisson's ratio in tendon and ligament tissue greatly exceed the isotropic limit of 0.5. This is indicative of volume loss during tensile loading. The microstructural origin of the large Poisson's ratios is unknown. It was hypothesized that a helical organization of fibrils within a fiber would result in a large Poisson's ratio in ligaments and tendons, and that this helical organization would be compatible with the crimped nature of these tissues, thus modeling their classic nonlinear stress-strain behavior. Micromechanical finite element models were constructed to represent crimped fibers with a super helical organization, composed of fibrils embedded within a matrix material. A homogenization procedure was performed to determine both the effective Poisson's ratio and the Poisson function. The results showed that helical fibril organization within a crimped fiber was capable of simultaneously predicting large Poisson's ratios and the nonlinear stress-strain behavior seen experimentally. Parametric studies revealed that the predicted Poisson's ratio was strongly dependent on the helical pitch, crimp angle and the material coefficients. The results indicated that, for physiologically relevant parameters, the models were capable of predicting the large

Poisson's ratios seen experimentally. It was concluded that helical organization within a crimped fiber can produce both the characteristic nonlinear stress strain behavior and large Poisson's ratios, while fiber crimp alone could only account for the nonlinear stress-strain behavior.

Introduction

Tendons and ligaments are fibrous, load bearing tissues that are characterized by a hierarchical organization of collagen microstructures. A basic structural component of ligaments and tendons is the collagen fibril. Fibrils are closely packed within an extrafibrillar proteoglycan rich matrix to form a fiber. Individual fibers are encased in the endotenon sheath and packed into fascular units, which then become the constituents of the whole tendon or ligament complex [1, 2] (Refer to Fig 2.1 in Chapter 2).

Although there is a wealth of literature on the elastic and viscoelastic behavior of ligaments and tendons, most studies have focused on uniaxial stress strain behavior and largely ignore volumetric behavior (e.g., Poisson's ratio). In biphasic theory, the compressibility of the solid phase is governed by the volumetric material coefficients in the constitutive model [3]. For uniaxial tensile loading in linear elasticity, the Poisson's ratio is a measure of volume change and describes the lateral contraction in response to an axial strain. The Poisson's ratio is strictly a kinematic measure, and can be defined both for the kinematically linear and nonlinear cases (generally referred to as the Poisson function in nonlinear theory), and applies to both isotropic and anisotropic materials. In the latter case, more than one Poisson's ratio must be defined.

The reported Poisson's ratios for tendon and ligament subjected to tensile loading along the fiber direction have ranged from 0.8 ±0.3 in rat tail tendon fascicles [4], to 2.0

± 1.9 in capsular ligament [5] and 2.98 ± 2.59 in bovine flexor tendon [6]. Under tensile loading, these large Poisson's ratios are indicative of volume loss, which may result in fluid exudation [7, 8].

The magnitude of volume loss and thus the quantity of fluid exuded during deformation may play an important role in the mechanics and function of these tissues. It has been suggested that biphasic theory may explain some if not all of the viscoelastic behavior of ligament and tendon [9, 10]. Furthermore, fluid transport resulting from mechanical forces may aid in nutrient delivery within these tissues. Finally, shear forces and or cell membrane deformation resulting from pressure driven fluid flux may be an important mechanotransduction signal for tenocytes and fibroblasts [11-13]. In light of this information, the volumetric behavior, and thus Poisson's ratio, is of fundamental importance in understanding healthy and diseased ligament and tendon tissue.

A number of studies have examined structure-function relationships between the fibrillar microstructure and macroscopic behavior of the "toe region" of ligaments and tendons under tensile loading [14-19]. However, there are no models in the literature that predict or explain the large Poisson's ratio of these tissues. A review of the literature on fiber based composites reveals that at least two microstructural fiber geometries are capable of generating large Poisson's ratios. One possibility is multiple fiber families crossing at nonorthogonal angles [20], but histological studies suggest that fibrils and fibers in most ligaments and tendons are predominantly aligned in a parallel fashion [21]. The other possibility is the helical arrangement of a fiber family [22].

Several studies have reported the presence of helical structures within fibers and fascicles of ligament and tendon. Yahia et al. presented histological evidence that

suggests the presence of a super helical organization of fibrils in canine patellofemoral tendon and ACL. An organizational scheme was suggested in which a helical twist was superimposed on top of crimp structures. The scale of this twist was suggested as being an order of magnitude larger than that of the crimp [23]. Studies by Vidal et al. have also presented histological evidence suggesting a super helical arrangement of fibrils [24-26]. It was suggested that this helical arrangement is difficult to see in standard preparations, which may account for their absence in past histological studies.

It was hypothesized that a micromechanical model with super helical fibril organization in the presence of crimp would predict the large Poisson's ratios seen experimentally while simultaneously predicting the nonlinear stress strain behavior of these tissues. The objective of this study was to use homogenization methods and finite element micromechanical models to test this hypothesis, as well as to assess the influence of material coefficients and geometric characteristics of the micromechanical model on the predicted Poisson's ratio.

Methods

Fiber geometry and unit cell

It was assumed that a fiber is the fundamental repeating structural unit within a tendon and ligament. For the purposes of homogenization, a single fiber unit was considered to be a periodic unit cell. Unit cells were modeled by embedding discrete fibrils within a more compliant matrix material and were assumed to be hexagonally packed within the fiber [13]. It was assumed that the matrix material modeled both the interfibrillar and interfiber space. The number of fibrils embedded within the fiber was varied as part of the study, with models featuring 7 to 91 discrete fibrils (Fig 4.1). The

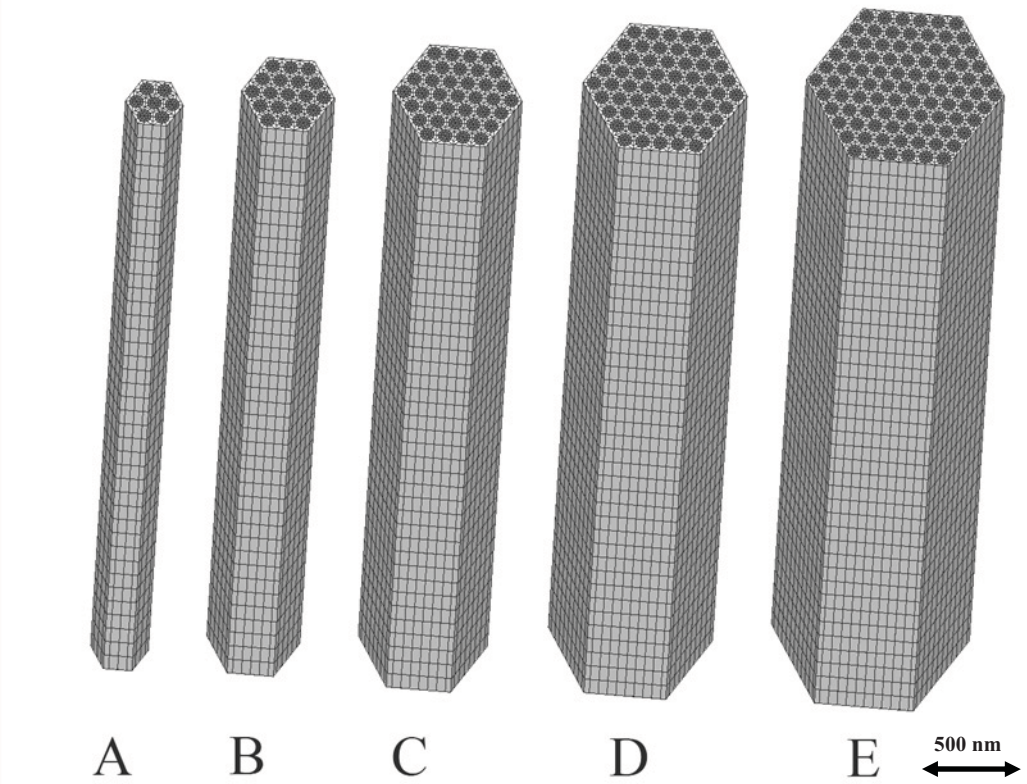

Figure 4.1: Models with varied fibril numbers. Separate models were constructed with 7, 19, 37, 61 and 91 discrete fibrils. Model C, which had 37 fibrils, was considered to be the base model and was used for most simulations.

fibril diameter was set to 100 nm, based on values reported in the literature for ligament and tendon [27]. The interfibrillar spacing was set to 25 nm [27], which generated a fibril volume fraction of 57%. The baseline model contained 37 fibrils (based on a convergence study described later in the text), had a diameter of 0.769 μm and a height of 8.0 μm. Transformations were applied to the baseline model to generate models with planar crimp, helical twisting and planar crimp models with a super helical twist (Fig 4.2).

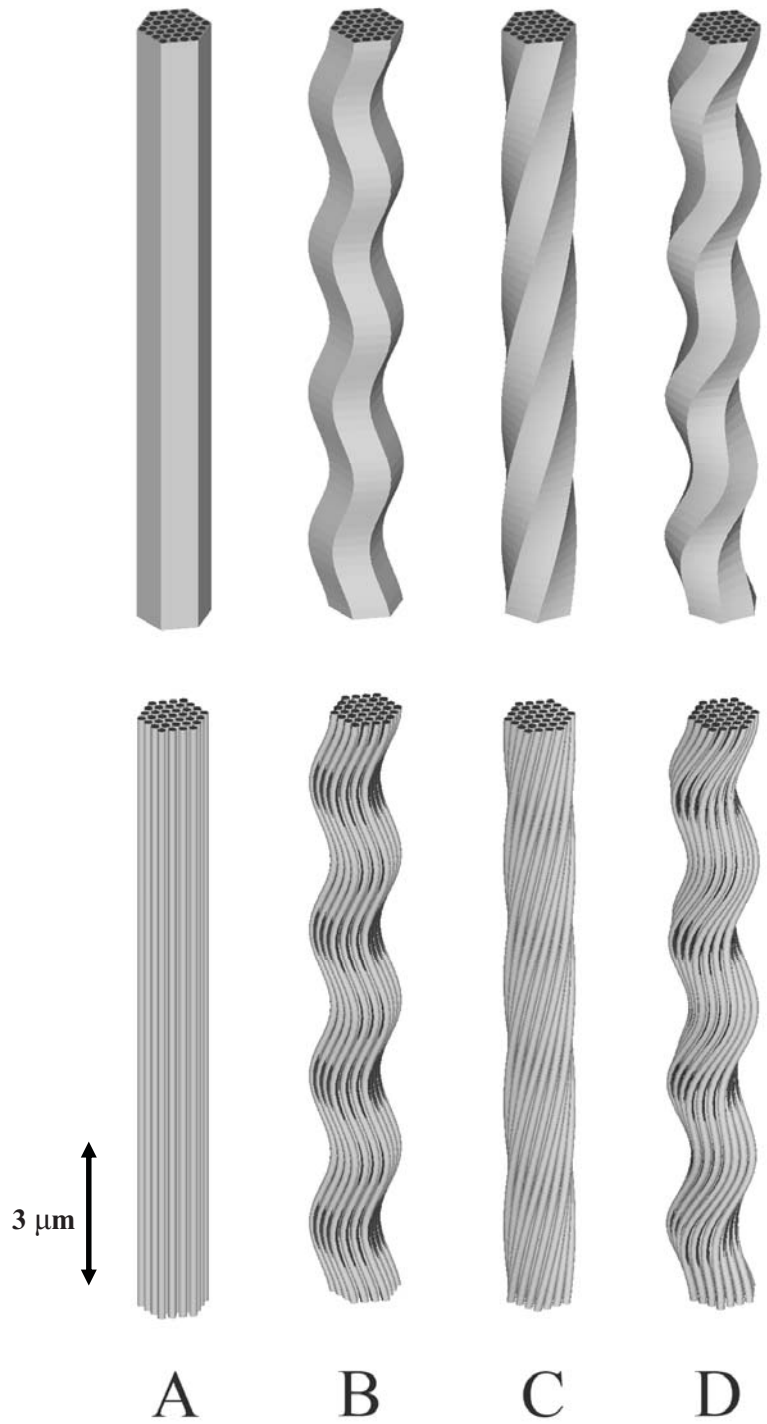

Figure 4.2: Model transformation types. (A) Untransformed model; (B) Planar crimp model; (C) Helically transformed model; (D) Helically transformed model combined with planar crimp. The top models show the full mesh while bottom models show just the fibrils with the matrix material removed.

Sinusoidal and helical transformation of unit cells

The most accepted geometric model of fiber crimp is planar crimp, in which the crimp plane is constant throughout the fiber and fascicle [28-30]. Planar crimp models were generated by applying a sinusoidal transformation of the following form along the fiber axis:

$$y' = y + A_\theta \sin\left(2\pi \frac{z}{\lambda}\right); \quad A_\theta = \frac{\lambda}{4}\tan\left(\theta_{crimp}\right) \tag{4.1}$$

where λ is the crimp period and θ_{crimp} is the crimp angle (Fig 4.3A). To accurately represent the crimp structures observed in histological studies [31-33], the models were scaled such that the ratio of the crimp period to fiber diameter was similar to that seen experimentally:

$$\frac{\lambda_{experiment}}{D_{experiment}} = \frac{\lambda_{model}}{D_{model}} \tag{4.2}$$

where $\lambda_{experiment}$ and $D_{experiment}$ are the experimentally measured crimp period and fiber diameter and λ_{model} and D_{model} are the model crimp period and model fiber diameter. Histologically measured values for the crimp period and fiber diameter vary between tendons and ligaments, as well as between studies. Table 4.1 provides values from the literature for rat tail tendon, rat MCL, human Achilles tendon and for the baseline model used in this study [30-34].

Helical models were generated with a mean fibril pitch (averaged over all fibrils) ranging from 0 to 60^o (Fig 4.3B). To generate the helical models, the mesh nodes were rotated an angle θ about the fiber axis such that a complete rotation was generated.

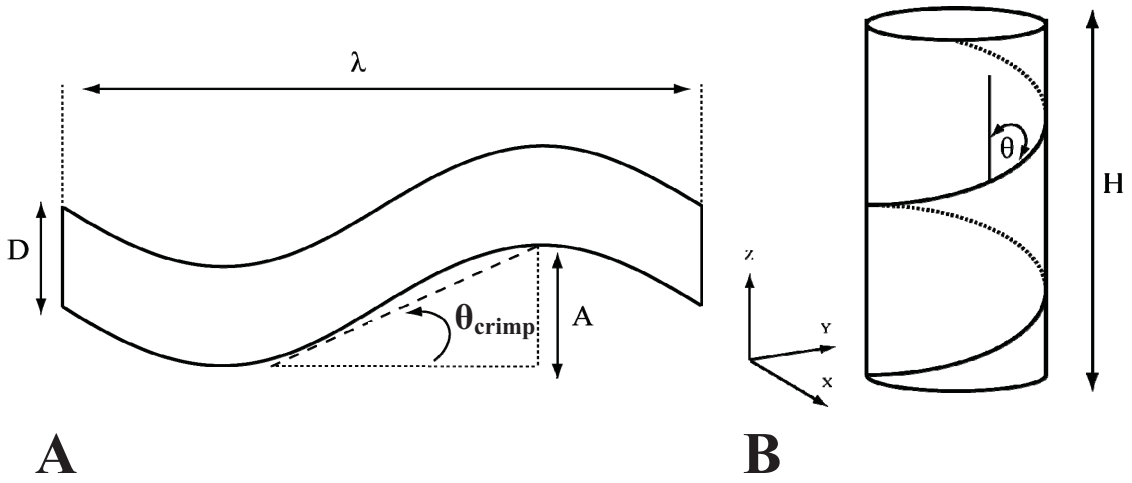

Figure 4.3: Geometric parameters of crimped and helical models. (A) A sinusoidally crimped fiber was defined by its diameter *D*, crimp angle θ_{crimp}, crimp amplitude *A* and crimp period λ. (B) The helical pitch angle was defined as the angle between the vertical (z) axis and the fibrils. All models shared the same coordinate system. The fiber axis was aligned with the z axis and the x-y plane was transverse to the fiber.

Table 4.1: Comparison of crimp parameters. Experimentally measured values of crimp period and fiber diameter for rat tail tendon, rat MCL and human Achilles tendon as compared to the values used in this study.

	λ	**D**	**λ/D**
Rat Tail Tendon	**150 µm**	**25 µm**	**6.00**
Rat MCL	**50 µm**	**20 µm**	**2.50**
Human Achilles Tendon	**230 µm**	**28.9 µm**	**8.0**
37 Fiber model	**2 µm**	**0.736 µm**	**2.72**

Since the diameter of a given fiber model was constant, the helical pitch was altered by changing the height of the model such that:

$$\theta_{pitch} = \frac{2\pi r}{H} \tag{4.3}$$

These models were then modified to include planar crimp superimposed with helical twist. The scaling of the models required that the length was a multiple of the crimp period, which restricted the possible model lengths and thus the helical pitch.

Constitutive model

Both the fibrils and matrix were modeled using an isotropic, compressible neo-Hookean hyperelastic constitutive model. This model was chosen because it is rotationally invariant and, in the limit of infinitesimal strains, the material coefficients can be cast in terms of the familiar linear material coefficients, namely the Young's modulus E and Poisson's ratio ν. The fibrils were assigned a Young's modulus of $E_f = 1$ GPa, which is consistent with experimental values in the literature [35]. Although published values are not available for the modulus of the matrix material E_m, Ault et al. estimated a value of 0.25 MPa using analytic micromechanical models [16]. With this guidance, a value of $E_m = 1.0$ MPa was assigned for the baseline models. Experimental values for the Poisson's ratios of the fibril and matrix have not been reported, so a value of $\nu_f = \nu_m = 0.3$ was assigned to the baseline model. The effect of the Young's modulus and Poisson's ratio were explored as part of a parametric study.

Discretization of the unit cell

Unit cells were constructed of fibrils embedded within a hexagonally shaped fiber using trilinear hexahedral elements and transformed according to Equations 4.1 and 4.3. A mesh convergence study was performed to determine the optimal mesh density. Since a large number of elements was needed to discretize the domain, a tradeoff was made between model accuracy and model size. Model size was limited by practical constraints such as memory and computation time, while accuracy was affected by the mesh density. The convergence study revealed that the final meshes used in the study (111,000 elements and 144,635 nodes for the largest 37 fibril model) resulted in errors of less than 12% as compared to more refined meshes.

Homogenization procedure and FE analysis

To obtain effective material properties, periodic boundary conditions were applied to the transformed unit cells. Briefly, periodic boundary conditions require that opposing faces deform identically and that boundary tractions are antiperiodic. The so called master node approach was used to enforce the kinematic requirement of identically deforming faces [36-39]. Refer to Appendix A for a complete description of the periodic boundary conditions used. It was not necessary to enforce the requirement for anti-periodic tractions directly, as previous work has shown that for displacement based FEM solvers this constraint is automatically satisfied when the kinematic constraints are met [39]. Additional boundary conditions were also applied to the models to prevent rigid body translation and rotation. To prevent translation, the center node on the top and bottom face were constrained in the x-y plane. To prevent rotation, an appropriate edge node on the top face was constrained in the x-direction and an appropriate edge node on the bottom face was constrained in the y direction. Tensile loading was simulated by applying prescribed displacements in the axial direction to the master nodes on the top and bottom faces of the model. All finite element analysis was conducted using the nonlinear FE solver FEBio (http://mrl.sci.utah.edu/software.php). The periodic boundary conditions were implemented as linear constraint equations and enforced using an augmented Lagrangian method.

The untransformed models (straight fiber unit cells) and the sinusoidally transformed models (crimped fiber unit cells) were perfectly periodic. After helical transformation, the models lose their perfect periodicity. However, opposing faces can still be constrained to deform identically if the linear constraint equations are transformed

into a helical coordinate system. With the loss of perfect periodicity, the effective material properties become approximate. The small error introduced by this approximation will be addressed in the discussion.

Effective Poisson's ratio

This study focused primarily on obtaining the effective Poisson's ratio (the Poisson function computed near a reference configuration, $\lambda_a = 1$). However, the Poisson function was also obtained for a number of models over a large range of finite strains. The Poisson function $v(\lambda_a)$ [40] is given by:

$$v(\lambda_a) = -\frac{\varepsilon_t(\lambda_a)}{\varepsilon_a(\lambda_a)} = \frac{1-\lambda_t}{\lambda_a - 1} \tag{4.4}$$

where ε_a and λ_a are the engineering strain and stretch ratio in the fiber direction and ε_t and λ_t are the engineering strain and stretch ratio transverse to the fiber direction. This reduces to the Poisson's ratio v_0 at small strains:

$$v_0 = \lim_{\lambda_a \to 1} v(\lambda_a) \,. \tag{4.5}$$

$v(\lambda_a)$ and v_0 were determined by subjecting the unit cell to simulated tensile loading. To obtain v_0, an axial strain of 0.5% was applied. Note that the small strain allows for the linear coefficient, the Poisson's ratio, to be obtained. However, the use of the nonlinear constitutive model for the fibril and matrix made these models intrinsically nonlinear. To obtain $v(\lambda_a)$, strains of up to 8% were applied.

λ_a was computed from the prescribed axial displacements, and λ_t was computed from the nodal displacements of the master nodes for each face. For the crimped models, the presence of a crimping plane transformed the models from transverse isotropy (caused by the presence of the fibrils) to orthotropic isotropy. This led to the presence of two different Poisson's ratios, v_{xz} and v_{yz}. Pilot testing revealed that this additional anisotropy within the helically twisted crimp models was relatively small, with the ratio of v_{xz}/v_{yz} typically close to unity. Therefore v_0 and $v(\lambda_a)$ were computed to be the average of the two, making the effective properties those of transverse isotropy.

Parametric studies

Parametric studies were performed to determine the effects of θ_{pitch}, θ_{crimp}, E_m, ν_m, ν_f and fibril number. θ_{pitch} was varied between 0^o and 60^o. E_m was varied such that the ratio of the fiber to matrix modulus (the modulus ratio, $M_r=E_f/E_m$) spanned five orders of magnitude, while the ratio of the fiber to matrix Poisson's ratio (the compressibility ratio, $C_r = v_f / v_m$) was varied between 1.0 and 30.0. The number of fibrils was varied from 7 to 91 to determine the validity of extrapolating the results from the baseline model with 37 fibrils to real fibers, which typically contain many thousands of fibrils.

Results

Nonlinear stress strain behavior

Fig 4.4A shows stress strain curves for the baseline model featuring crimp angles of 10, 15 and 20 degrees. A classic "uncrimping" behavior was predicted, with an initial nonlinear toe region changing to a linear region at the so-called transition strain.

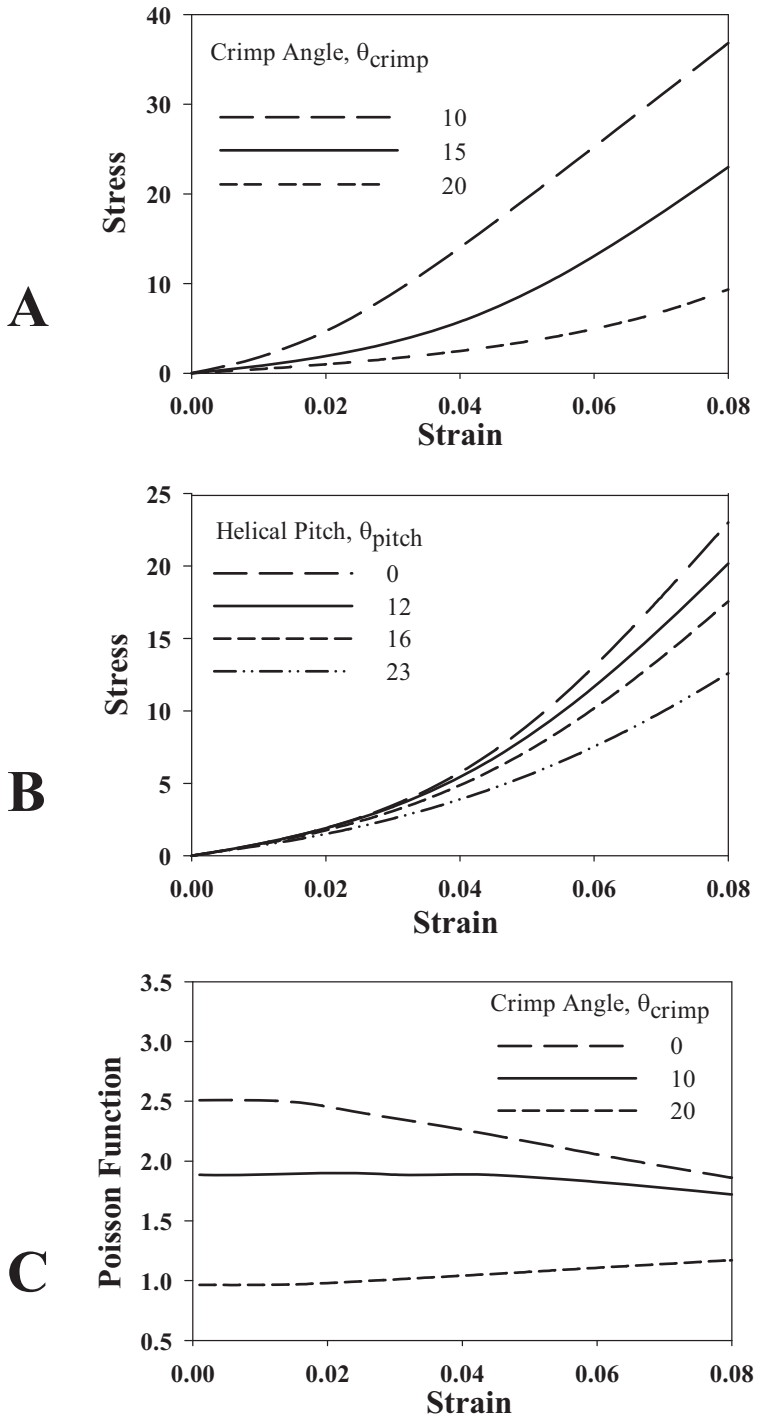

Figure 4.4: Extensional behavior of the models. (A) Plot of the stress vs. strain for models with θ_{crimp} =10, 15 and 20 degrees. (B) Plot of the stress vs. strain for crimped models (θ_{crimp}=15 degrees) with a helical pitch of θ_{pitch} = 0, 12, 16 and 23 degrees. (C) The Poisson function plotted vs. strain for models with crimp angles of θ_{crimp} = 0, 10 and 20 degrees (θ_{pitch} =23 degrees).

Increasing θ_{crimp} increased the length of the toe region and the magnitude of the transition strain. Adding a super helical organization to the crimped models did not affect the length of the toe region, but did change the slope of the linear region (Fig 4.4B).

Poisson function

The Poisson function $v(\lambda_a)$ for the baseline model (θ_{pitch}=23°) is shown in Fig 4.4C for three different crimp angles. In helical models with no crimp (θ_{crimp}=0), $v(\lambda_a)$ decreased with increasing strain. This is a result of the fibrils progressively compressing until they are almost in contact. In models with moderate crimp (θ_{crimp}=10), $v(\lambda_a)$ was nearly constant until about 6% strain, at which point it also decreased. In models with large crimp (θ_{crimp}=20), $v(\lambda_a)$ increased with increasing strain and then leveled off in the linear region.

Effect of helical pitch and crimp angle on

effective Poisson's ratio

There was a nonlinear relationship between the effective Poisson's ratio v_0 and the mean helical pitch angle θ_{pitch}. At θ_{pitch} = 0 (straight fibers), v_0 was the volume average of the matrix and fibril Poisson's ratio (v_0 = 0.3). As θ_{pitch} increased, v_0 increased until a transition angle was reached, at which point v_0 again decreased until the so called "neutral angle" was attained and the volume averaged Poisson's ratio was once again observed. This is seen in the top curve of Fig 4.5A, which represents the results for a helical model with θ_{crimp} = 0° (no crimp). For the baseline model with 37 fibrils and a

modulus ratio of M_r =10^3, a maximum value of v_0 = 2.5 was obtained at θ_{pitch} = 17.5°. Poisson's ratios exceeding the isotropic limit of 0.5 were obtained for angles greater than 1.7°.

As the crimp angle θ_{crimp} was increased from 0°, the maximum effective Poisson's ratio decreased and the optimal pitch angle increased. For a θ_{crimp} = 5°, a maximum v_0 of 2.2 occurred at an optimal pitch angle of θ_{pitch} = 19°, while θ_{crimp} = 10° resulted in a maximum v_0 of 1.6 at an optimal pitch of θ_{pitch} = 21°. This trend continued for crimp angles of 15°, 20°, 25°, 30° and 35°, which had maximum Poisson's ratios of 1.6, 0.9, 0.7, 0.6 and 0.45 for optimal angles of 23°, 29°, 36°, 39° and 40° (Fig 4.5A). All crimp angles except for the 35° crimp were capable of generating Poisson's ratios larger than the isotropic limit.

Parametric studies

Real tendon and ligament fibers contain many hundreds if not thousands of fibrils. To determine the applicability of the baseline RVE fiber model with 37 fibrils to real fibers, a convergence study was performed on the fibril number. As shown in Fig 4.6A, the effective Poisson's ratio asymptoted as the number of fibrils was increased (θ_{pitch} held constant for all models). This important result indicates that large aggregates of fibrils can be modeled with a smaller number of fibrils as long as θ_{pitch} is kept constant. The increase in Poisson's ratio with increasing number of fibrils likely resulted from two model artifacts. The first artifact is the center fibril, which is straight and thus does not contribute to the transverse compressive forces that generate the large Poisson's ratios.

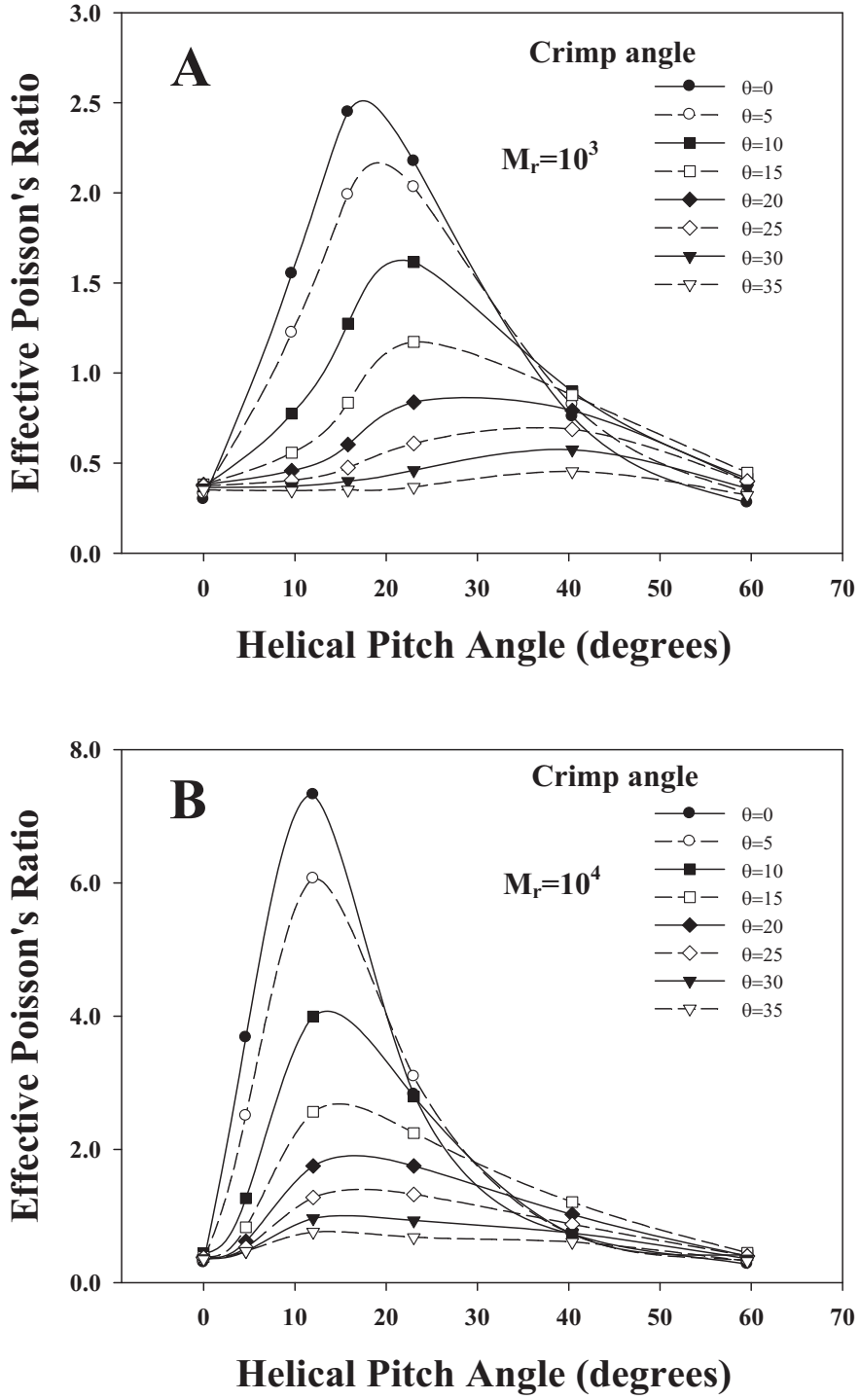

Figure 4.5:. Sensitivity of Poisson's ratios to helical pitch and material properties. (A) The effective Poisson's ratio plotted as a function of mean helical pitch for models with a modulus ratio of $M_r=10^3$. (B) The effective Poisson's ratio as a function of mean helical pitch for models with a modulus ratio of $M_r=10^4$. The top curve in both plots corresponds to a helical crimp of 0^o, with successive curves featuring an increase in crimp angle by 5^o until an angle of 35^o is reached at the bottom.

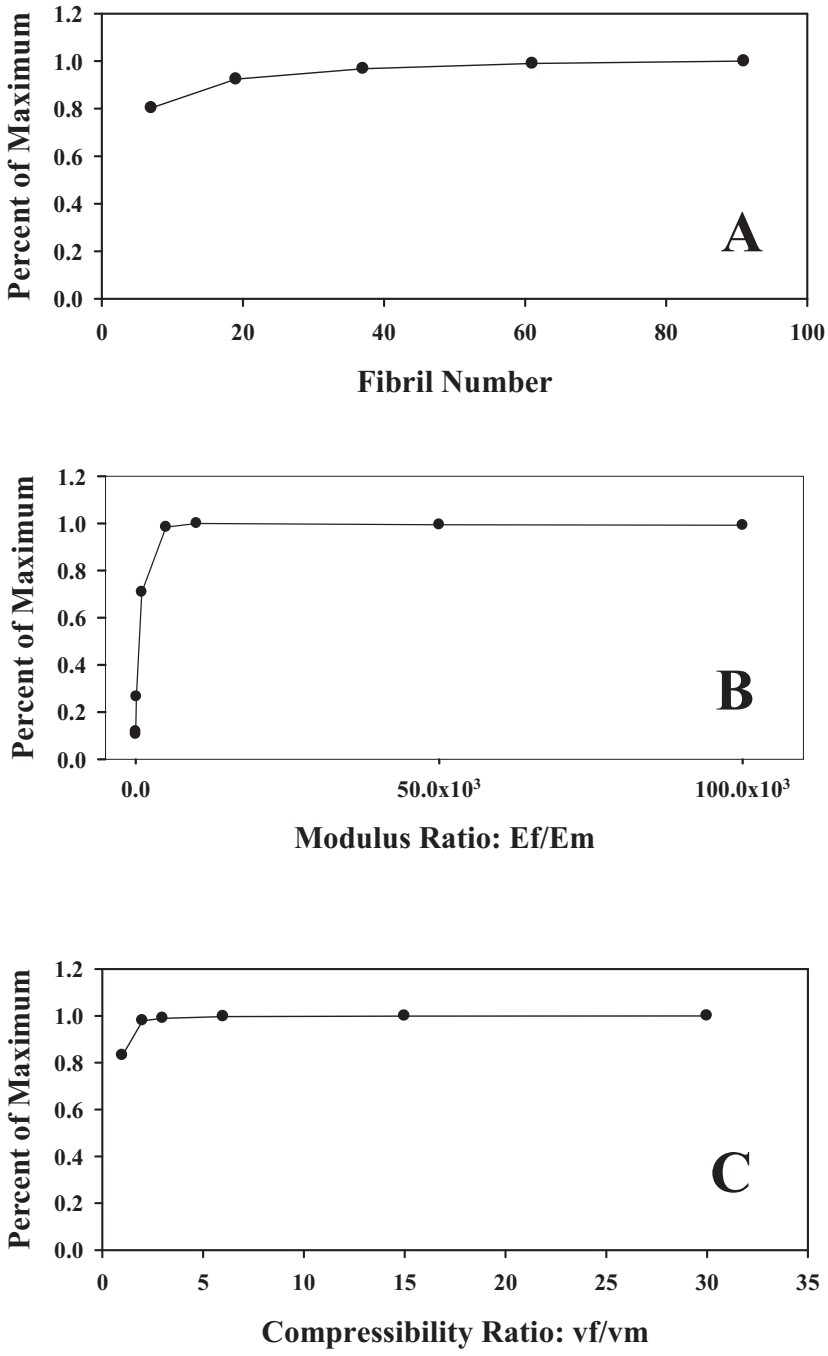

Figure 4.6: Parametric studies**.** (A) The percent of the maximum Poisson's ratio plotted as a function of the total number of fibrils. The mean pitch for all models was 15^{o} and the modulus ratio was 10^4. (B) Sensitivity of the effective Poisson's ratio to changes in the modulus ratio. Mean pitch = 23^{o} and compressibility ratio C_r= 1. (C) Sensitivity of the effective Poisson's ratio to changes in the compressibility ratio. Mean pitch = 23^{o} and modulus ratio M_r =10^4.

The other source of artifact is the model edges, which contain only matrix material. As the number of fibrils is increased, the effects of these artifacts become negligible.

The effective Poisson's ratio was also sensitive to the modulus ratio M_r (Fig 4.5A, 4.6B). As M_r was increased, the maximum v_0 also increased until a value of M_r=5000 was reached, at which point it asymptoted (Fig 4.6B). The results in Fig 4.6B are for a helical model with no crimp, but increasing M_r in the crimped models had a similar effect. In addition to increasing the maximum v_0, M_r also affected the transition pitch angle and the shape of the Poisson's ratio vs. pitch curve (Fig 4.5B). Interestingly, as M_r was increased, not only did the transition angle shift left, but the maximum v_0 at that angle also increased. For $M_r = 10^4$ values for v_0 were as large as 7.3 at the optimal angle of 12^o.

The effective Poisson's ratio v_0 was also sensitive to the compressibility ratio, C_r (Fig 4.6C). Varying C_r had the same effect as varying M_r in that a quick increase was seen, followed by asymptotic behavior. Unlike M_r, however, the magnitude of this effect was considerably less.

Discussion

Micromechanical models were capable of reproducing the classic "uncrimping" stress-strain behavior of tendon and ligament tissue while simultaneously generating Poisson's ratios that were in agreement with experimental data. The length of the toe region was affected by the crimp angle, which is consistent with the results from a previous micromechanical model [16]. The Poisson function also depended on the crimp angle. Although little experimental data on the Poisson function for tendon and ligament

tissue are available, it was noted by Lynch et al. (2003) that the Poisson's ratio for sheep flexor tendon was constant. The model with a 10 degree crimp angle was capable of generating a curve with a nearly constant Poisson's ratio (Fig 4.4C).

The largest determining factors for the magnitude of the effective Poisson's ratio in the helical models were the mean helical pitch and the ratio of the fiber modulus to the matrix modulus. The dependence on the mean helical pitch qualitatively agrees with results for center filled, helically wound cylindrical tubes [22]. The largest Poisson's ratios were generated for a pitch angle between 12 to 18 degrees. However, Poisson's ratios greater than the isotropic limit were predicted even for small pitch angles.

The value of the matrix modulus was explored in sensitivity studies, as no direct measurements were available. It has been suggested that the matrix modulus may be many orders of magnitude smaller than the fiber modulus [16]. Ault et al. estimated the matrix modulus to be 0.25 MPa and the fiber modulus to be 2 GPa by using an analytic micromechanical model that coupled crimped fibrils to the matrix material, which provides a modulus ratio of 8,000. Although not a direct measurement of matrix modulus, the compressive modulus for MCL ligament as computed from published data provided a modulus of 0.05 MPa, while the modulus in the fiber direction for MCL has been measured as approximately 300 MPa [41, 42]. This provides an approximate modulus ratio of 6000. Based on this information, it seems reasonable to assume that the modulus ratio is large enough to be in the asymptotic region (M_r>5,000) (Fig 4.6B).

The planar crimp models predicted lower effective Poisson's ratios than the helical models. This can be interpreted in light of the fact that the uncrimping of the fiber will tend to decrease the tensile stress within the helically wound fibrils. This leads to a

decrease in the compressive forces, which then leads to a decrease in the Poisson's ratios. In a study on the homogenization of crimped composite structures by Garnich et al., the average Poisson's ratio never exceeded the isotropic limit, showing that planar crimp alone is not capable of generating large Poisson's ratios [38]. This was confirmed in the present study.

Although the predicted Poisson's ratio was sensitive to the modulus ratio, pitch angle and crimp angle, physiologically relevant parameters predicted large Poisson's ratios. Models of both crimped and uncrimped unit cells were capable of predicting Poisson's ratios within the range of those seen experimentally, but they were strongly dependent on the crimp angle. Reported values for the crimp angle vary greatly across the literature, ranging from 10^{o} to 60^{o}, depending on the tissue and study [30-34] . The models in the present study will only predict large Poisson's ratios if the crimp angle is in the low end of this range. It is interesting to note that previous micromechanical studies all required smaller crimp angles (10-20 degrees) to match experimental data [16, 19].

In this study, the helical transformation of the unit cell models resulted in a loss of perfect periodicity. To determine the magnitude of error introduced by this approximation, a verification study was performed in which the helically transformed unit cell models were compared to perfectly periodic unit cells with embedded helical fibrils. The latter models were constructed by embedding a cylindrical mesh of helically twisted fibrils into a mesh of a hexagonal unit cell with a cylindrical hole. The two meshes were nonconforming. Therefore tied surface constraints were used to connect the two meshes. Results of this study indicated that the maximum error for the helically transformed models was 8%, with the errors for most models being much less. The

addition of a tied surface constraint required meshes with higher resolutions and thus considerably longer solution time. Furthermore, the tied surface constraint introduced another possible source of discretization error.

The current study assumed that the material symmetry of the individual collagen fibrils was isotropic, but it has been suggested that individual collagen fibrils may be anisotropic [35]. It is also possible that a helical organization exists at a hierarchical level above that of the fiber. It was noted by Screen et al. that when individual rat tail tendon fascicles were subjected to tension in the fiber direction a nonnegligible amount of rotation was present [43]. This suggests that fibers themselves may be helically oriented within the fascicle. Finally, it is possible that other mechanisms, namely fiber crossing, interweaving or linking may contribute to the large Poisson's ratios.

In conclusion, this study demonstrated that microstructural models of ligaments and tendons with a super helical organization of fibrils within a crimped fiber are capable of predicting the large Poisson's ratios measured experimentally. Furthermore, these models were capable of reproducing the nonlinear stress strain behavior seen experimentally. Although the results of this study lend credibility to the hypothesis that helical organization of fibrils may provide a structure-function relationship between tissue microstructure and large Poison's ratios, experimental validation is necessary to confirm or refute this. The novel methodology developed for this study may provide a useful starting point for modeling helical microstructures in other biological tissues and composites.

References

[1] Kastelic, J., Galeski, A., and Baer, E., 1978, "The Multicomposite Structure of Tendon," Connect Tissue Res, 6(1), pp. 11-23.

[2] Kannus, P., 2000, "Structure of the Tendon Connective Tissue," Scand J Med Sci Sports, 10(6), pp. 312-20.

[3] Mow, V. C., Kuei, S. C., Lai, W. M., and Armstrong, C. G., 1980, "Biphasic Creep and Stress Relaxation of Articular Cartilage in Compression? Theory and Experiments," J Biomech Eng, 102(1), pp. 73-84.

[4] Screen, H. R. C., and Cheng, V. W. T., 2007, "The Micro-Structural Strain Response of Tendon," Journal of Material Science, 19, pp. 1-2.

[5] Hewitt, J., Guilak, F., Glisson, R., and Vail, T. P., 2001, "Regional Material Properties of the Human Hip Joint Capsule Ligaments," J Orthop Res, 19(3), pp. 359-64.

[6] Lynch, H. A., Johannessen, W., Wu, J. P., Jawa, A., and Elliott, D. M., 2003, "Effect of Fiber Orientation and Strain Rate on the Nonlinear Uniaxial Tensile Material Properties of Tendon," J Biomech Eng, 125(5), pp. 726-31.

[7] Wellen, J., Helmer, K. G., Grigg, P., and Sotak, C. H., 2004, "Application of Porous-Media Theory to the Investigation of Water Adc Changes in Rabbit Achilles Tendon Caused by Tensile Loading," J Magn Reson, 170(1), pp. 49-55.

[8] Adeeb, S., Ali, A., Shrive, N., Frank, C., and Smith, D., 2004, "Modelling the Behaviour of Ligaments: A Technical Note," Comput Methods Biomech Biomed Engin, 7(1), pp. 33-42.

[9] Yin, L., and Elliott, D. M., 2004, "A Biphasic and Transversely Isotropic Mechanical Model for Tendon: Application to Mouse Tail Fascicles in Uniaxial Tension," J Biomech, 37(6), pp. 907-16.

[10] Atkinson, T. S., Haut, R. C., and Altiero, N. J., 1997, "A Poroelastic Model That Predicts Some Phenomenological Responses of Ligaments and Tendons," J Biomech Eng, 119(4), pp. 400-5.

[11] Lavagnino, M., Arnoczky, S. P., Kepich, E., Caballero, O., and Haut, R. C., 2008, "A Finite Element Model Predicts the Mechanotransduction Response of Tendon Cells to Cyclic Tensile Loading," Biomech Model Mechanobiol, 7(5), pp. 405-16.

[12] Butler, S. L., Kohles, S. S., Thielke, R. J., Chen, C., and Vanderby, R., 1997, "Interstitial Fluid Flow in Tendons or Ligaments: A Porous Medium Finite

Element Simulation," Medical and Biological Engineering and Computing, 35(6), pp. 742-746.

[13] Chen, C. T., Malkus, D. S., and Vanderby, R., Jr., 1998, "A Fiber Matrix Model for Interstitial Fluid Flow and Permeability in Ligaments and Tendons," Biorheology, 35(2), pp. 103-18.

[14] Freed, A. D., and Doehring, T. C., 2005, "Elastic Model for Crimped Collagen Fibrils," J Biomech Eng, 127(4), pp. 587-93.

[15] Diamant, J., Keller, A., Baer, E., Litt, M., and Arridge, R. G., 1972, "Collagen; Ultrastructure and Its Relation to Mechanical Properties as a Function of Ageing," Proc R Soc Lond B Biol Sci, 180(60), pp. 293-315.

[16] Ault, H. K., and Hoffman, A. H., 1992, "A Composite Micromechanical Model for Connective Tissues: Part Ii--Application to Rat Tail Tendon and Joint Capsule," J Biomech Eng, 114(1), pp. 142-6.

[17] Lanir, Y., 1978, "Structure-Strength Relationships in Mammalian Tendon," Biophysical Journal, 24, pp. 541-554.

[18] Hurschler, C., 1997, "A Structurally Based Stress-Stretch Relationship for Tendon and Ligament," J Biomech Eng, 119(4), pp. 392-399.

[19] Grytz, R., and Meschke, G., 2009, "Constitutive Modeling of Crimped Collagen Fibrils in Soft Tissues," J Mech Behav Biomed Mater, 2(5), pp. 522-33.

[20] Peel, L. D., 2007, "Exploration of High and Negative Poisson's Ratio Elastomer-Matrix Laminates," Physica Status Solidi, 244(3), pp. 988-1003.

[21] Provenzano, P. P., and Vanderby, R., Jr., 2006, "Collagen Fibril Morphology and Organization: Implications for Force Transmission in Ligament and Tendon," Matrix Biol, 25(2), pp. 71-84.

[22] Marklund, E., 2007, "Doctoral Thesis: Modeling the Mechanical Performance of Natural Fiber Composites," Lulea University of Technology, Department of Applied Physics and Mechanical Engineering, pp. 151-178.

[23] Yahia, L. H., and Drouin, G., 1989, "Microscopical Investigation of Canine Anterior Cruciate Ligament and Patellar Tendon: Collagen Fascicle Morphology and Architecture," J Orthop Res, 7(2), pp. 243-51.

[24] Vidal Bde, C., 1995, "Crimp as Part of a Helical Structure," C R Acad Sci III, 318(2), pp. 173-8.

[25] Vidal, D. C., 2003, "Image Analysis of Tendon Helical Superstructure Using Interference and Polarized Light Microscopy," Micron, 34(8), pp. 423-432.

[26] Vidal Bde, C., and Mello, M. L., 2009, "Structural Organization of Collagen Fibers in Chordae Tendineae as Assessed by Optical Anisotropic Properties and Fast Fourier Transform," J Struct Biol, 167(2), pp. 166-75.

[27] Baek, G. H., Carlin, G. J., Vogrin, T. M., Woo, S. L., and Harner, C. D., 1998, "Quantitative Analysis of Collagen Fibrils of Human Cruciate and Meniscofemoral Ligaments," Clin Orthop Relat Res, (357), pp. 205-11.

[28] Rowe, R. W., 1985, "The Structure of Rat Tail Tendon," Connect Tissue Res, 14(1), pp. 9-20.

[29] Hansen, K. A., Weiss, J. A., and Barton, J. K., 2002, "Recruitment of Tendon Crimp with Applied Tensile Strain," J Biomech Eng, 124, pp. 72.

[30] Gathercole, L. J., and Keller, A., 1991, "Crimp Morphology in the Fibre-Forming Collagens," Matrix, 11(3), pp. 214-34.

[31] Hansen, K. A., Weiss, J. A., and Barton, J. K., 2002, "Recruitment of Tendon Crimp with Applied Tensile Strain," J Biomech Eng, 124(1), pp. 72-7.

[32] Hurschler, C., Provenzano, P. P., and Vanderby, R., Jr., 2003, "Scanning Electron Microscopic Characterization of Healing and Normal Rat Ligament Microstructure under Slack and Loaded Conditions," Connect Tissue Res, 44(2), pp. 59-68.

[33] Jarvinen, T., Jarvinen, T. L., Kannus, P., Jozsa, L., and Jarvinen, M., 2004, "Collagen Fibres of the Spontaneously Ruptured Human Tendons Display Decreased Thickness and Crimp Angle," Journal of Orthopaedic Research, 22(6), pp. 1303-1309.

[34] Franchi, M., Fini , M., Quaranta, M., De Pasquale , V., Raspanti, M., Giavaresi, G., Ottani , V., and Ruggeri, A., 2007, "Crimp Morphology in Relaxed and Stretched Rat Achilles Tendon," Journal of Anatomy, 210(1), pp. 1-7.

[35] Wenger, M. P., Bozec, L., Horton, M. A., and Mesquida, P., 2007, "Mechanical Properties of Collagen Fibrils," Biophys J, 93(4), pp. 1255-63.

[36] Pahr Dh, R. F., 2006, "Buckling of Honeycomb Sandwiches:Periodic Finite Element Considerations," CMES Comp Model Eng, 12, pp. 229-242.

[37] Pahr, D. H., and Zysset, P. K., 2008, "Influence of Boundary Conditions on Computed Apparent Elastic Properties of Cancellous Bone," Biomech Model Mechanobiol, 7(6), pp. 463-76.

[38] Garnich, M. R., and Karami, G., 2004, "Finite Element Micromechanics for Stiffness and Strength of Wavy Fiber Composites," Journal of Composite Materials, 38(4), pp. 273.

[39] Xia, Z., Zhou, C., Yong, Q., and Wang, X., 2006, "On Selection of Repeated Unit Cell Model and Application of Unified Periodic Boundary Conditions in Micro-Mechanical Analysis of Composites," International Journal of Solids and Structures, 43(2), pp. 266-278.

[40] Beatty, M. F., and Stalnaker, D. O., 1986, "The Poisson Function of Finite Elasticity," Journal of Applied Mechanics 53(4), pp. 807-813.

[41] Weiss, J. A., 2000, "Behavior of Human Medial Collateral Ligament in Unconfined Compression," Othopaedic Research Society 46th Annual Meeting, pp.

[42] Gardiner, J. C., and Weiss, J. A., 2003, "Subject-Specific Finite Element Analysis of the Human Medial Collateral Ligament During Valgus Knee Loading," J Orthop Res, 21(6), pp. 1098-106.

[43] Screen, H. R. C., Bader, D. L., Lee, D. A., and Shelton, J. C., 2004, "Local Strain Measurement within Tendon," Strain, 40(4), pp. 157-163.

CHAPTER 5

THE FLUID DEPENDENT MECHANISM DESCRIBED BY BIPHASIC THEORY MAY EXPLAIN THE APPARENT VISCOELASTICITY OF SINGLE TENDON FASCICLES

Abstract

The underlying mechanisms for the viscoelastic behavior of tendon and ligament tissue are poorly understood. It has been suggested that both fluid dependent and independent contributions may be present at different structural levels. We hypothesized that the stress relaxation response of a single fascicle is consistent with the fluid dependent mechanisms described by biphasic theory. To test this hypothesis, force, transverse strain and Poisson's ratio were measured as a function of time during stress relaxation testing of six rat tail tendon fascicles from Sprague Dawley rats. The mean equilibrium value of the Poisson's ratio was 4.26±1.53, which corresponded to an estimated 16.4% volume loss. As predicted by biphasic theory, the transverse strain and Poisson's ratio were time dependent, a large volume loss was seen at equilibrium and a linear correlation was found to exist between the force and Poisson's ratio during stress relaxation. These results suggest that the fluid dependent mechanism described by biphasic theory may explain some or all of the apparent viscoelastic behavior of single fascicles.

Introduction

The viscoelastic behavior of ligaments and tendons is thought to play an important role in the normal function of these tissues. The time and rate dependent behaviors are manifested as stress relaxation, creep and hysteresis. It is believed that the viscoelastic properties dissipate energy and thus protect the tissue from damage [1]. Experimentally observed changes in viscoelastic behavior in damaged and disease tissue highlights the importance of understanding the rate and time dependence [2, 3]. In spite of this importance, little is known about the underlying source of the apparent viscoelastic behavior.

Discerning the source of this behavior is complicated by the multiscale structural organization and high level of hydration in these tissues. Stress relaxation mechanisms may be both fluid dependent and independent, and may occur at different structural levels [4-9]. Rate dependent behavior has been observed at the fibril level, fiber level, fascicle level and tissue level [4, 8, 10, 11]. This study focuses on the viscoelastic behavior at the fascicle level, and more specifically, the fluid dependent mechanisms. Understanding the fascular response is fundamental to understanding the macroscopic tissue response and was deemed a prudent starting point in understanding the multiscale viscoelastic behavior of tendon and ligament tissue.

It has been suggested that biphasic theory may explain the apparent viscoelastic behavior of single fascicles [9]. According to biphasic theory, apparent viscoelasticity is a result of energy dissipated from fluid flux through a porous solid phase [12, 13]. This fluid flux is driven by volume strain governed by the Poisson's ratio of the elastic solid phase. During stress relaxation, biphasic theory predicts a time dependent lateral

contraction, which would be manifested experimentally as a time dependent Poisson's ratio. Furthermore, biphasic theory predicts that the stress during relaxation should be proportional to the lateral contraction. These observations regarding biphasic theory have motivated our hypothesis that during stress relaxation, single fascicles will display a time dependent lateral strain and Poisson's ratio, a large volume loss at equilibrium and a correlation between stress and Poisson's ratio.

To test this hypothesis, the force, transverse strain and Poisson's ratio were measured in single rat tail tendon (RTT) fascicles during stress relaxation testing. Although previous studies have characterized the stress response during relaxation of fascicles [14, 15], this is the first study to characterize the lateral strain and Poisson's ratio during relaxation. For this study, rat tail tendon fascicles were chosen as they have been well characterized [16-20], are easy to obtain, have a large aspect ratio that is conducive to obtaining homogenous strains and have nearly cylindrical cross sections that aid in measuring transverse strain.

Methods

Rat tail tendons were obtained from a single, freshly sacrificed Sprague Dawley rat, placed in gauze, moistened using phosphate buffered saline and frozen for future testing. Prior to testing, tendons were allowed to thaw at room temperature and then single fascicles were removed from the tendons. A total of six samples were isolated from six different tendons and cut to a length of approximately 20 mm. Fascicle diameters were approximately 250 μm, providing an aspect ratio of 80:1. Samples were attached to a mini materials test machine using tissue clamps and tested in a PBS bath at room temperature. Prior to clamping, small black beads with a hole drilled in the center

were slid onto the tendon fascicle and glued 10 mm apart using cyanoacrylate gel. The beads were applied as markers to track axial strain. The samples tended to rotate during loading, which was noted in previous studies [19]. By stringing the fascicle through a bead, a marker was created that had a consistent profile in the presence of rotation. Images of the sample were acquired at a rate of 2.0 Hz (resolution =1024 x 1360 pixels) and saved for strain analysis. Force was recorded using a 10 N load cell and the displacements and image acquisition was controlled using Labview. A prestrain was applied to the samples using a 0.4 N tare load. Preliminary experiments demonstrated that this load was adequate to remove slack in the sample and to prevent excessive rotation during testing. Samples were preconditioned by applying 10 cycles of a triangular displacement profile to 3.0% strain at a strain rate of 0.5%/s. Samples were allowed to recover for 10 minutes after preconditioning [21]. Stress relaxation testing was then performed, with a maximum strain of 3%, a strain rate of 0.5 %/s and a relaxation time of 300 s.

The images from the ramping phase and stress relaxation were imported into Matlab where strain analysis was performed. Images were converted to black and white using a threshold value of 0.15, at which point the outline of the sample (defined as the tissue between the two bead markers) was segmented. A quadrilateral was fit to the segmented image using a global optimization routine, namely a pattern search algorithm in Matlab's optimization toolbox (Fig 5.1).

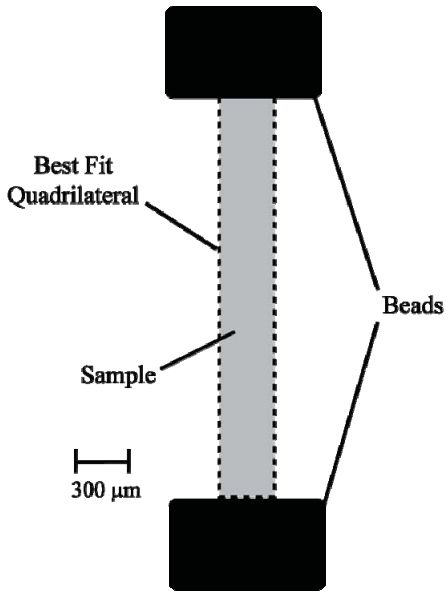

Figure 5.1: Sample schematic. A typical image used for calculating axial strain, transverse strains and Poisson's ratio. The sample, marker beads and the best fit quadrilateral are indicated.

The deformation gradient for each time point was computed from the nodes of the best fit quadrilateral:

$$F_{iJ} = \sum_{a=1}^{4} x_{a,i} \frac{\partial N_a}{\partial X_J} \tag{5.1}$$

where $\partial N_a/\partial X_J$ is the derivative of the a'th shape function with respect to the reference configuration and $x_{a,i}$ is the deformed nodal coordinates for the a'th node [22]. The deformation gradient was then used to compute the engineering strain in the fiber (e_f) and transverse (e_t) directions. The Poisson's ratio in the fiber plane was computed using $\upsilon = -e_t / e_f$. Analysis was only performed on strains larger than the transition strain (the point where the exponential region becomes linear), as most rotation had subsided by this point. The transition strain was found by performing a nonlinear curve fit to a piecewise exponential and linear function described previously [23]:

$$f(\lambda)=\begin{Bmatrix} 0 & \lambda \le 1 \\ c_1\left(e^{c_2(\lambda-1)}-1\right) & \lambda < \lambda^* \\ c_3\lambda + c_4 & \lambda \ge \lambda^* \end{Bmatrix} \tag{5.2}$$

where f is the force, λ is the fiber stretch, λ^* is the transition stretch and c_1-c_4 are constants. Strain analysis used the transition strain as the reference configuration (Fig 5.2). The mean value and standard deviation for all samples were computed for the force, axial strain, transverse strain and Poisson's ratio at all time points. A linear correlation was performed between the normalized force and normalized Poisson's' ratio using data points for all samples, where each data set was normalized relative to the maximum value obtained. To provide equal weight to points during stress relaxation, the data were resampled logarithmically.

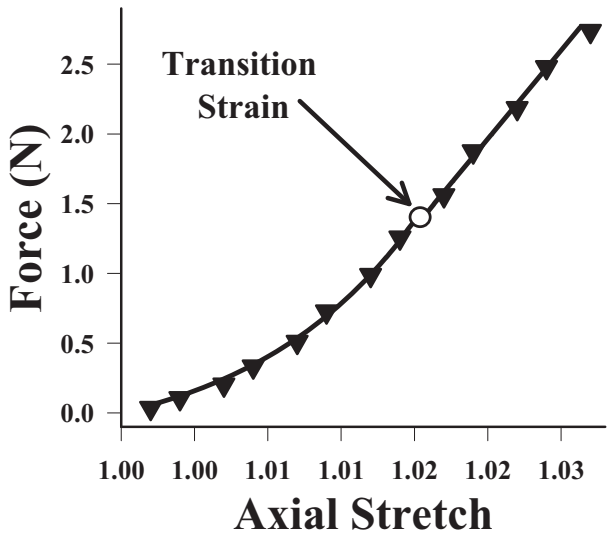

Figure 5.2: A typical force-strain curve during the ramping phase. Black triangles represent the data points, the solid line represents the nonlinear curve fit and an empty circle represents the transition strain.

Results

During relaxation the mean transverse strain was negative and decreased with time, while the mean Poisson's ratio was positive and increased with time (Fig 5.3 top, Fig 5.4 top). During the initial ramping phase the mean Poisson's ratio (averaged over all samples) was 0.70 ±0.52, and increased to a mean value of 4.26±1.53 at the end of testing. This behavior was qualitatively similar to the decrease in the force measured during relaxation (Fig 5.4 bottom). A plot of the normalized force vs. the normalized Poisson's ratio for all samples revealed a linear relationship (Fig 5.5, m = -1.05, R^2 = 0.85). The linear correlation was significant with a p value of $\alpha<0.0001$. The equilibrium volume ratio, as computed from the mean axial and transverse strains was 0.836±0.065, which corresponds to a mean volume loss of 16.4±6.5%. The optically measured axial tissue strain was constant in time and linearly correlated with the applied clamp strain by a value of 75% ± 12% (Fig 5.3 bottom).

Discussion

As hypothesized, there was a time dependent volumetric behavior in RTT during stress relaxation. This was manifested as a decreasing lateral strain and a corresponding increase in Poisson's ratio with time. The mean Poisson's ratios for all times were in excess of the isotropic limit of 0.5, which is indicative of volume loss during uniaxial tensile testing. The mean volume loss at the end of testing was 16.4%, signifying a time dependent fluid exudation. This is supported by previous studies which have experimentally observed fluid exudation during tensile loading [24-26]. The Poisson's ratio during the ramp phase was 0.70, which indicates nearly incompressible behavior during fast loading, as predicted by biphasic theory.

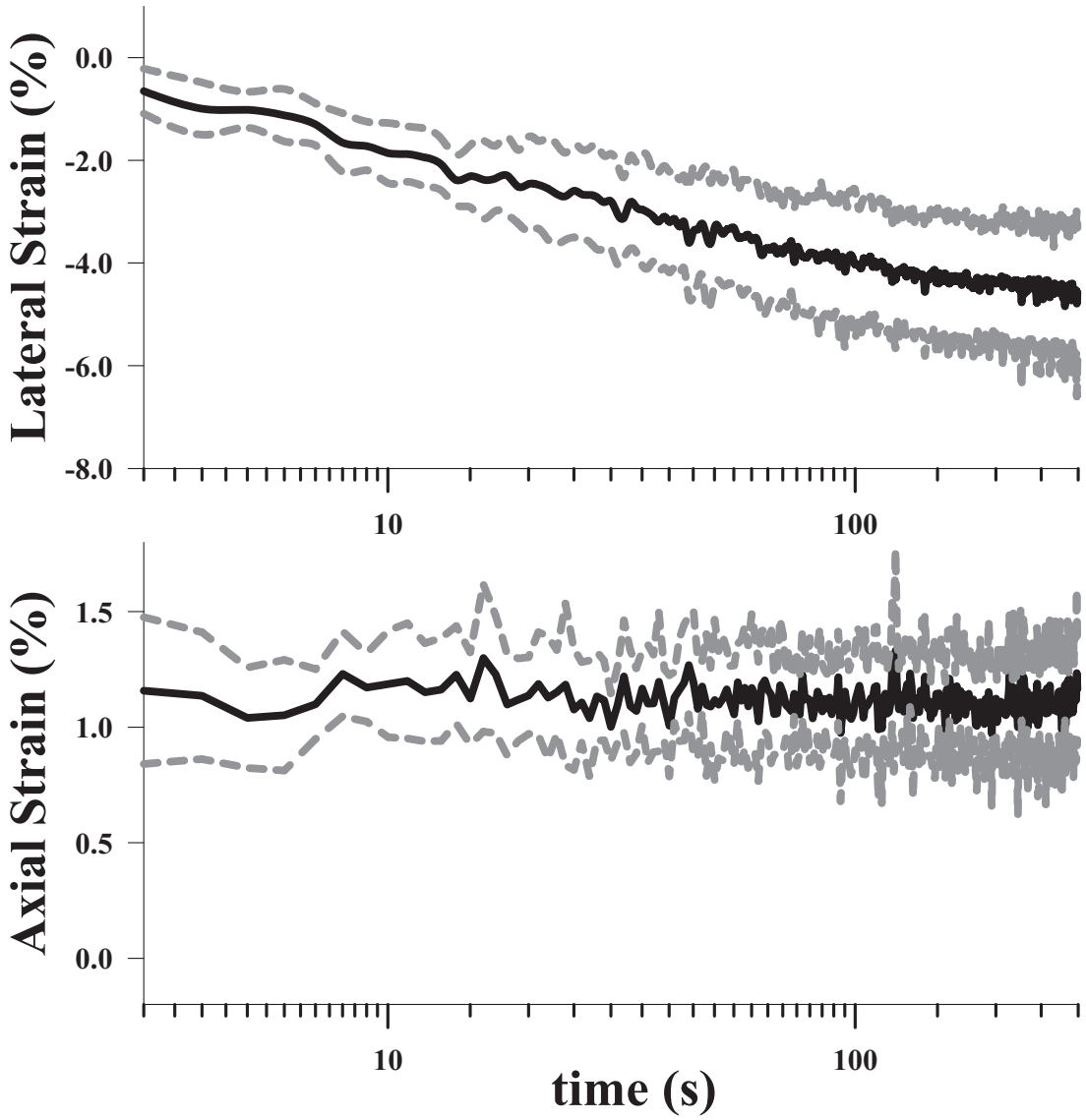

Figure 5.3: Lateral and axial strain vs. time. (Top) Transverse strain versus time (log scale) for all samples. (Bottom) Axial strain versus time (log scale) for all samples. A linear fit of the axial tissue strain resulted in a negligible slope, indicating that it was constant during relaxation. In both plots the solid line is the mean value (averaged over all samples) while the dashed line represents the standard deviation for each time point.

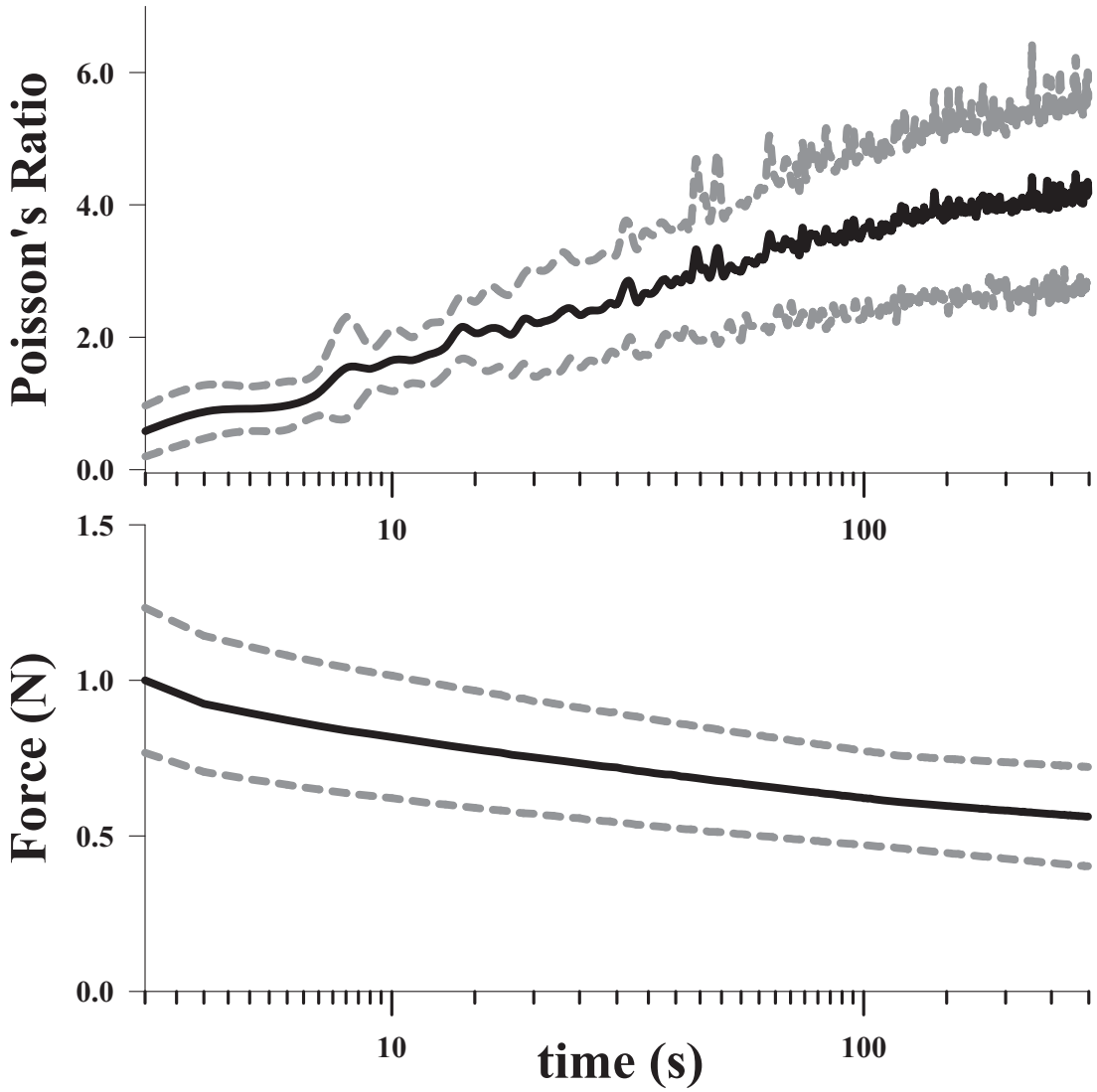

Figure 5.4: Poisson's ratio and force vs. time. **(**Top) Poisson's ratio vs. time (log scale) for all samples. (Bottom) Normalized force vs. time (log scale) for all samples. The solid line is the mean value (averaged over all samples) while the dashed line represents the standard deviation for each time point.

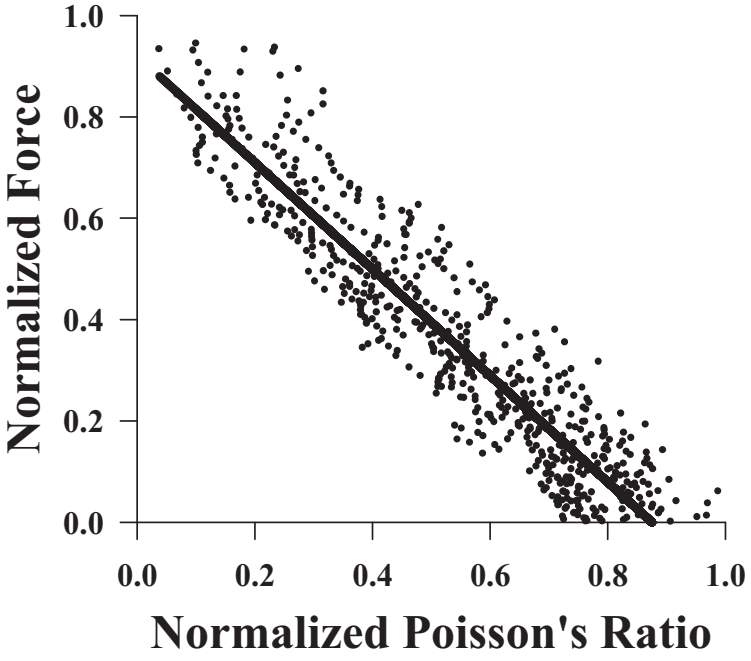

Figure 5.5: The normalized force plotted against the normalized Poisson's ratio for all data points. Note that the data were logarithmically sampled in time to provide an equal distribution of points throughout the entire data range. The best fit is represented by a solid black line.

The equilibrium Poisson's ratio was 4.26, indicating elastic behavior with a large volume loss. The correlation between the Poisson's ratio and force during relaxation revealed an intrinsic connection between volumetric behavior and stress during the relaxation processes. These results agree with predictions from biphasic theory and suggest some or all of the apparent viscoelastic response can be explained by fluid dependent mechanisms. This result is highly relevant, as fluid movement has been implicated in nutrient transport and mechanotransduction and may be fundamentally important in the behavior of fascicles in normal tissues [6, 9, 27, 28].

The results from this study are supported by previous biphasic fits of collagenous tissues reported in the literature. Transversely isotropic biphasic fits were performed on

incremental stress relaxation data of mouse tail fascicles and excellent fits were obtained [9]. The previous study predicted Poisson's ratio's ranging from 2.0 - 2.4, which compares favorably to the measured value of 4.26 in the current study. Large Poisson's ratios were also reported for sheep flexor tendon (v=2.98±2.59) [29], capsular ligament tissue (v=2.0 ±1.9) [30] and meniscus (v=2.13±1.27) [31], suggesting a large volumetric response is intrinsic to these tissues.

A significant rotation was present within the toe region of the ramping phase, as previously observed [19]. This suggests the presence of a helical organization within the fascicle. Micromechanical models of helical structures within tendon and ligament suggest the presence of helical twisting, which may be responsible for the large experimentally observed Poisson's ratios [32]. Further evidence for the presence of a helical organization is found in previous histological studies on tendon and ligament [33-36].

The primary limitation of this study is that the analysis was restricted to strains exceeding the transition strain. To perform strain analysis in the toe region, a more sophisticated approach to measuring transverse strain will be needed. More specifically, a method for reconstructing the 3D cross section of the fascicle will be required to compensate for the strain artifacts induced by fascicle rotation. It would have been desirable to fit biphasic models to the stress data and determine their capability to predict transverse strain. However, the use of a single step displacement combined with material nonlinearity made this infeasible. Incremental stress relaxation testing starting from the transition strain will be pursued in future studies.

Another limitation of this study was noise in the strain data (and thus Poisson's ratio) due to the resolution of the camera (~1 μm/pixel) and the size of the sample within the field of view. Given the typical width of the sample (~250 pixels), an error in the segmentation by a single pixel resulted in an error in the Poisson's ratio of ~0.3, which is comparable to the error seen in the data. The segmentation errors were a result of varying image quality, which was affected by convection currents in the PBS bath and slight movement of the sample (e.g., rotation) during relaxation.

With an understanding of how single fascicles behave, the question as to how this behavior translates to whole tissue behavior naturally arises. Given that experimental measurements of the Poisson's ratio in whole tissue preparations are also large, it can be assumed that adjacent fascicles are mechanically coupled in such a way as to generate a large macroscopic volumetric response. However, elucidating the mechanisms of fluid flux at the macroscopic level is an open question. It is possible (as suggested by Yin et al.) that the primary resistance to fluid flux occurs at the fascicle level and that resistance to fluid flow between fascicles and out of the tissue may be minimal. It is also possible that fluid cannot freely flow between fascicles, which would suggest the presence of flow dependent viscoelastic mechanisms at different structural levels. Measuring the volumetric response during stress relaxation of whole tissue preparations will be crucial to elucidating these mechanisms.

This study highlights an important connection between the axial stress and the Poisson's ratio during stress relaxation testing of RTT. This may provide evidence for the biphasic origins of tissue viscoelasticity and suggests that the time dependent axial stress behavior is intrinsically linked to the lateral relaxation of the tissue. However,

further work is needed to determine the relative contribution of solid and fluid phase contributions to the apparent viscoelastic behavior of single tendon fascicles. Curve fitting of poroviscoelastic models may be a useful means for elucidating these mechanisms and should be a focus of future research [37-41].

References

[1] Bonifasi-Lista, C., Lake, S. P., Small, M. S., and Weiss, J. A., 2005, "Viscoelastic Properties of the Human Medial Collateral Ligament under Longitudinal, Transverse and Shear Loading," J Orthop Res, 23(1), pp. 67-76.

[2] Woo, S. L., Debski, R. E., Zeminski, J., Abramowitch, S. D., Saw, S. S., and Fenwick, J. A., 2000, "Injury and Repair of Ligaments and Tendons," Annu Rev Biomed Eng, 2, pp. 83-118.

[3] Abramowitch, S. D., Clineff, T. D., Withrow, J. D., Papageorgiou, C. D., and Woo, S. L., 1999, "The Quasilinear Viscoelastic Properties of the Healing Goat Medial Collateral Ligament: An Experimental & Analytical Approach," 23rd Annual Meeting of the American Society of Biomechanics, Pittsburgh, Pennsylvania.

[4] Atkinson, T. S., Ewers, B. J., and Haut, R. C., 1999, "The Tensile and Stress Relaxation Responses of Human Patellar Tendon Varies with Specimen Cross-Sectional Area," J Biomech, 32(9), pp. 907-14.

[5] Atkinson, T. S., Haut, R. C., and Altiero, N. J., 1997, "A Poroelastic Model That Predicts Some Phenomenological Responses of Ligaments and Tendons," J Biomech Eng, 119, pp. 400.

[6] Butler, S. L., Kohles, S. S., Thielke, R. J., Chen, C., and Vanderby, R., Jr., 1997, "Interstitial Fluid Flow in Tendons or Ligaments: A Porous Medium Finite Element Simulation," Med Biol Eng Comput, 35(6), pp. 742-6.

[7] Weiss, J. A., and Gardiner, J. C., 2001, "Computational Modeling of Ligament Mechanics," Crit Rev Biomed Eng, 29(3), pp. 303-71.

[8] Yamamoto, E., Hayashi, K., and Yamamoto, N., 1999, "Mechanical Properties of Collagen Fascicles from the Rabbit Patellar Tendon," J Biomech Eng, 121(1), pp. 124-31.

[9] Yin, L., and Elliott, D. M., 2004, "A Biphasic and Transversely Isotropic Mechanical Model for Tendon: Application to Mouse Tail Fascicles in Uniaxial Tension," J Biomech, 37(6), pp. 907-16.

[10] Miyazaki, H., and Kozaburo, H., 1999, "Tensile Tests of Collagen Fibers Obtained from the Rabbit Patellar Tendon," Biomedical Microdevices, 2(2), pp. 151-157.

[11] Svensson, R. B., Hassenkam, T., Hansen, P., and Peter Magnusson, S., "Viscoelastic Behavior of Discrete Human Collagen Fibrils," J Mech Behav Biomed Mater, 3(1), pp. 112-5.

[12] Armstrong, C. G., Lai, W. M., and Mow, V. C., 1984, "An Analysis of the Unconfined Compression of Articular Cartilage," J Biomech Eng, 106(2), pp. 165-73.

[13] Cohen, B., Lai, W. M., and Mow, V. C., 1998, "A Transversely Isotropic Biphasic Model for Unconfined Compression of Growth Plate and Chondroepiphysis," J Biomech Eng, 120(4), pp. 491-6.

[14] Elliott, D. M., Robinson, P. S., Gimbel, J. A., Sarver, J. J., Abboud, J. A., Iozzo, R. V., and Soslowsky, L. J., 2003, "Effect of Altered Matrix Proteins on Quasilinear Viscoelastic Properties in Transgenic Mouse Tail Tendons," Ann Biomed Eng, 31(5), pp. 599-605.

[15] Gupta, H. S., Seto, J., Krauss, S., Boesecke, P., and Screen, H. R., "In Situ Multi-Level Analysis of Viscoelastic Deformation Mechanisms in Tendon Collagen," J Struct Biol, 169(2), pp. 183-91.

[16] Diamant, J., Keller, A., Baer, E., Litt, M., and Arridge, R. G., 1972, "Collagen; Ultrastructure and Its Relation to Mechanical Properties as a Function of Ageing," Proc R Soc Lond B Biol Sci, 180(60), pp. 293-315.

[17] Kastelic, J., Galeski, A., and Baer, E., 1978, "The Multicomposite Structure of Tendon," Connect Tissue Res, 6(1), pp. 11-23.

[18] Rigby, B. J., Hirai, N., Spikes, J. D., and Eyring, H., 1959, "The Mechanical Properties of Rat Tail Tendon," J Gen Physiol, 43(2), pp. 265-283.

[19] Screen, H. R. C., Bader, D. L., Lee, D. A., and Shelton, J. C., 2004, "Local Strain Measurement within Tendon," Strain, 40(4), pp. 157-163.

[20] Screen, H. R. C., and Cheng, V. W. T., 2007, "The Micro-Structural Strain Response of Tendon," Journal of Material Science, 19, pp. 1-2.

[21] Lujan, T. J., Underwood, C. J., Jacobs, N. T., and Weiss, J. A., 2009, "Contribution of Glycosaminoglycans to Viscoelastic Tensile Behavior of Human Ligament," J Appl Physiol, 106(2), pp. 423-31.

[22] Bonet, J., and Wood, R., 1997, *Nonlinear Continuum Mechanics for Finite Element Analysis*, Cambridge University Press, Cambridge, England.

[23] Weiss, J. A., 1994, "A Constitutive Model and Finite Element Representation for Transversely Isotropic Soft Tissues," Ph.D. thesis, University of Utah, Salt Lake City.

[24] Wellen, J., Helmer, K. G., Grigg, P., and Sotak, C. H., 2004, "Application of Porous-Media Theory to the Investigation of Water Adc Changes in Rabbit Achilles Tendon Caused by Tensile Loading," J Magn Reson, 170(1), pp. 49-55.

[25] Helmer, K. G., Nair, G., Cannella, M., and Grigg, P., 2006, "Water Movement in Tendon in Response to a Repeated Static Tensile Load Using One-Dimensional Magnetic Resonance Imaging," J Biomech Eng, 128(5), pp. 733-41.

[26] Hannafin, J. A., and Arnoczky, S. P., 1994, "Effect of Cyclic and Static Tensile Loading on Water Content and Solute Diffusion in Canine Flexor Tendons: An in Vitro Study," Journal of Orthopaedic Research, 12, pp. 350-356.

[27] Lavagnino, M., Arnoczky, S. P., Kepich, E., Caballero, O., and Haut, R. C., 2008, "A Finite Element Model Predicts the Mechanotransduction Response of Tendon Cells to Cyclic Tensile Loading," Biomech Model Mechanobiol, 7(5), pp. 405-16.

[28] Albro, M. B., Chahine, N. O., Li, R., Yeager, K., Hung, C. T., and Ateshian, G. A., 2008, "Dynamic Loading of Deformable Porous Media Can Induce Active Solute Transport," J Biomech, 41(15), pp. 3152-3157.

[29] Lynch, H. A., Johannessen, W., Wu, J. P., Jawa, A., and Elliott, D. M., 2003, "Effect of Fiber Orientation and Strain Rate on the Nonlinear Uniaxial Tensile Material Properties of Tendon," J Biomech Eng, 125(5), pp. 726-31.

[30] Hewitt, J., Guilak, F., Glisson, R., and Vail, T. P., 2001, "Regional Material Properties of the Human Hip Joint Capsule Ligaments," J Orthop Res, 19(3), pp. 359-64.

[31] Leroux, M. A., and Setton, L. A., 2002, "Experimental and Biphasic Fem Determinations of the Material Properties and Hydraulic Permeability of the Meniscus in Tension," J Biomech Eng, 124(3), pp. 315-21.

[32] Reese, S. P., Maas, S. A., and Weiss, J. A., 2010, "Micromechanical Models of Helical Superstructures in Ligament and Tendon Fibers Predict Large Poisson's Ratios," J Biomech, 43(7), pp. 1394-400.

[33] Yahia, L. H., and Drouin, G., 1989, "Microscopical Investigation of Canine Anterior Cruciate Ligament and Patellar Tendon: Collagen Fascicle Morphology and Architecture," J Orthop Res, 7(2), pp. 243-51.

[34] Vidal, D. C., 2003, "Image Analysis of Tendon Helical Superstructure Using Interference and Polarized Light Microscopy," Micron, 34(8), pp. 423-432.

[35] Vidal Bde, C., and Mello, M. L., 2009, "Structural Organization of Collagen Fibers in Chordae Tendineae as Assessed by Optical Anisotropic Properties and Fast Fourier Transform," J Struct Biol, 167(2), pp. 166-75.

[36] Vidal Bde, C., 1995, "Crimp as Part of a Helical Structure," C R Acad Sci III, 318(2), pp. 173-8.

[37] Disilvestro, M. R., and Suh, J. K., 2001, "A Cross-Validation of the Biphasic Poroviscoelastic Model of Articular Cartilage in Unconfined Compression, Indentation, and Confined Compression," J Biomech, 34(4), pp. 519-25.

[38] Disilvestro, M. R., Zhu, Q., and Suh, J. K., 2001, "Biphasic Poroviscoelastic Simulation of the Unconfined Compression of Articular Cartilage: Ii--Effect of Variable Strain Rates," J Biomech Eng, 123(2), pp. 198-200.

[39] Huang, C. Y., Mow, V. C., and Ateshian, G. A., 2001, "The Role of Flow-Independent Viscoelasticity in the Biphasic Tensile and Compressive Responses of Articular Cartilage," J Biomech Eng, 123(5), pp. 410-7.

[40] Huang, C. Y., Soltz, M. A., Kopacz, M., Mow, V. C., and Ateshian, G. A., 2003, "Experimental Verification of the Roles of Intrinsic Matrix Viscoelasticity and Tension-Compression Nonlinearity in the Biphasic Response of Cartilage," J Biomech Eng, 125(1), pp. 84-93.

[41] Mak, A. F., 1986, "Unconfined Compression of Hydrated Viscoelastic Tissues: A Biphasic Poroviscoelastic Analysis," Biorheology, 23(4), pp. 371-83.

CHAPTER 6

MICROMECHANICAL MODEL OF A COLLAGEN BASED TENDON SURROGATE: DEVELOPMENT, VALIDATION AND ANALYSIS OF MESOSCALE SIZE EFFECTS

Abstract

Tendons and ligaments are fibrous bands of connective tissue that are primarily composed of water (~70%) and type I collagen. Collagen is hierarchically organized into nanoscale fibrils, microscale fibers and mesoscale fascicles. Force transfer across scales is complex and poorly understood, with the macroscale strain not being representative of the microscale strain. Since innervation, the vasculature, damage mechanisms and mechanotransduction occur at the microscale, understanding such multiscale interactions is of high importance. Unfortunately, experimental characterization of this behavior has proved challenging. In this study, a physical model was used in combination with a computational model to isolate and study the mechanisms of force transfer between scales. A collagen based tendon surrogate was used as the physical model. The surrogate consisted of extruded collagen fibers embedded within a collagen gel matrix, which emulated the organization of fascicles within a tendon. A micromechanical finite element model of the surrogate was validated using tensile test data that were recorded using a custom tensile testing device mounted on a confocal microscope. The

experimentally measured macroscale strain was not representative of the microscale strain, which was highly inhomogeneous. As with native tendon tissue, the microstructures in the surrogate were not infinitesimally small in relation to the macroscale, which violates the assumption of a continuum. The micromechanical model, in combination with a macroscopic continuum model, revealed that the microscale inhomogeneity resulted from size effects in the presence of a constrained boundary. A sensitivity study indicated that significant scale effects would be present over a range of physiologically relevant interfiber spacing values and matrix material properties. The results of this study indicate that the continuum assumption may not accurately represent the mechanisms of force transfer between scale levels, thus necessitating the use of alternative modeling techniques.

Introduction

Tendons and ligaments are fibrous connective tissues that transmit loads within the musculoskeletal system. Acute and chronic injury of tendons and ligaments is among the most common injuries in the musculoskeletal system [1-3]. Despite decades of research, the treatment of common injuries such as ligament ruptures and tendinitis remains challenging [3]. These difficulties are due, at least in part, to our incomplete understanding of the microstructural interactions that underlie tissue behavior. Tendons and ligaments are composites with macroscopic mechanical properties that are derived from a complex, multiscale organization of collagen and other ECM proteins. At the nanoscale, tropocollagen is excreted by fibroblasts and self assembles into collagen fibrils (d~100 nm). At the microscale, fibrils assemble into fibers (d~20 um), to which fibroblasts attach. At the mesoscale, fibers further organize into fascicles (d~200 um),

which then assemble into the macroscale tendon or ligament unit (d~10 mm) [4]. At each level of hierarchy, collagen structures are aligned in a predominantly parallel fashion. Separating adjacent fibers and fascicles is a thin fascia (referred to as endotenon) which consists primarily of randomly oriented collagen fibrils [4-6].

Force transfer between scales is complex and poorly understood. At the mesoscopic level, force does not appear to be distributed evenly between fascicles [7, 8]. At the fiber level, the strain is highly inhomogeneous, with the dominant modes of deformation consisting of fiber sliding and uncrimping [9, 10]. An understanding of these multiscale interactions is of fundamental importance to the understanding of normal tissue function and dysfunction. In tendons, failure occurs at the fiber and fascicle level [11-13]. Because adjacent fascicles are poorly coupled, this is hypothesized to lead to stress shielding of damaged fascicles, which may affect healing [7]. Furthermore, tendon vascularization and innervation, which is required for normal function of tendon and ligament, occurs at the fascicle level. Since mechanotransduction occurs at the fiber level, abnormal fiber loading (e.g., in response to fascicle injury or rupture) may adversely affect the fibroblast mediated remodeling of the tissue [7, 14]. At the fibril level, certain disease states (e.g., Ehlers Danlos Syndrome) affect the formation and subsequent strength of collagen fibrils [15]. A comprehensive understanding of the mechanical function of normal and diseased tendon can only exist in a context that takes all scale levels and their interactions into consideration.

Although it is clear that multiscale structure-function relationships are of fundamental importance, the study of these aspects has proved challenging. Multiple studies have tested tendon constituents (e.g., single fascicles, fibers and fibrils) in an

attempt to isolate scale dependent behaviors. However, these studies have arrived at conflicting conclusions. Some studies have found that tissue structures become stiffer with increasing scale level (e.g., whole tendon is stiffer than fascicles) [16-18] while others have reported the opposite [7, 8]. These conflicting results may be attributable to damage of tissue structures during separation, clamping artifacts, errors in strain measurement, errors in cross sectional area estimates and sample hydration. Obtaining a homogenous test sample is another obstacle, as material properties within a tendon and ligament varying between the insertion site and the midsubstance [19]. All of these aspects introduce uncontrolled variables that can be difficult to account for. A potential confounding factor that is often overlooked is the possibility of microscale size effects, which are introduced by inadequate scale separation. The characteristic size of fascicles (~200 um) and fibers (~20 um) are only 1-3 orders of magnitude smaller than macroscopic tendon dimensions (~10 mm) [4, 20]. This violates the continuum assumption that microstructures are infinitesimally small relative to the macroscale. In the presence of a constrained boundary (e.g., an insertion site or tissue clamp), size effects may propagate throughout the tissue in a manner inconsistent with continuum theories [21, 22].

The present study addresses these challenges by using a surrogate material as a physical model to isolate and study key structural features. A validated micromechanical finite element model is also created. This allows certain hypotheses to be addressed that would be difficult to test using the physical model alone. The surrogate consists of dense, extruded collagen fibers aligned within a collagen gel interfiber matrix. The fibril organization, diameter and linear modulus of the extruded fibers is similar to that of

fascicles, while the fibril organization and linear modulus of the gel matrix is similar to that of the interfascicle endotenon matrix. This emulates the mesoscale structure of tendon and ligament. A physical model reduces the number of uncontrolled variables related to structural organization. The surrogate dimensions and fiber organization can be controlled, and the material properties of the constituents can be controlled by modulating the density of collagen used in the matrix and fibers. In the present study, surrogates are subjected to uniaxial tensile testing in which a single independent variable (the longitudinally applied strain) is applied to the system and multiple dependent variables are measured. The experimental measures include the macroscopic stress and 2D strain as well as the microscale 2D strain. The 2D strain measurement is performed by simultaneously measuring the longitudinally applied strain and the transverse strain induced by the Poisson's effect. Poisson's ratios are computed from the 2D macroscopic and microscopic strain data. The use of these data provides a robust validation of the computational model.

The surrogate microstructure is not infinitesimally small in comparison to the microscale. Thus, it was hypothesized that boundary effects and size effects will not be negligible. To test this hypothesis, two approaches are taken. First, the aspect ratio of the micromechanical surrogate model is varied. This reveals the extent to which boundary effects propagate into the surrogate mid substance. Second, a continuum model of the surrogate is created and the aspect ratio of this model is also varied. This determines if these effects originate solely from the constrained boundary, or from size effects in the presence of a constrained boundary. This addresses the important question as to whether the surrogate behavior can be approximated using the continuum

assumption. A sensitivity study is then performed in which the interfiber spacing and the interfiber matrix material properties are varied. The parameters within the sensitivity study span physiologically relevant values, allowing the model observations to be extended to the study of native tendon tissue.

In the present study, four objectives are addressed: (1) Develop a collagen based tendon surrogate for use as a physical model and subject it to tensile loading. (2) Create a 3D micromechanical finite element (FE) model of the surrogate and validate it using stress and strain measured at both the macroscale and microscale. (3) Examine boundary and size effects within the surrogate using the validated micromechanical model and a continuum model. (4) Perform a sensitivity study using a range of physiologically relevant values.

Methods

Surrogate construction

Collagen based surrogates were created from type I collagen. Type I collagen was extracted from rat tail tendon following previous protocols and solubilized in acetic acid at 10 mg/ml [23, 24]. To create extruded collagen fibers, collagen was diluted to 5 mg/ml in 1X PBS, neutralized to a pH=8.5, injected into 1 m silicone tubes with an inner diameter of 1.4 mm and allowed to polymerize at RT for 8 hours. Sulfide functionalized fluorescent styrene beads (d=1.0 μm, $\lambda_{emission}$=543 nm, $7.3 \cdot 10^6$ beads/ml) were added to the solution prior to polymerization [25]. The gel was extruded from the silicone tubes to form fibers. The fibers were incubated in water overnight and then allowed to dry under their own weight to a final diameter of ~100 μm [23, 24]. A custom jig was constructed to align the fibers with a constant spacing. The jig consisted of silicone inserts with laser-

cut channels (500 μm spacing) to align the fibers. These inserts were placed between two glass slides (slide spacing=1mm) contained within an acrylic chamber, thus forming a mold. Fibers were placed in the jig and 5 mg/ml collagen containing carboxyl functionalized fluorescent styrene beads (1 μm diameter, $\lambda_{emission}$=605 nm, $7.3 \cdot 10^6$ beads/ml) was injected into the chamber and allowed to polymerize overnight. After polymerization, the constructs were cross linked in a solution of 5% formalin and 2% gluteraldehyde for 8 hours. Constructs were then cut to dimensions of ~2.5 mm in width and 30 mm in length and stored in water at 4°C. The final constructs consisted of evenly spaced fibers aligned in parallel and centered within the gel matrix (Fig 6.1 A). Individual fibers and gel samples (2 mg/ml) were fixed and stained using osmium tetroxide, dehydrated in a graded ethanol series, air dried, sputter coated and imaged using SEM following previously reported protocols [26].

Surrogate testing

A custom mechanical testing apparatus was created to allow simultaneous measurement of force, macroscopic strain and microscopic strain (Fig 6.2 A). The apparatus was mounted on the stage of an inverted confocal microscope. Surrogates were immersed in a water bath (N=9) at room temperature (RT), mounted in the clamps and subjected to incremental stress relaxation testing to determine the quasistatic elastic response [27]. A total of six 1% strain increments (6% max strain) were applied at a strain rate of 1%/sec, with a relaxation time of 5 min between increments.

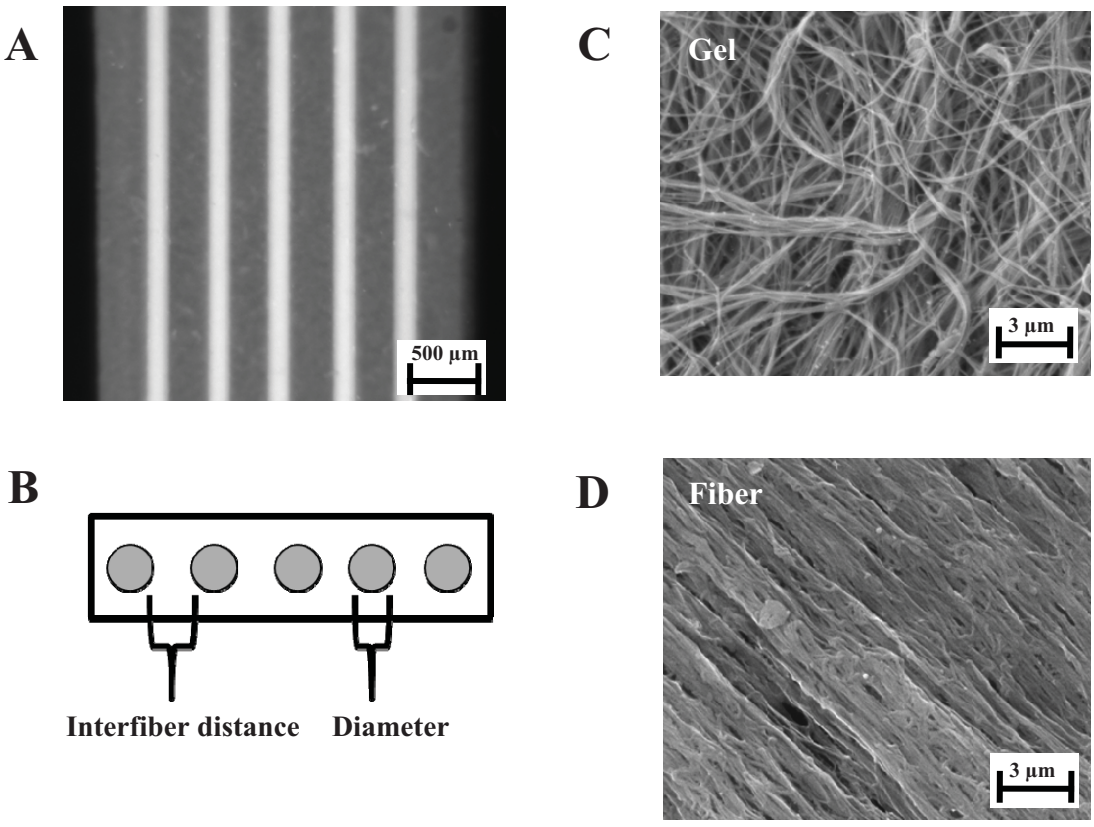

Figure 6.1: Surrogate structure. (A) An overhead view of a physical surrogate shows the extruded collagen fibers embedded within the collagen gel. (B) The collagen fibers (d=185 µm) were regularly spaced (spacing=300 µm) within the gel. (C and D) SEM imaging reveals that the gel had loosely and randomly packed collagen fibrils, while the fiber had densely packed and highly aligned fibrils.

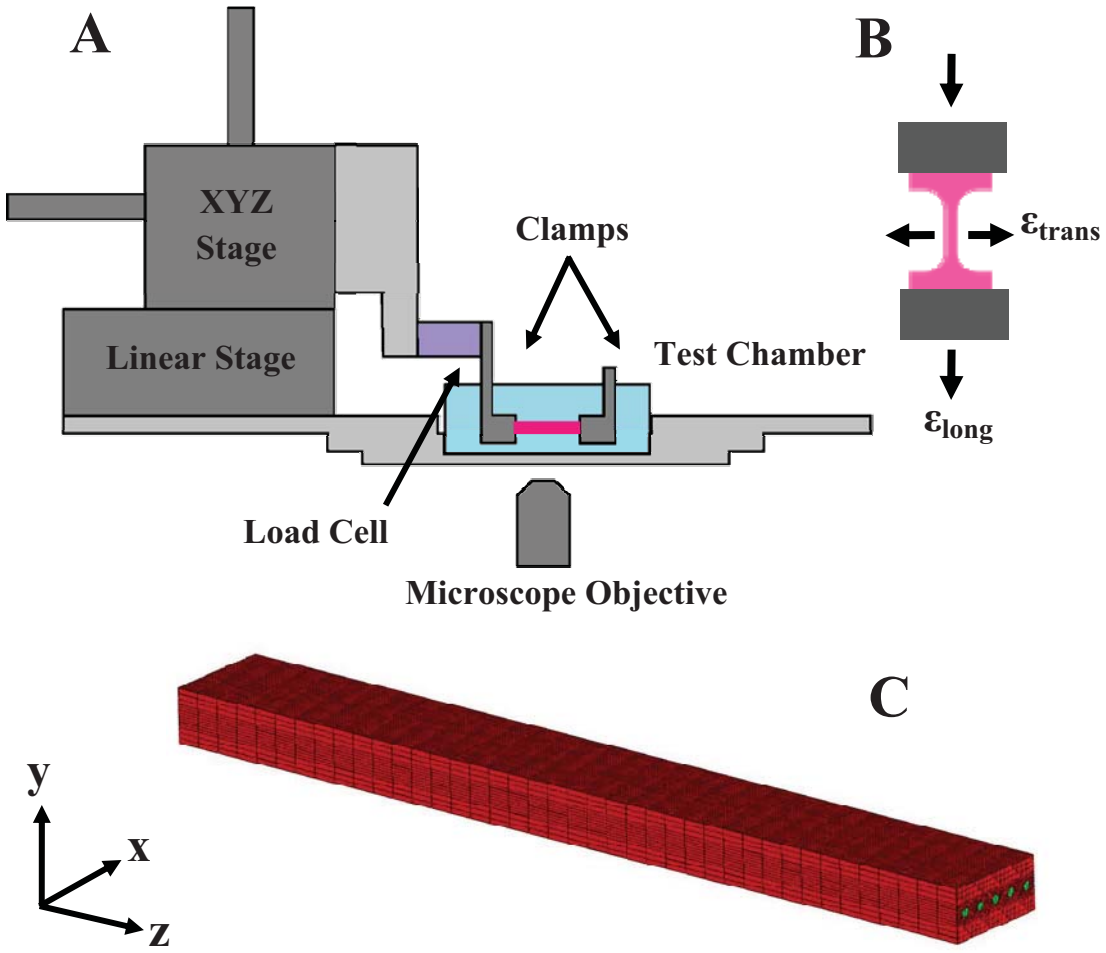

Figure 6.2: Mechanical testing and FE mesh. (A) A custom test apparatus was mounted onto an inverted confocal microscope. The linear stage and load cell were interfaced to a PC via Labview. The sample was tested in a water chamber and images were acquired using confocal fluorescence imaging. (B) Collagen gels were molded into dog bone shaped specimens for uniaxial tensile testing where the 2D strain (the longitudinal strain and transverse strain) as well as the stress was measured. (C) A micromechanical FE model of the surrogate was constructed, where green elements represent the fibers and red elements represent the gel matrix.

After equilibration of each strain increment, force was recorded and a confocal z-stack was acquired from the center plane of the construct at 4X magnification and 10X magnification using two lasers to excite the red ($\lambda_{exitation}$=543 nm) and green ($\lambda_{exitation}$=488 nm) fluorescent beads. A z-stack with a total of five images was acquired with a 40 μm spacing for each strain level and magnification.

Strain measurement

The texture correlation technique was used to measure strain at the macroscale and microscale [28, 29]. For each z-stack, the image that was closest to the center of the construct was used for strain measurement (the dotted line in Fig 6.3 C). For the macroscale strain measurement, a quadrilateral was defined by four nodes within the 4X image (nodes denoted by a white "x" in Fig 6.3 A). At each node, a subregion of the image was extracted and used as a template. In the next image (acquired at the subsequent strain level), the templates were registered and the nodal displacements were computed using the template displacements. The nodal displacements for the quadrilateral were then used to find the deformation gradient between each strain level using the finite element method of shape function interpolations [30]:

$$dF_{iJ} = \sum_{a=1}^{4} x_{a,i} \frac{\partial N_a}{\partial X_J} \tag{6.1}$$

where dF_{iJ} is the deformation gradient computed from a sequence of two images, $\partial N_a/\partial X_J$ is the derivative of the a'th shape function with respect to the reference configuration and $x_{a,i}$ is the deformed nodal coordinates for the a'th node.

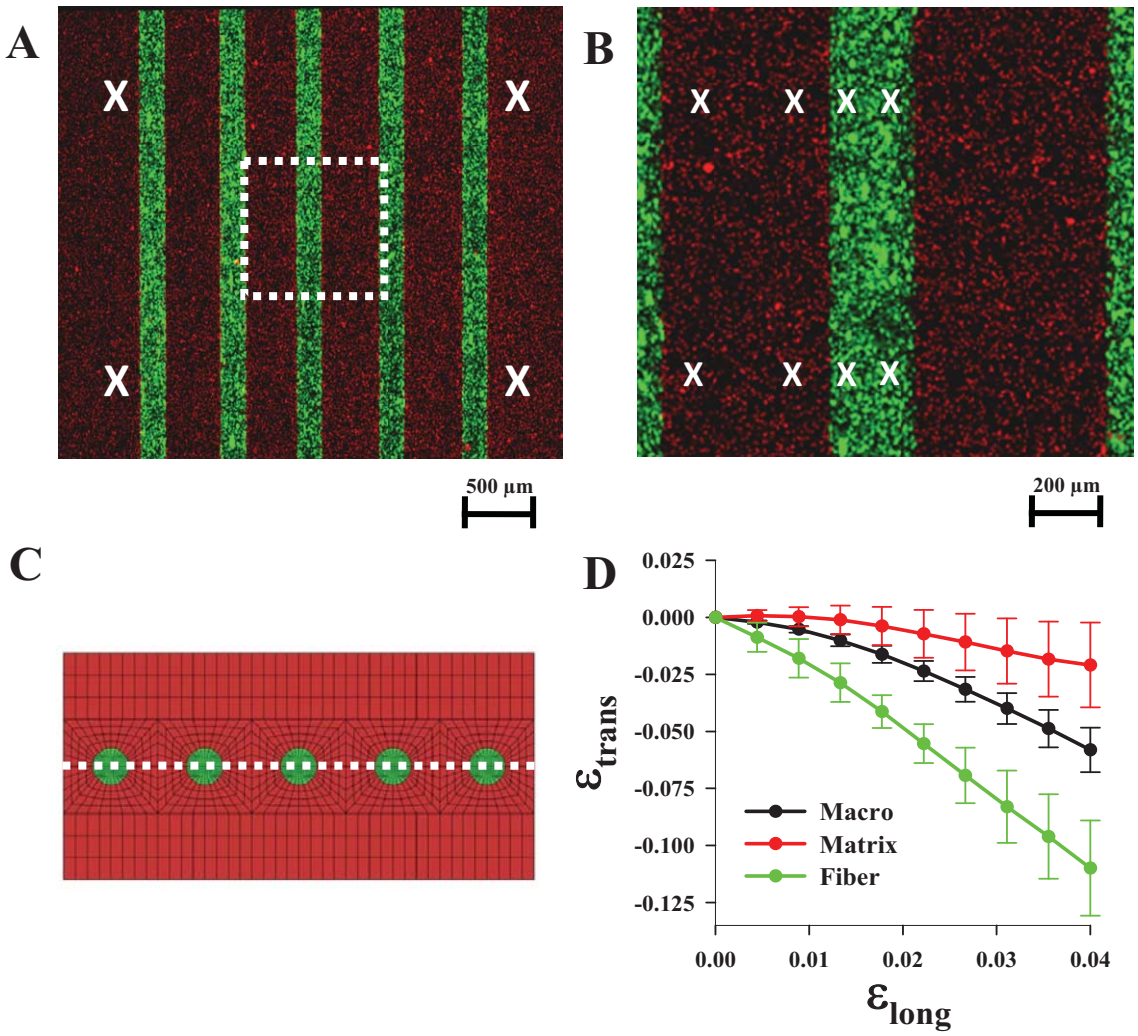

Figure 6.3: Confocal imaging results. (A) A dual channel 4X image shows the red fluorescent beads in the gel matrix and the green fluorescent beads in the fiber. The nodal locations for the macroscopic strain measurement are marked with a white "x". (B) A 10X image was taken from the center of the surrogate (indicated by the dotted white box in panel A) and used for computing the microscale fiber and gel strain. The locations of nodes for the microscale strain analysis are again marked with a white "x". (C) Confocal images were acquired from the center of the construct, as illustrated by the dotted line in a cross sectional view of the FE mesh. (D) The macroscopic transverse strain (black line) was not representative of the microscopic fiber strain (green line) or matrix strain (red line). The error bars represent the standard deviation computed for all samples.

The total deformation gradient for strain level *N* is computed by multiplying the deformation gradients from all previous strain levels:

$$F_N = \prod_{i=1}^{N} dF_i \tag{6.2}$$

The engineering strain was then computed from the deformation gradient:

$$\boldsymbol{\varepsilon} = \frac{1}{2}\left[\left(\mathbf{F} - \mathbf{I}\right) + \left(\mathbf{F} - \mathbf{I}\right)^T \right] \tag{6.3}$$

where $\boldsymbol{\varepsilon}$ is the 2nd order infinitesimal strain tensor. This yielded the average strain within the quadrilateral. This formulation was adopted because it only required that a unique template image be present in two consecutive image frames, which was necessary to accommodate the large rigid body displacements that resulted from the applied strain.

To obtain the microscale strain, a quadrilateral was defined for the matrix material and the fiber material (Fig 6.3 B). As with the macroscopic strain, template images were used to compute the deformation gradient and engineering strain, yielding strain values averaged over the quadrilateral regions. In general, the measured longitudinal strain was less than the applied clamp strain (e.g., 4%-5% optical strain for 6% clamp strain). The longitudinal strain, transverse strain and force were interpolated in time via cubic splines. The average strain across all samples was computed at ten times, using 4% as the maximum longitudinal strain, as all experimentally measured longitudinal strains exceeded that value. Average Poisson's ratios were computed for each region by performing a linear curve fit to the longitudinal strain (ε_{trans}) vs. transverse strain (ε_{long}) curves:

$$\varepsilon_{trans} = -v\varepsilon_{trans} + b \tag{6.4}$$

The negative of the slope of this line was taken to be the average Poisson's ratio (ν).

Gel and fiber testing and constitutive model

A hyperelastic constitutive model with a 3D elliptical fiber distribution (EFD) embedded within a matrix material was chosen to represent the nanoscale fibril behavior for the extruded fibers and the gel matrix [31]. To obtain coefficients for the constitutive model, collagen gels (5 mg/ml) and extruded fibers were tested in tension using the same protocol used for testing the surrogates. For gel tensile testing, collagen was polymerized into dog bone shaped tensile specimens (N=12, gauge length=20 mm, width=thickness=2.5 mm, Fig 6.2 B) [32]. To facilitate clamping, 2 mm thick sections of melamine foam were polymerized into the tabs of the dog bone specimens. For fiber testing, fibers were teased out of assembled, polymerized and fixed surrogates and cut to 40 mm (N=15). Both gels and fibers were subjected to incremental stress relaxation testing with the same strain rate and relaxation time as for the physical surrogate. As with the surrogate, beads were polymerized in the gel and fibers for strain tracking. Strain was measured using the texture correlation technique. Uniaxial stress-strain data and 2D strain data (ε_{trans}, ε_{long}) were obtained for both the gels and fibers. A nonlinear constrained optimization algorithm (the patternsearch function in Matlab's global optimization toolbox) was used to find the set of coefficients that minimized the sum of the square difference between the data and curve fits for the gel and fiber data sets, with the stress-strain and 2D strain data being fit simultaneously. In the curve fitting, gels were assumed to be isotropic. Based on SEM imaging and FFT analysis of the fibril

distribution within the extruded fibers [33], fibril distribution coefficients in the axial direction were set four times larger than the transverse direction (see "Gel and fiber constitutive model curve fitting" in Appendix B).

Micromechanical FE model

A hexahedral finite element mesh was constructed to represent the surrogate (Truegrid, XYZ Scientific, Inc.) using the average geometry (Fig 6.2 C). A mesh convergence study revealed that the mesh used resulted in a mean axial stress value that changed by less than 7% and a Poisson's ratio that changed by less than 1%, as compared to more refined models. The EFD model and the best fit coefficients from the gel and fiber testing were used. The surrogate tensile test was simulated by constraining one end of the model in the x-y-z directions and constraining the other end in the x-y plane (the transverse plane). The end constrained in the x-y plane was subjected to displacement boundary conditions in the longitudinal (z) direction that resulted in a clamp to clamp strain of 4%. The FEBio finite element software was used for all simulations (http://mrl.sci.utah.edu/software/febio). The macroscopic and microscopic strain was calculated from the FE model using the same nodal point coordinates that were used in the experimental texture correlation measurements. This allowed a direct comparison between the model and experimental results. To determine the effect of constitutive model parameters, simulations were performed using coefficient values that were ± one standard deviation. The best fit coefficient model was compared to the experimental results, with the normalized root mean square error values (NRMSE) being used as a metric of model and experimental agreement.

Model sensitivity to aspect ratio

To explore boundary effects, micromechanical models were created that had aspect ratios (AR) of 4:1, 8:1, 16:1, 24:1, 40:1 and 80:1. These models were given the same material properties, subjected to the same boundary conditions and strain analysis as described previously. To simulate a surrogate with an infinite aspect ratio, a simulation of unconstrained uniaxial tension was performed. The unconstrained model had the same geometry as previously described. However, boundary conditions were such that the ends of the surrogate were no longer fixed in the x-y plane. Briefly, nodes in the center x-y plane were constrained in the z direction, nodes in the center x-z plane were constrained in the y direction and the nodes in the center y-z plane were constrained in the x direction. The ends of the model were then subjected to opposing longitudinal displacement that corresponded to a 4% clamp strain. To assess homogeneity in the strain field, the microscale transverse strains at the model center in the x-z plane were extracted for both the constrained model (AR=20:1) and the unconstrained model, with the coefficient of variation being computed for each model.

Continuum model

To model a continuum response, the macroscopic stress and the macroscopic 2D strain were curve fit to the EFD model using the same procedure as described for the fibers and gel. The curve fit coefficients from the macroscopic data were then substituted for the fiber and matrix materials in the aforementioned micromechanical models with varying aspect ratio. These models were subjected to the same boundary conditions and strain analysis as the micromechanical models. If the continuum assumption is valid for

the surrogates, then continuum models should produce similar results to those obtained for the micromechanical models for all aspect ratios.

Sensitivity studies

To explore the model sensitivity to the interfiber spacing, models with an aspect ratio of 10:1 (a typical aspect ratio for a tendon or ligament) were created with a constant fiber diameter (d=185 μm) and a varied interfiber spacing (10, 20, 60, 160, 300 μm). To explore the model sensitivity to the material properties of the interfiber gel matrix, the stiffness of the gel for the 10 μm spacing model was scaled by a factor of 1-500 while the fiber stiffness was held constant. This provided a ratio of fiber stiffness to gel stiffness (E_{fiber}/E_{matrix}) ranging from 8-2500. These models were subjected to the same boundary conditions and strain analysis as described previously. The metric of comparison for the sensitivity studies was the difference between the microscale transverse fiber strain and the microscale transverse matrix strain:

$$\Delta\varepsilon_{micro} = Matrix\ \varepsilon_{trans} - Fiber\ \varepsilon_{fiber} \tag{6.5}$$

This was used to provide a more intuitive measure of the inhomogeneity within the microscale strain field.

Results

Physical surrogate and confocal imaging

Collagen based physical surrogates were created (N=9) that featured dense, extruded fibers (~30% by weight) embedded within a collagen hydrogel (0.5% by weight) (Fig 6.1). The resulting construct (l=30 mm, w=2.42 ±.14, t=1.16±0.07 mm) had

a mean fiber diameter of 185±20 μm and an interfiber spacing of 298±47 μm. SEM imaging revealed that the extruded fibers were composed of densely packed and aligned collagen fibrils, while the matrix was composed of loosely packed and randomly oriented fibrils (Fig 6.1 C,D). Functionalized styrene beads that were embedded in the gel (red emission) and fiber (green emission) were highly visible at 4X and 10X magnification and proved suitable for use in strain measurement. Image stacks were obtained from the plane intersecting the fibers (Fig 6.3 C), with both the fibers and matrix being clearly visible.

Macroscopic and microscopic strains

Two-dimensional strain was measured at the macroscale and the microscale. The macroscopic strain was not representative of the microscopic strain. At the macroscale, the transverse strain (ε_{trans}) induced by the Poisson effect exceeded that of the longitudinally applied strain (ε_{long}) and was nonlinear (Fig 6.3 D). The average macroscale Poisson's ratio was 1.72±0.26. The microscale fiber strain in the transverse direction had a magnitude that was considerably larger than the macroscopic value, with an average Poisson's ratio of 2.90±0.56. Interestingly, the magnitude of the transverse strain for the gel matrix was less than both the fiber and the macroscopic values. The mean matrix Poisson's ratio within the surrogate was 0.57±0.51. The macroscopically measured stress-strain response was nearly linear, with a modulus of 10.55±1.02 MPa (Fig 6.4 upper left).

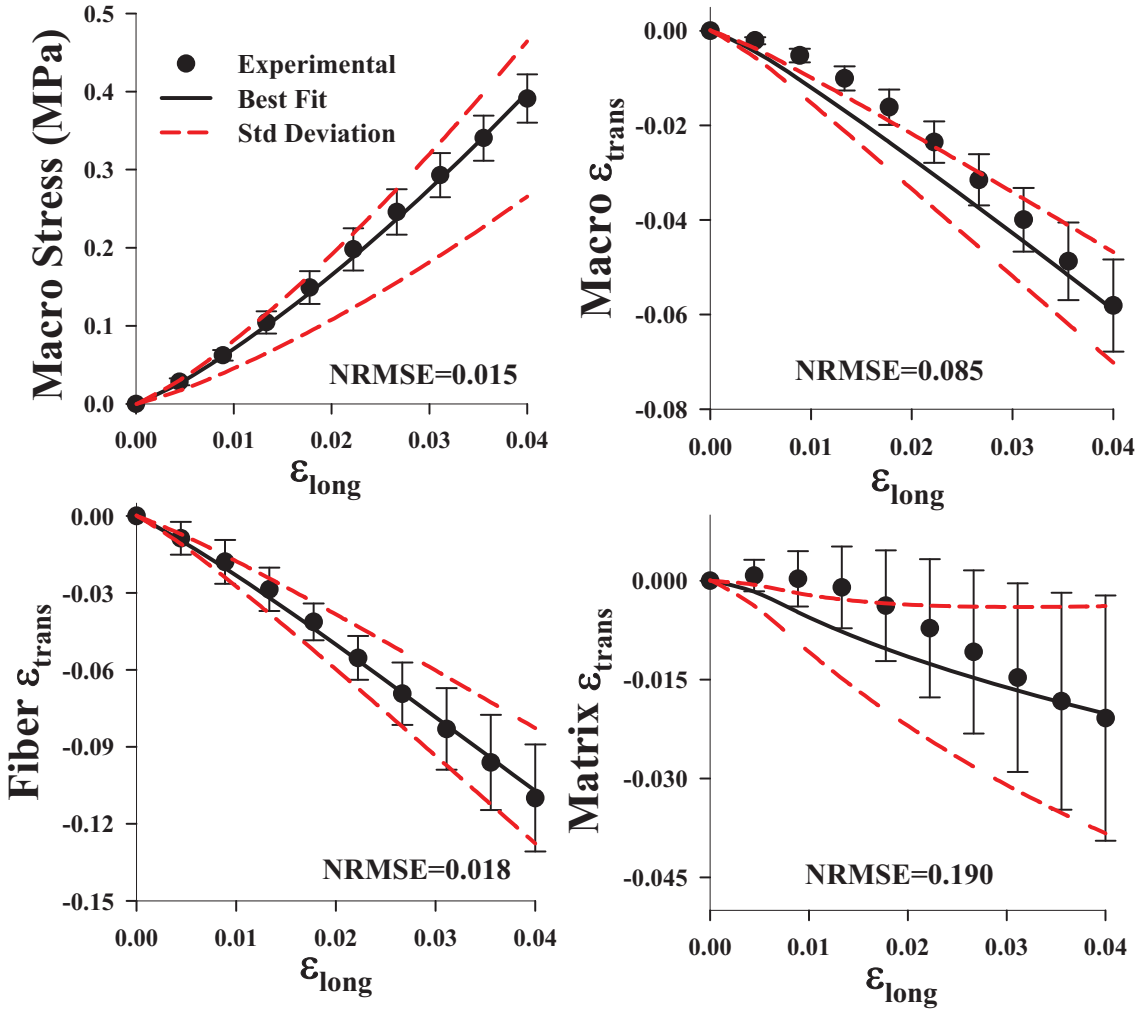

Figure 6.4: Micromechanical FE model validation. The FE model predictions were in excellent agreement with the experimental data. Results are shown for the stress-strain (upper left), the macroscopic strain (upper right), the fiber strain (lower left) and the matrix strain (lower right). In all plots the black points represent the experimental data, the solid black line is the FE prediction obtained using the best fit coefficients and the dashed red lines are the FE predictions obtained using coefficients plus or minus one standard deviation. The normalized root mean square error (NRMSE) are shown at the bottom of each plot.

Gel and fiber characterization

The EFD constitutive model was able to simultaneously describe the uniaxial stress-strain and 2D strain behavior of both the extruded fibers (R^2=0.98) and the collagen gel (R^2=0.99) (Fig 6.5). The fibers were considerably stiffer than the gel (E_{fiber}=215.2±52.1 MPa, E_{gel}=0.091±0.030 MPa). For both materials, the transverse strain induced by the Poisson's effect exceeded the applied longitudinal strain. The average Poisson's ratios were similar, with the fiber having a Poisson's ratio of 2.86±0.42 and the gel having a Poisson's ratio of 2.84±0.79. Considerably more variation was seen in the tensile response of the gel than that of the fibers, as indicated by the large standard deviations for each strain level. Coefficients for the curve fits are provided in Appendix B.

FE micromechanical model and validation

The micromechanical finite element model was created using the experimentally measured surrogate geometry and the optimized gel and fiber coefficients. The model was capable of simultaneously predicting the macroscopic stress-strain behavior as well as the 2D macroscale and microscale strain (Fig 6.4). The predicted macroscopic stress (NRMSE=0.015) and the macroscopic transverse strain (NRMSE=0.085) closely matched the experimentally measured values. The predicted microscopic transverse fiber strain (NRMSE=0.018) was closely matched by the experimentally measured values, while the microscopic transverse matrix strain (NRMSE=0.190) was not as accurately predicted. Large variability was present in the experimental results, especially for the macroscopic and matrix 2D strain. Model simulations performed using coefficients that were varied by a single standard deviation closely bounded this uncertainty.

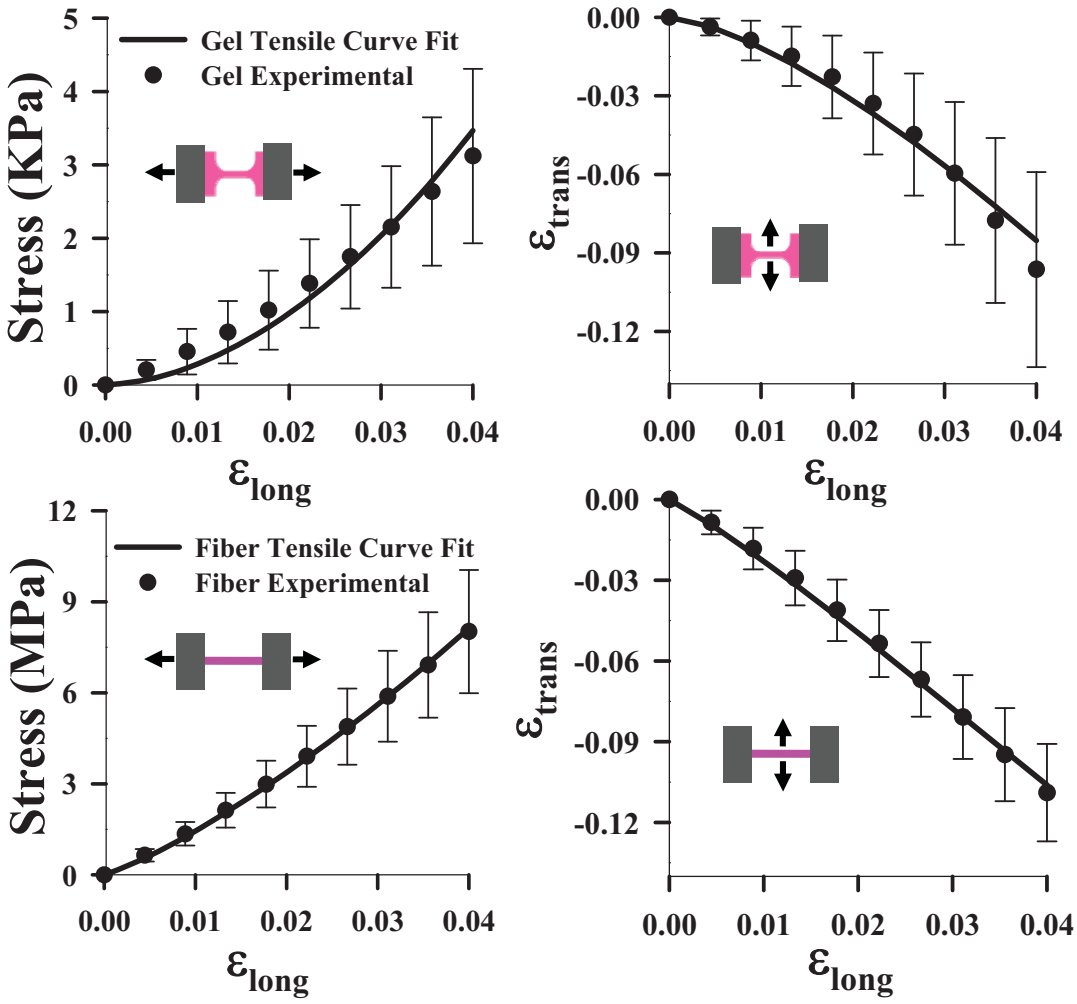

Figure 6.5: Gel and fiber curve fits. The continuous fiber model accurately described the stress-strain (upper left) and 2D strain (upper right) of the collagen gels (R^2=0.98). The continuous fiber model also described the stress-strain (lower left) and 2D strain (lower right) of the extruded fibers (R^2=0.99). In all plots the interpolated data points (with error bars) are black and the best fit curve is black.

This suggests that experimental uncertainty is likely a result of variation of microscale material properties.

Boundary effects

The influence of the constrained boundary at the clamp interface was examined by varying the aspect ratio of the micromechanical model from 4:1 to 80:1. The microscale matrix transverse strain decreased with an increasing aspect ratio (Fig 6.6), as did the macroscale transverse strain (Fig 6.7). An aspect ratio of 40:1 was needed to reach the values obtained for an unconstrained simulation (e.g., no boundary effects).

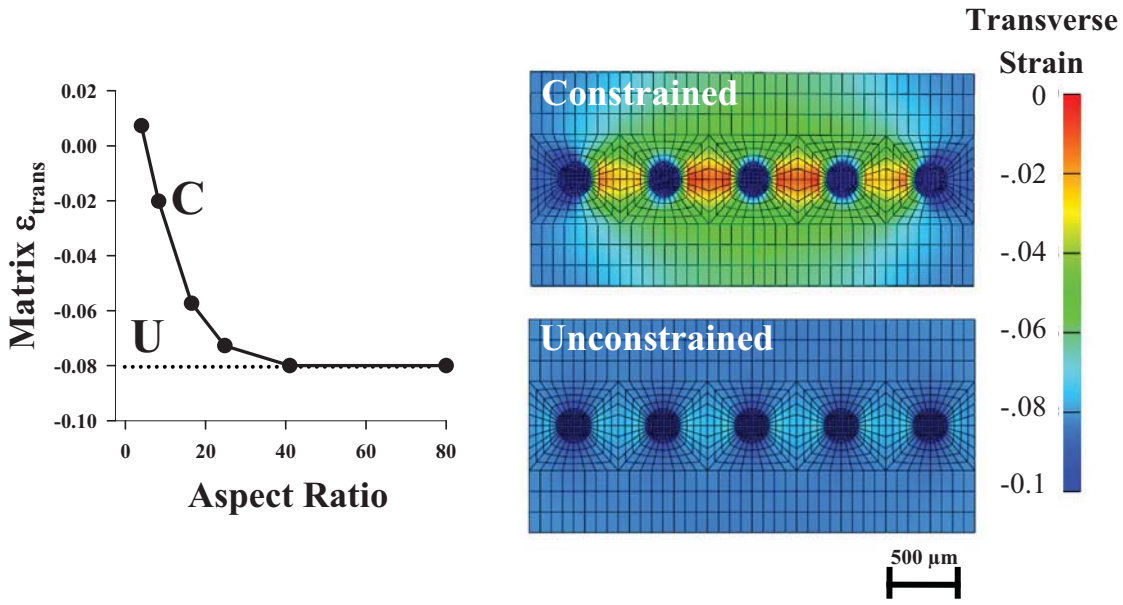

Figure 6.6: Results for boundary effects study. Varying the surrogate aspect ratio had a significant effect on the microscale matrix strain (left plot). The constrained surrogate model (top fringe plot) displayed considerable heterogeneity at the microscale, while the strain field within the unconstrained model was more homogeneous (bottom fringe plot). The corresponding point for the constrained model is designated on the plot with a C. The dotted line represents the value obtained from the unconstrained model and is labeled with a U.

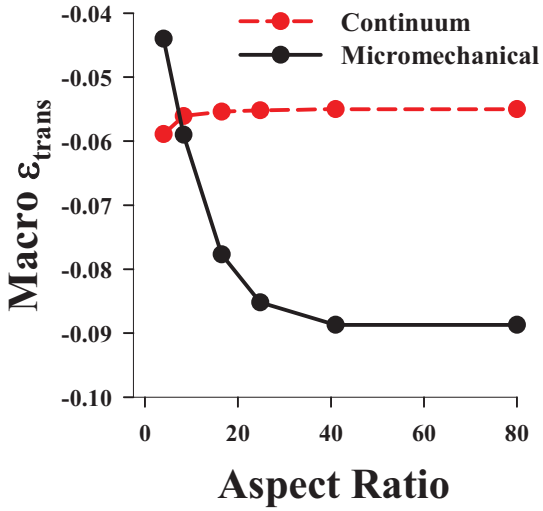

Figure 6.7: Continuum model results. Varying the aspect ratio of the micromechanical model had a significant impact on the macroscopic transverse strain (black points and black line). Varying the aspect ratio of the continuum based model had little effect on the macroscopic strain (red points and dashed red line).

Contour plots of the transverse strain showed that a surrogate model with a constrained boundary has considerable inhomogeneity (coefficient of variation=63.9%), while a surrogate model with an unconstrained boundary does not exhibit this level inhomogeneity (coefficient of variation=12.3%) (Fig 6.6). This reveals that the microscale inhomogeneity observed in the midsubstance of the surrogate is generated by a constrained boundary.

Size effects

To assess the presence of size effects, continuum models with varying aspect ratios were created. In these simulations, the continuum model only matched the micromechanical model for an aspect ratio of 8, which was the aspect ratio for the surrogate (Fig 6.6). Since the continuum model coefficients were obtained by curve

fitting the experimental surrogate test data, this result is expected. However, varying the aspect ratio of the continuum model did not result in a significant change in the macroscopic transverse strain, as was observed for the micromechanical model. This indicates that the continuum assumption is not valid for the surrogate and that size effects are not negligible.

Sensitivity studies

Decreasing the interfiber distance increased the heterogeneity at the microscale, as indicated by the rise in the microscale strain difference, $\Delta\varepsilon_{micro}$ (Fig 6.8). An inter-fiber spacing of 10 μm resulted in a microscale strain difference of $\Delta\varepsilon_{micro}$=0.13, while the surrogate interfiber spacing of 300 μm resulted in a microscale strain difference of $\Delta\varepsilon_{micro}$=0.08. Increasing the stiffness of the matrix resulted in a decrease in heterogeneity, as indicated by a lower microscale strain difference with a decrease in the ratio of fiber stiffness to matrix stiffness (E_{fiber}/E_{matrix}) (Fig 6.8).

Discussion

The physical surrogates created in this study emulated structural features found in tendon and ligament tissue, including a nanoscale organization of collagen fibrils and a mesoscale organization of aligned collagen fibers coupled via an interfiber matrix. The surrogate reproduced a number of behaviors that are similar to those observed in native tissue. The macroscale Poisson's ratios were in the range of those reported for tendon and ligament [34, 35]. At the microscale, the Poisson's ratio and linear modulus of the extruded fibers matched the experimental values for tendon fascicles [36].

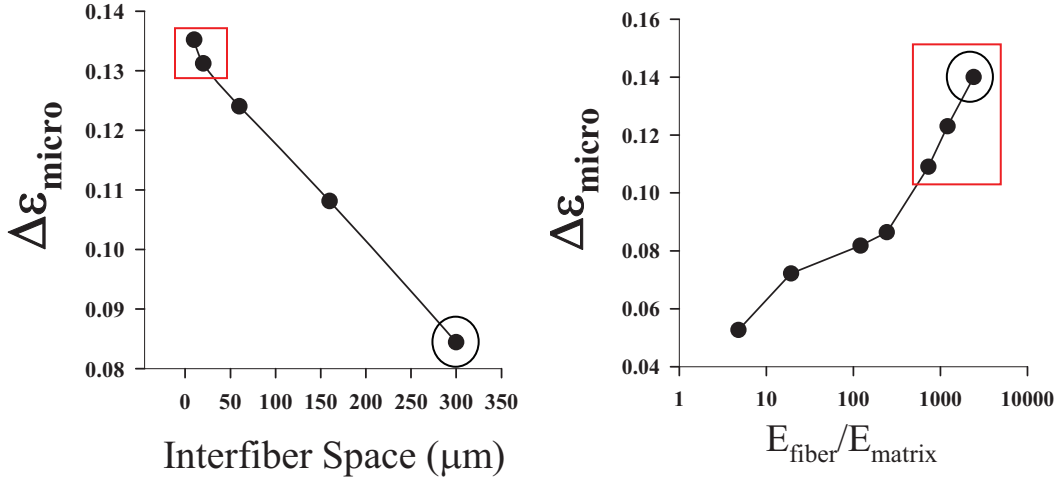

Figure 6.8: Sensitivity studies. (Left) As the interfiber distance was decreased, the difference between the fiber and matrix strain increased. The surrogate spacing is circled in black, while the physologically relvent values are boxed in red. (Right) For a constant interfiber spacing of 10 μm, an increase in the ratio of the fiber stiffness to the matrix stiffness resulted in a larger microscale strain difference between the fiber and matrix. The value corresponding to the surrogate matrix is circled in black, while the physiologically relevant values are boxed in red.

The experimentally measured macroscale surrogate strain was not representative of the microscale strain, which was highly inhomogeneous. The transverse strain within the interfiber gel matrix was dissimilar from the transverse strain measured within the fiber. This behavior is qualitatively similar to the inhomogeneous strains experimentally observed at the mesoscale and the microscale in tendon tissue [8, 9, 37].

To investigate the source of this microscale inhomogeneity, a micromechanical model of the surrogate was created. This model was validated at multiple scales and dimensions, which allowed the model to be extended to simulate tests that would have been difficult to perform experimentally. By creating models with varied aspect ratios and comparing them to an unconstrained model, it was revealed that the constrained boundary at the clamp was responsible for the inhomogeneous strain field experimentally

observed at the microscale. According to continuum theory, the size of microstructural features must be infinitesimally small in comparison to the macroscale [22]. A continuum model did not predict these boundary effects. This indicates that the continuum assumption is not valid for describing the macroscale behavior of the surrogate and that boundary induced size effects are present.

To determine the relevance of the model in describing the mechanics of native tissue, a sensitivity study was performed. The interfiber spacing of the surrogate was much larger than is present in tendon and ligament. Spacing between fascicles within tendon ranges between 5-20 μm, while the spacing in the surrogate was 300 μm. The sensitivity study revealed that decreasing the interfiber spacing actually led to an increase in the inhomogeneity between the matrix and fiber strain. It has been estimated that the matrix material is 500-5000 times more compliant than the fibers [38]. A sensitivity study on the matrix stiffness revealed that considerable strain inhomogeneity is present within this range. For a physiologically relevant model with an interfiber spacing of 10 μm and a gel stiffness ~2500 times that of the fiber, the predicted matrix strain was positive (matrix $\varepsilon_{trans} = 0.03$) while the fiber strain was negative (fiber $\varepsilon_{trans} = -0.10$). If the micromechanical model predictions are indicative of in vivo mesoscale behavior, then these results could have important implications. Histological studies have shown that vessels and nerves are located between fascicles at the mesoscopic level [14, 39]. If present within native tissue, positive transverse interfiber strains may play a role in regulating blood flow within a tendon. The presence of large negative transverse strains within a fascicle may play a role in nutrient transport. Large strains are indicative of volume loss and thus fluid exudation, as described by biphasic theory [36, 38, 40].

Since the surrogate represented a simplified physical model, certain features found in native tendon were not emulated. Fiber crimp was not included, and thus the nonlinear stress-strain response typical for tendon was not observed. The extruded fibers were composed of aligned collagen fibrils. However, the fibrils were not organized into the characteristic ~20 μm fibers that are seen in native tendon. Finally, other ECM components such as elastin and proteoglycans were not included. Inclusion of such features may have provided a more physiologically relevant model. However, it would have come at the cost of simplicity in model construction, analysis and hypothesis testing. Nevertheless, these features can be investigated as part of future studies using the surrogate approach.

Although the FE predictions for the stress and 2D strain were quite good, the predicted microscale transverse matrix strain did not fully replicate the experimentally measured behavior. The constructs were observed to shrink a small amount when put into the formalin/gluteraldehyde mixture. It is hypothesized that the gel shrunk more than the fibers (driven by osmotic forces), which generated a prestress within the matrix. Another possible source of error is that of clamping effects on the gel matrix. When testing the gel specimens it was necessary to embed the tabs in melamine foam. Without this step, the clamping effects affected the tensile response. Since the constructs did not have the foam embedded in the ends that were gripped, this may have introduced an additional clamping effect that was not captured by the model. Although the matrix behavior was not perfectly replicated, the predicted result is still within a range deemed acceptable, with an NRMSE of less than 0.2.

The physical surrogate in this study was able to emulate the mesoscale microstructure of tendon and allowed for a controlled means of investigating size effects in the presence of a constrained boundary. Sensitivity studies indicated that the results of this model may have relevance to native tendon and ligament tissue, where experimental evidence suggests the presence of such size effects [8, 9]. In the future, the use of physical models could provide a means for developing and validating more complex and physiologically relevant computational models. Since size effects may play an important role in the normal function of tendon and ligament, the results of this work suggest that future modeling studies should carefully consider if a continuum assumption is adequate for the intended use of the model. In addition to its contribution in the field of multiscale tendon mechanics, this study also has relevance to the tissue engineering field, where computational modeling is poised to help develop future generations of tissue engineering scaffolds.

References

[1] Frank, C. B., 1996, "Ligament Healing: Current Knowledge and Clinical Applications," J Am Acad Orthop Surg, 4(1), pp. 74-83.

[2] Fredberg, U., and Stengaard-Pedersen, K., 2008, "Chronic Tendinopathy Tissue Pathology, Pain Mechanisms, and Etiology with a Special Focus on Inflammation," Scandinavian Journal of Medicine & Science in Sports, 18(1), pp. 3-15.

[3] Sharma, P., and Maffulli, N., 2005, "Tendon Injury and Tendinopathy: Healing and Repair," The Journal of Bone and Joint Surgery (American Volume), 87(1), pp. 187-202.

[4] Kannus, P., 2000, "Structure of the Tendon Connective Tissue," Scand J Med Sci Sports, 10(6), pp. 312-20.

[5] Gotoh, T., Murashige, N., and Yamashita, K., 1997, "Ultrastructural Observations on the Tendon Sheath of the Rat Tail," J Electron Microsc (Tokyo), 46(3), pp. 247-52.

[6] Smith, K. D., Vaughan-Thomas, A., Spiller, D. G., Innes, J. F., Clegg, P. D., and Comerford, E. J., 2011, "The Organisation of Elastin and Fibrillins 1 and 2 in the Cruciate Ligament Complex," J Anat, 218(6), pp. 600-7.

[7] Haraldsson, B. T., Aagaard, P., Qvortrup, K., Bojsen-Moller, J., Krogsgaard, M., Koskinen, S., Kjaer, M., and Magnusson, S. P., 2008, "Lateral Force Transmission between Human Tendon Fascicles," Matrix Biol, 27(2), pp. 86-95.

[8] Komolafe, O. A., and Doehring, T. C., 2010, "Fascicle-Scale Loading and Failure Behavior of the Achilles Tendon," J Biomech Eng, 132(2), pp. 021004.

[9] Screen, H. R., Lee, D. A., Bader, D. L., and Shelton, J. C., 2004, "An Investigation into the Effects of the Hierarchical Structure of Tendon Fascicles on Micromechanical Properties," Proc Inst Mech Eng [H], 218(2), pp. 109-19.

[10] Screen, H. R. C., and Cheng, V. W. T., 2007, "The Micro-Structural Strain Response of Tendon," Journal of Material Science, 19, pp. 1-2.

[11] Fung, D. T., Wang, V. M., Laudier, D. M., Shine, J. H., Basta-Pljakic, J., Jepsen, K. J., Schaffler, M. B., and Flatow, E. L., 2009, "Subrupture Tendon Fatigue Damage," J Orthop Res, 27(2), pp. 264-73.

[12] Nakama, L. H., King, K. B., Abrahamsson, S., and Rempel, D. M., 2005, "Evidence of Tendon Microtears Due to Cyclical Loading in an in Vivo Tendinopathy Model," J Orthop Res, 23(5), pp. 1199-205.

[13] Ritter, M. C., Jesudason, R., Majumdar, A., Stamenovic, D., Buczek-Thomas, J. A., Stone, P. J., Nugent, M. A., and Suki, B., 2009, "A Zipper Network Model of the Failure Mechanics of Extracellular Matrices," Proc Natl Acad Sci U S A, 106(4), pp. 1081-6.

[14] Wang, J. H., 2006, "Mechanobiology of Tendon," J Biomech, 39(9), pp. 1563-82.

[15] Tozer, S., and Duprez, D., 2005, "Tendon and Ligament: Development, Repair and Disease," Birth Defects Res C Embryo Today, 75(3), pp. 226-36.

[16] Hirokawa, S., 2003, "An Experimental Study of the Microstructures and Mechanical Properties of Swine Cruciate Ligaments," JSME International Journal, 46(4), pp. 1417-1425.

[17] Miyasaka, K. C., Daniel, D. M., Stone, M. L., and Hirshman, P., 1991, "The Incidence of Knee Ligament Injuries in the General Population," Am J Knee Surg, 4, pp. 3-8.

[18] Yamamoto, E., Hayashi, K., and Yamamoto, N., 1999, "Mechanical Properties of Collagen Fascicles from the Rabbit Patellar Tendon," J Biomech Eng, 121(1), pp. 124-31.

[19] Thomopoulos, S., Williams, G. R., Gimbel, J. A., Favata, M., and Soslowsky, L. J., 2003, "Variation of Biomechanical, Structural, and Compositional Properties Along the Tendon to Bone Insertion Site," J Orthop Res, 21(3), pp. 413-9.

[20] Danylchuk, K. D., Finlay, J. B., and Krcek, J. P., 1978, "Microstructural Organization of Human and Bovine Cruciate Ligaments," Clin Orthop Relat Res, (131), pp. 294-8.

[21] Buechner, P. M., and Lakes, R. S., 2003, "Size Effects in the Elasticity and Viscoelasticity of Bone," Biomech Model Mechanobiol, 1(4), pp. 295-301.

[22] Kouznetsova, V. G., Geers, M. G. D., and Brekelmans, W. a. M., 2004, "Multi-Scale Second-Order Computational Homogenization of Multi-Phase Materials: A Nested Finite Element Solution Strategy," Computer Methods in Applied Mechanics and Engineering, 193(48-51), pp. 5525-5550.

[23] Caves, J. M., Kumar, V. A., Wen, J., Cui, W., Martinez, A., Apkarian, R., Coats, J. E., Berland, K., and Chaikof, E. L., 2010, "Fibrillogenesis in Continuously Spun Synthetic Collagen Fiber," Journal of Biomedical Materials Research, Part B: Applied Biomaterials, 93(1), pp. 24-38.

[24] Pins, G. D., Christiansen, D. L., Patel, R., and Silver, F. H., 1997, "Self-Assembly of Collagen Fibers. Influence of Fibrillar Alignment and Decorin on Mechanical Properties," Biophys J, 73(4), pp. 2164-72.

[25] Vader, D., Kabla, A., Weitz, D., and Mahadevan, L., 2009, "Strain-Induced Alignment in Collagen Gels," PLoS One, 4(6), pp. e5902.

[26] Iwasaki, S., Hosaka, Y., Iwasaki, T., Yamamoto, K., Nagayasu, A., Ueda, H., Kokai, Y., and Takehana, K., 2008, "The Modulation of Collagen Fibril Assembly and Its Structure by Decorin: An Electron Microscopic Study," Arch Histol Cytol, 71(1), pp. 37-44.

[27] Lujan, T. J., Underwood, C. J., Henninger, H. B., Thompson, B. M., and Weiss, J. A., 2007, "Effect of Dermatan Sulfate Glycosaminoglycans on the Quasi-Static Material Properties of the Human Medial Collateral Ligament," J Orthop Res, 25(7), pp. 894-903.

[28] Upton, M. L., Gilchrist, C. L., Guilak, F., and Setton, L. A., 2008, "Transfer of Macroscale Tissue Strain to Microscale Cell Regions in the Deformed Meniscus," Biophys J, 95(4), pp. 2116-24.

[29] Gilchrist, C. L., Witvoet-Braam, S. W., Guilak, F., and Setton, L. A., 2007, "Measurement of Intracellular Strain on Deformable Substrates with Texture Correlation," J Biomech, 40(4), pp. 786-94.

[30] Bonet, J., and Wood, R., 1997, *Nonlinear Continuum Mechanics for Finite Element Analysis*, Cambridge University Press, Cambridge, England.

[31] Ateshian, G. A., Rajan, V., Chahine, N. O., Canal, C. E., and Hung, C. T., 2009, "Modeling the Matrix of Articular Cartilage Using a Continuous Fiber Angular Distribution Predicts Many Observed Phenomena," J Biomech Eng, 131(6), pp. 061003.

[32] Roeder, B. A., Kokini, K., Sturgis, J. E., Robinson, J. P., and Voytik-Harbin, S. L., 2002, "Tensile Mechanical Properties of Three-Dimensional Type I Collagen Extracellular Matrices with Varied Microstructure," J Biomech Eng, 124(2), pp. 214-22.

[33] Krishnan, L., Weiss, J. A., Wessman, M. D., and Hoying, J. B., 2004, "Design and Application of a Test System for Viscoelastic Characterization of Collagen Gels," Tissue Engineering, 10(1-2), pp. 241-52.

[34] Hewitt, J., Guilak, F., Glisson, R., and Vail, T. P., 2001, "Regional Material Properties of the Human Hip Joint Capsule Ligaments," J Orthop Res, 19(3), pp. 359-64.

[35] Lynch, H. A., Johannessen, W., Wu, J. P., Jawa, A., and Elliott, D. M., 2003, "Effect of Fiber Orientation and Strain Rate on the Nonlinear Uniaxial Tensile Material Properties of Tendon," J Biomech Eng, 125(5), pp. 726-31.

[36] Yin, L., and Elliott, D. M., 2004, "A Biphasic and Transversely Isotropic Mechanical Model for Tendon: Application to Mouse Tail Fascicles in Uniaxial Tension," J Biomech, 37(6), pp. 907-16.

[37] Screen, H. R. C., Bader, D. L., Lee, D. A., and Shelton, J. C., 2004, "Local Strain Measurement within Tendon," Strain, 40(4), pp. 157-163.

[38] Reese, S., and Weiss, J., 2010, "Measurement of Poisson's Ratio and Transverse Strain in Rat Tail Tendon During Stress Relaxation," Proc. of the 56th Annual Meeting of the Orthopaedic Research Society, New Orleans, LA.

[39] Kjaer, M., 2004, "Role of Extracellular Matrix in Adaptation of Tendon and Skeletal Muscle to Mechanical Loading," Physiol Rev, 84(2), pp. 649-98.

[40] Armstrong, C. G., Lai, W. M., and Mow, V. C., 1984, "An Analysis of the Unconfined Compression of Articular Cartilage," J Biomech Eng, 106(2), pp. 165-73.

CHAPTER 7

DISCUSSION

Summary

The objective of this work was to address a number of outstanding questions regarding the structure-function relationships that underlie the mechanical behavior of tendon and ligament tissue. Starting at the nanoscale, in vitro polymerization of type I collagen gels was used as a model for investigating the role of decorin during fibrillogenesis. At the microscale, nonlinear homogenization techniques were combined with novel micromechanical models to test the hypothesis that a helical fibril organization can generate large Poisson's ratios during uniaxial tension. At the mesoscale, the biphasic behavior of single tendon fascicles was investigated during stress relaxation testing. Finally, collagen based physical models were coupled with micromechanical FE models to study multiscale interactions within tendon tissue. The major findings of this work include:

1) The presence of decorin during the in vitro polymerization of type I collagen gels leads to an increased tensile strength and modulus. This increased strength appears to be a result of decorin's ability to modulate the process of fibrillogenesis in such a way as to create a fibril network with smaller diameter fibers and more fibril interconnections.

2) A helical organization of fibrils embedded within a matrix material predicts homogenized Poisson's ratios that are comparable to those experimentally observed in tendon and ligament. A superhelical fibril organization superimposed on fiber crimp simultaneously predicts both large Poisson's ratios and the nonlinear stress strain response, while crimp alone predicts only a nonlinear stress-strain response.
3) During stress relaxation, the time depended Poisson's ratio in tendon fascicles is linearly correlated with the time dependent stress. This is consistent with predictions made by biphasic theory, which suggests that some or all of the apparent viscoelastic response of tendon fascicles is attributable to the fluid dependent mechanism postulated by biphasic theory.
4) Collagen based physical models coupled to micromechanical FE models provide a means for isolating and studying multiscale organizational features of tendon and ligament. The use of a validated micromechanical model reveals that microscale size effects in the presence of a constrained boundary are responsible for the inhomogeneous strain field that is experimentally observed within the physical model at the microscale.

Although present in small quantities within the tissue, decorin is believed to play an important role in the macroscopic function of ligament and tendon. However, studies in which the decorin GAG side chain was digested revealed that decorin does not crosslink adjacent collagen fibrils via the dermatan sulfate side chain [1, 2]. In light of this evidence, other roles for decorin have been sought. As discussed in previous chapters, it is hypothesized that decorin may indirectly modulate the mechanical properties of

ligament by regulating fibril organization during fibrillogenesis. In vitro studies suggested that decorin modifies the fibril diameter of collagen. This hypothesis is corroborated by studies in developing chick embryos in which a cessation of lateral fibril fusions was concurrent with an increase in decorin mRNA expression [3]. However, no direct link between the presence of decorin during polymerization and the resulting mechanical properties had been established. The study presented in Chapter 3 provided that link by revealing that the presence of decorin during fibrillogenesis resulted in gels that were significantly stronger than gels polymerized in the absence of decorin. Furthermore, it was discovered that only the core protein is needed to facilitate this effect. Interestingly, the presence of dermatan sulfate by itself resulted in significantly weaker gels, suggesting that dermatan sulfate behaves differently when attached to the core protein. It is plausible that dermatan sulfates attachment to the decorin core protein plays no role in mechanics or fibrillogenesis. It has been suggested that dermatan sulfate acts as a reservoir for growth factors [4]. The attachment of dermatan sulfate to the core protein may be a means of preventing dermatan sulfate from negatively impacting fibrillogenesis while still facilitating its presence for the purpose of binding growth factors. It is hypothesized that other proteoglycans, such as biglycan and lumican, may also be of importance [5]. The in vitro system developed provides a systematic means for studying the effect of these and other molecules on the process of fibrillogenesis.

The relationship between fibril organization and the macroscopic material behavior has been a topic of study in ligament mechanics for several decades. Numerous modeling studies utilizing analytical methods have corroborated the hypothesis that the nonlinear toe region of the stress-strain response is a result of the uncrimping and

sequential recruitment of collagen fibers [6-9]. However, no studies have examined the structure-function relationships that underlie the considerable volumetric behavior of tendon (i.e., a Poisson's ratio in excess of the isotropic limit). In spite of the potential importance of this behavior, its structural underpinnings have not been investigated. Microscopic observations have suggested that helical organizational structures are present within fibers and fascicles [10, 11]. In Chapter 4, nonlinear homogenization techniques were used to compute the effective Poisson's ratios of micromechanical models that featured crimped fibrils with a superhelical organization. Although nonlinear FE based homogenizations of a unit cell have been employed in the composites field for a number of years [12], this study represents the first application of these methods to biological composites such as tendon and ligament. Homogenization techniques provide a computational framework for addressing a number of structure-function based hypotheses in 3D that would be difficult to address using analytical, linear or 2D computational approaches.

The viscoelastic response of tendon and ligament plays an important role in the normal function of these tissues, yet the underlying mechanisms are still poorly understood. Both solid and fluid phase mechanisms have been proposed. Solid phase mechanisms include fibrillar sliding and an intrinsic viscoelasticity within the interfiber matrix. The fluids phase mechanism is described using biphasic theory, in which energy is dissipated via fluid flux through a porous matrix. In light of the porous, hydrated nature of ligament and its large volumetric response, this mechanism seems particularly relevant. Unlike solid phase viscoelastic models such as QLV, biphasic theory intrinsically requires volumetric changes in response to tensile loading. Experimentally,

both a time dependent stress and a time dependent 3D strain are expected. This motivates a rich set of experiments that can be used to test the biphasic hypothesis. In Chapter 5, the first measurements of time dependent Poisson's ratios in tendon were presented. As hypothesized by biphasic theory, the time dependent stress and Poisson's ratios were linearly correlated during stress relaxation testing. A previously published study found that biphasic theory was capable of describing the stress relaxation behavior of single tendon fascicles [13]. By measuring an additional dimension (Poisson's ratios), this study provided a more robust test of the biphasic hypothesis.

As discussed in Chapters 2 and 6, force transmission, damage mechanisms and mechanotransduction are phenomena that result from complex interactions between scale levels. Experimental studies have begun to address these multiscale interactions. However, isolating the structure-function mechanisms at each level is difficult. These difficulties arise from a number of variables that are hard to account for, including complex three-dimensional microscale structures, inhomogeneity in material properties and the challenge of removing and testing individual components at different scale levels. In Chapter 6, the use of a collagen based tendon surrogate was proposed as a simplified means for isolating multiscale structural features. This provided a useful tool for the study of multiscale interactions and simplified the development of multiscale modeling and validation methods. For this study, extruded collagen fibers were embedded within a collagen gel matrix, which emulated the mesoscale organization of fascicles within a tendon. A micromechanical FE model of the surrogate was created and experimentally validated at two scale levels using confocal microscopy techniques. The surrogate was capable of reproducing a number of features that have been experimentally observed in

tendon, including large Poisson's ratios and inhomogeneity within the microscale strain field. The validated micromechanical model was used to explore the presence of boundary effects within the surrogate. By varying the aspect ratio of the model, it was revealed that microscale inhomogeneity within the strain field was induced by boundary effects. In the absence of a constrained boundary, this inhomogeneity largely subsided. As in tendons, the microstructural features of the surrogate did not satisfy the continuum requirement of being infinitesimally small in comparison to the macroscale. Simulations using a continuum based model did not replicate the boundary effect seen in the micromechanical models. This indicated that the continuum assumption was not valid and that scale effects could not be ignored. A sensitivity study revealed that size effects were significant over a range of physiologically relevant interfiber spacing values and matrix material properties. Although utilizing the continuum assumption for multiscale modeling of tendon (e.g., 1^{st} order homogenization schemes) may prove useful for modeling macroscopic behavior, this study suggested that it may not accurately reconstruct the microscale strain environment. Although the tendon surrogate represented a considerable simplification, its combination with a validated micromechanical FE model provided valuable insights into the multiscale behavior of materials with structural features similar to that of tendon and ligament.

Limitations

As with all studies, the work in this dissertation is subject to a number of limitations. Although the vitro approach in Chapter 3 allowed for the interactions of decorin and type I collagen to be isolated, the conclusions from this approach may not directly translate to in vivo fibrillogenesis. In vitro polymerization of collagen is

performed by precipitating acid solubilized collagen via an increase in pH. Although in vivo fibrillogenesis is poorly understood, it appears that procollagen bundles are excreted into the ECM, at which point extracellular proteases cleave the propeptide regions to create tropocollagen. After cleavage of the propeptide regions, the solubility of collagen decrease by a factor of 10,000, which causes the tropocollagen to precipitate out of solution and form fibrils [14]. Since both in vivo and in vitro fibrillogenesis are mediated by a drop in solubility, it seems reasonable to assume that in vitro experiments are, at least in part, providing information relevant to in vivo processes. Although both in vitro and in vivo mechanisms of fibrillogenesis result from a decrease in solubility of collagen, the mechanisms by which this occurs are different. Another relevant difference between in vitro and in vivo fibrillogenesis is the rate at which collagen precipitates out of solution. In vitro, a fixed concentration of collagen is precipitated out of solution over a short time period. In vivo, collagen is excreted by fibroblasts at low concentrations, and thus collagen precipitation is a process that occurs over a long time course. These differences must be kept in mind when interpreting the results of in vitro studies of collagen gels.

In Chapter 4, homogenization techniques were used to obtain macroscopic material properties. One of the assumptions in this homogenization is that the macroscale could be represented by a simple repeat of a unit cell. As discussed in Chapter 2, the tendon microstructure spans multiple organizational scales. In particular, adjacent fascicles may not be homogenous and fully coupled [15, 16]. If this is the case, then the unit cells presented in this study would be more appropriate for obtaining homogenized material properties of single fascicles, rather than the macroscopic tissue. Imaging

studies have revealed considerable branching and interweaving of fibers within fascicles [17]. Emulating this behavior would require a unit cell that also features branched and weaving fibers, which was not modeled in this study. It is clear that the unit cell utilized in Chapter 4 is not an exact representation of the complex structure of tendon and ligament. Nevertheless, the use of a simplified unit cell proved useful, as it enabled the testing of a number of structure function hypotheses that were difficult to address using previous analytical models. Furthermore, such an approach was capable of reproducing the experimentally observed behavior. This suggests that perhaps certain microscale and mesoscale features can be ignored if the primary level of interest is the macroscale. This approach has been taken by other modeling studies, in which "averaged" values for crimp and fiber stiffness were used [18, 19].

The primary limitation in Chapter 5 is the assumption that single fascicles have a circular cross sectional profile. Histological studies have indicated that a fascicle cross section is more accurately described as a triangular structure. Because the cross section was not circular, the observed shape change of the fascicles at low strains was unpredictable. The consequence was that the 2D strain could not be accurately measured within the toe region. To address this shortcoming, a system for measuring the 3D structure of the fascicle would be required. It was observed that past the toe region, the shape of the fascicle had stabilized into what appeared to be a cylinder. Thus, this shortcoming was addressed by making strain measurements relative to the transition strain (the point at which the nonlinear toe region becomes linear). This allowed for the time dependent stress and Poison's ratio to be measured during stress relaxation testing. Because the nonlinear behavior of the fascicle was not captured, the results were not

amenable to performing biphasic curve fits, which would have strengthened the conclusions made from the study.

In Chapter 6, the primary limitation in the use of collagen based physical models was that they did not reconstruct all of the multiscale features present within tendon and ligament. Since fiber crimp was not emulated, the stress-strain response was nearly linear. Because of this, the micromechanical models of the surrogates cannot be directly utilized in simulation of tendon and ligament tissue. In the future, surrogate complexity could be increased by adding additional levels of complexity, such as crimp. However, one of the attractive aspects of using a surrogate is the ability to isolate a small number of features. Too much complexity in a model may make it intractable and difficult to validate. Clearly, a balance between model complexity, relevance to native tissues and tractability must be found. Perhaps future studies can incrementally add model complexity, which would allow additional studies to build on the findings of previous studies.

Preliminary Studies

In order to extend the work presented in this dissertation, a number of preliminary studies have been performed. These include the development of a strain energy function to model the volumetric response of ligament, the application of a poroviscoelastic model in describing the viscoelastic behavior of ligament and novel 3D microscopy methods for observing the complex structural organization of fibrils and fibers within tendon.

A strain energy function to describe the

volumetric behavior of ligament

There exists a need for a strain energy formulation that can simultaneously describe the nonlinear stress-strain behavior and the volumetric behavior of ligament. To address this need, a fully coupled strain-energy function was developed that includes a fiber, matrix and volumetric term. The fiber and matrix terms were given the form:

$$W_{fiber} = \frac{1}{2}\frac{c_1}{c_2}\left(e^{c_2\left(\sqrt{I_4}-1\right)^2} - 1 \right) \tag{7.1}$$

$$W_{matrix} = \frac{\mu}{2}\left(I_1 - 3\right) - \mu Log\left(\sqrt{I_3}\right) + \frac{\Lambda}{2} Log\left(\sqrt{I_3}\right)^2 \tag{7.2}$$

where the fiber term was obtained from [20] and the matrix term was taken to be a compressible neo-Hookean material with the lame coefficients μ and Λ [21]. The derivation of a volumetric term is as follows. The cross sectional area normal to the fiber direction $\mathbf{a}_0$ is controlled by the Poisson's ratio in the fiber plane (ν_{31}) and the fiber stretch, $\lambda=\sqrt{I_4}$, where the fiber direction $\mathbf{a}_0$ is initially taken to be in the $\mathbf{e}_1$ direction. The change in cross-sectional area is defined, where dA and da are the areas in the reference and current configuration:

$$\left(da/dA\right)^2 = \left(1 - \nu_{31}\left(\sqrt{I_4} - 1\right)\right)^4 \tag{7.3}$$

A similar expression can be obtained using Nanson's relation and the Cayley-Hamilton theorem [22]:

$$\left(da/dA\right)^2 = \left(I_5 - I_1 I_4 + I_2\right) \tag{7.4}$$

Equations 7.1 & 7.2 are equal for uniaxial tension, and thus their ratio should equal one. A convex function that is stress-free at the reference configuration can then be generated:

$$W_{volume} = \ln\left[\frac{\left(I_5 - I_1 I_4 + I_2\right)}{\left(1 - v_{31}\left(I_4\right)\left(\sqrt{I_4} - 1\right)\right)^4}\right]^2 \tag{7.5}$$

A linear form for the Poisson's function, v_{31} was used for this preliminary study:

$$v_{31} = m\left(\sqrt{I_4} - 1\right) + v_0 \tag{7.6}$$

Finally, the total strain energy function is given by:

$$W = W_{fiber} + W_{matrix} + W_{volume} \tag{7.7}$$

Formulations for the Cauchy stress were derived and are presented in Appendix C. The model was fit to stress-strain data and Poisson's ratio-strain data (the Poisson's function) for rabbit MCL [23] using a two step procedure. In a uniaxial tensile test (fiber axis aligned with $\mathbf{e}_1$), the transverse stress ($\boldsymbol{\sigma}_{33}$) will be zero. Thus the 2D strain ($\boldsymbol{\varepsilon}_{11}$-$\boldsymbol{\varepsilon}_{33}$) data were curve fit using the constraint that $\boldsymbol{\sigma}_{33}$ must be zero for all strain levels. The equation for the $\boldsymbol{\sigma}_{33}$ component only depends on the matrix and volumetric strain energy terms, and thus this curve fit yielded the coefficients m, ν_0, μ and Λ. These coefficients were then used in curve fitting the longitudinal stress-strain ($\boldsymbol{\sigma}_{11}$) data, which yielded the fiber coefficients, c_1 and c_2. Both curve fits were performed using the sequential quadratic programming method that is implemented in Matlab's fmincon function. The two step optimization method resulted in excellent fits (Fig 7.1), demonstrating that a volumetric strain energy term can model the Poisson's function seen experimentally.

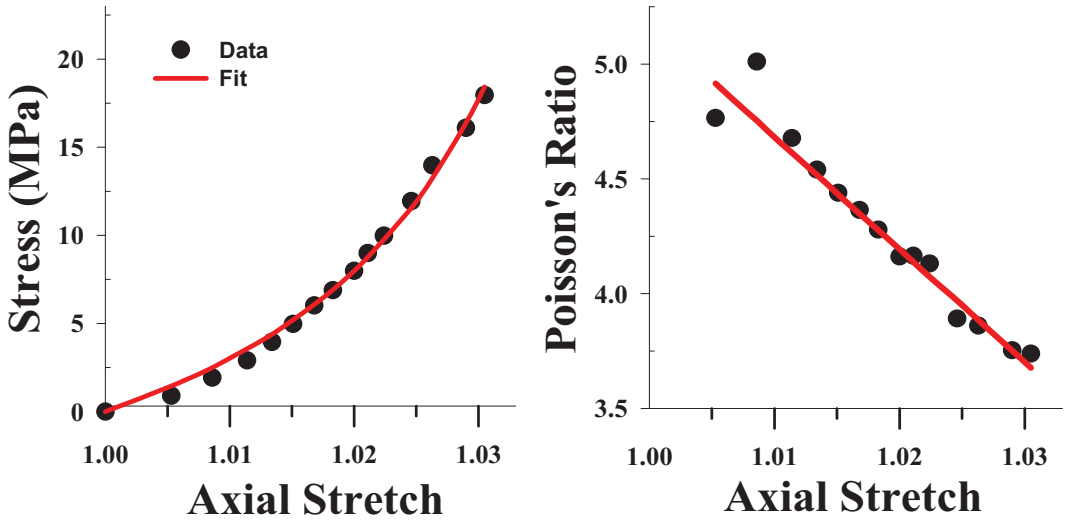

Figure 7.1: Volumetric strain energy function curve fits. The new strain energy function simultaneously described the stress-strain (left) and Poisson's ratio-strain (right) data that were experimentally measured for rabbit MCL.

Poroviscoelastic modeling

In this preliminary study it was hypothesized that the apparent viscoelasticity of tendon and ligament can be described by a combination of a flow dependent and a flow independent contribution, similar to previous studies on cartilage [24, 25]. To demonstrate feasibility, experimental data for the complex modulus [26] were curve fit to three different models: a QLV solid phase viscoelastic model, a transversely isotropic biphasic model [27] and an isotropic poroviscoelastic model [25]. The theory of poroviscoelasticity postulates that the solid phase viscoelasticity is restricted to the deviatoric stress response and can be described by QLV theory:

$$\boldsymbol{\sigma}(t) = \int_{t=0}^{t} G(t-\tau) \cdot \boldsymbol{\sigma}_{dev}(\boldsymbol{\varepsilon})\, dt \tag{7.8}$$

where $\boldsymbol{\sigma}_{dev}$ is the deviatoric stress tensor and G is the reduced relaxation function given by:

$$G(t) = 1 + c\int_{\tau_1}^{\tau_1} \frac{e^{-t/\tau}}{\tau} d\tau \tag{7.9}$$

In linear viscoelasticity, the complex modulus, *M**, can be obtained from the relaxation function using [28]:

$$M^* = i\omega \cdot L\left[G(t)\right]_{s=i\omega} \tag{7.10}$$

where *L*[ ] is the Laplace transform and ω is the frequency (in radians). Using this relation, the complex modulus for the solid phase response represented by Equation 7.9 is:

$$M^*_{QLV}\left(\omega\right) = \mu\left(1 + cLog\left[\frac{i\omega\tau_2 + 1}{i\omega\tau_2 + 1}\right]\right) \tag{7.11}$$

in which c, τ_1 and τ_2 are the coefficients for the relaxation function and μ is the shear modulus. The complex modulus for a biphasic, transversely isotropic cylinder subjected to unconstrained sinusoidal displacements is given by the following:

$$M^*_{biphasic}(\omega^*) = \left(\frac{c_{11} - c_{12}}{2}\right)\frac{c_1\sqrt{i\omega^*}J_0(\sqrt{i\omega^*}) - c_2c_0J_1(\sqrt{i\omega^*})}{\sqrt{i\omega^*}J_0(\sqrt{i\omega^*}) - c_0J_1(\sqrt{i\omega^*})} \tag{7.12}$$

where J_0 and J_1 are modified Bessel functions of the first kind and c_{11}, c_{12}, c_1, c_2 and c_0 are derived from material constants and are specified in Cohen et al. [27]. The biphasic

complex modulus was obtained from the stress-strain formulation in Laplace space, which was given by Cohen as:

$$\bar{\sigma}(s) = \bar{\varepsilon}(s)\bar{M}^*(s) \tag{7.13}$$

where $\bar{M}^*(s)$ evaluated at s=iω* yields Equation 7.12 [29]. Using a similar logic, the complex modulus for an isotropic poroviscoelastic cylinder subjected to unconstrained sinusoidal displacement can be found from the formulation of Mak et al. [25]:

$$M^*_{porovisco}(\omega^*) = \mu\left(1 + cLog\left[\frac{1+i\omega^*\tau_2}{1+i\omega^*\tau_1}\right]\right)\left(\frac{3\sqrt{\alpha}J_0(\sqrt{\alpha}) - 8\Delta J_1(\sqrt{\alpha})}{\sqrt{\alpha}J_0(\sqrt{\alpha}) - 2\Delta J_1(\sqrt{\alpha})}\right) \tag{7.14}$$

In this equation, the following parameters are defined:

$$g = \frac{1}{i\omega^*}\left(1 + cLog\left[\frac{1+i\omega^*\tau_2}{1+i\omega^*\tau_1}\right]\right) \tag{7.15}$$

$$\gamma = \frac{2(1-2\nu)}{3(1-\nu)} \tag{7.16}$$

$$\alpha = \frac{i\omega^*}{1-\gamma+i\omega^*\gamma g} \tag{7.17}$$

$$\Delta = \left(\frac{1-2\nu}{2(1-\nu)}\right)\left(\frac{1 + cLog\left[\frac{1+i\omega^*\tau_2}{1+i\omega^*\tau_1}\right]}{1+\gamma cLog\left[\frac{1+i\omega^*\tau_2}{1+i\omega^*\tau_1}\right]}\right) \tag{7.18}$$

where the lame coefficients (μ,Λ) and the aggregate modulus (H_a) are defined as:

$$\mu = \frac{E}{2(1+\nu)} \tag{7.19}$$

$$\Lambda = \frac{E\nu}{(1+\nu)(1-2\nu)} \tag{7.20}$$

$$H_a = \Lambda + 2\mu \tag{7.21}$$

In these equations, E is the Young's modulus and ν is the Poisson's ratio. Note that in the biphasic and poroviscoelastic solutions (Equations 7.12-7.19), the frequency is nondimensionalized. To obtain the actual frequency (rad/sec), the following transformation is used:

$$\omega = \frac{\omega^*}{\left(\frac{H_a k}{r^2}\right)} \tag{7.22}$$

where k is the isotropic permeability and r is the cylinder radius. To obtain the phase shift (δ) and the dynamic modulus (d), the following relations are used:

$$d = |G| \tag{7.23}$$

$$\delta = \arctan\left[\frac{\mathrm{Im}(G)}{\mathrm{Re}(G)}\right] \tag{7.24}$$

Nonlinear curve fits were performed simultaneously on previously published data for the phase angle and dynamic modulus [26] for the QLV formulation, the biphasic formulation and the poroviscoelastic formulation using a constrained nonlinear

optimization routine ("fmincon") in Matlab. Curve fits using the QLV model and the transversely isotropic biphasic model produced identical results and a poor fit of the data (Fig 7.2). Although it was an isotropic model with a cylindrical cross section, the poroviscoelastic fits were considerably better (Fig 7.2), suggesting that a more realistic model with transverse isotropy and a rectangular cross section may be capable of fully predicting the experimentally observed dynamic modulus and phase shift for ligament tissue samples.

3D microscopy of fascicle microstructure

A long standing challenge has been understanding the precise organization within fibers and fascicles. SEM studies have attempted to track single fibrils. However such

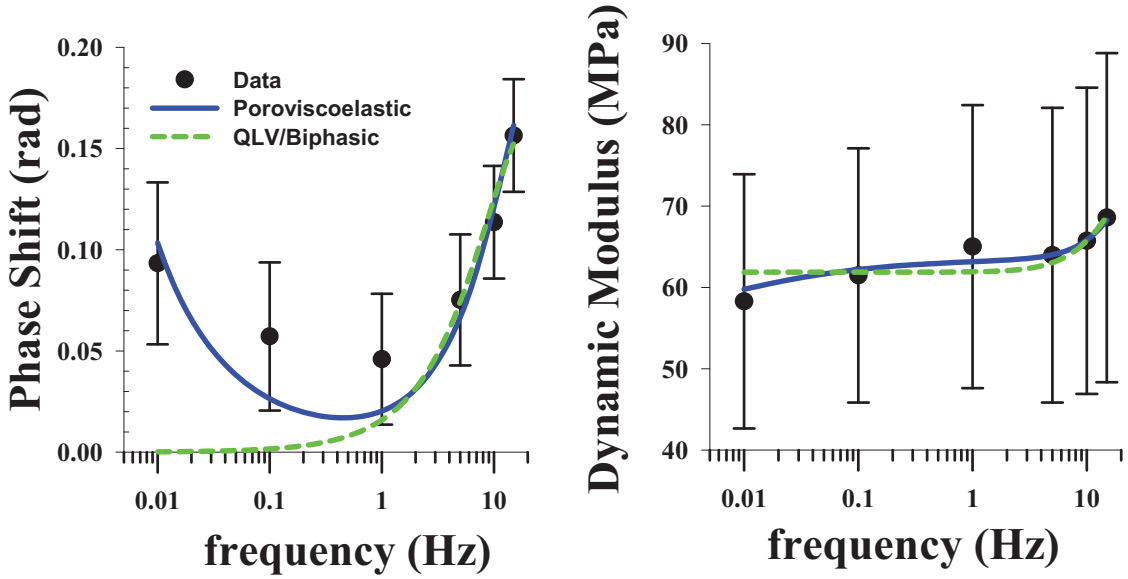

Figure 7.2: Poroviscoelastic curve fits. The QLV and biphasic curve fits (dotted green line) were identical and provided poor fits of the experimentally measured phase shift (Left) and the dynamic modulus (Right) of ligament. The isotropic poroviscoelastic model (solid blue line) provided a much better fit of the data.

studies are severely limited by the 2D nature of SEM [30]. The use of TEM and serial sectioning has been used, but obtaining an adequate number of slices to obtain a meaningful reconstruction is difficult [31]. A promising new technique known as focused ion beam milling scanning electron microscopy (FIB-SEM) utilizes a focused beam of gallium ions to serially section a sample. This provides a precise and automated method for obtaining 3D image data sets at the nanoscale. To demonstrate the feasibility of obtaining 3D imaging data of tendon fibril organization, FIB-SEM imaging was performed on a rat tail tendon fascicle. Tendon fascicles were isolated from rat tails, fixed in formalin and then postfixed with osmium tetroxide [32]. Fascicles were embedded in Spurr's resin and then attached to a cylindrical aluminum block using conductive adhesive tape. A fascicle was then imaged using a Quanta 3D dual beam FIB/SEM system (FEI; Hillsboro, Oregon) [33]. A total of 100 slices with a 20 nm spacing were imaged at 50,000X. The lowest voltage possible was used, as charging artifacts can be problematic for nonconductive samples. The resulting image stack was filtered using a tophat transformation to remove the background and then all images within the stack were aligned using an image registration algorithm. The final image stack was rendered using Amira 5.3 (Visage Imaging; San Diego, CA). Fibrils were clearly visible in the reconstructed 3D images from FIB-SEM imaging, revealing a complex organization of fibrils within a rat tail tendon fiber (Fig 7.3 left). The fibrils were predominantly oriented parallel to each other, yet fibril fusions, splitting and interweaving were visible. Previous studies using SEM have found it difficult to track 3D fibril trajectories [30], while serial sectioning studies have proven impractical for large scale analysis [31]. The FIB-SEM technique addresses both of these issues.

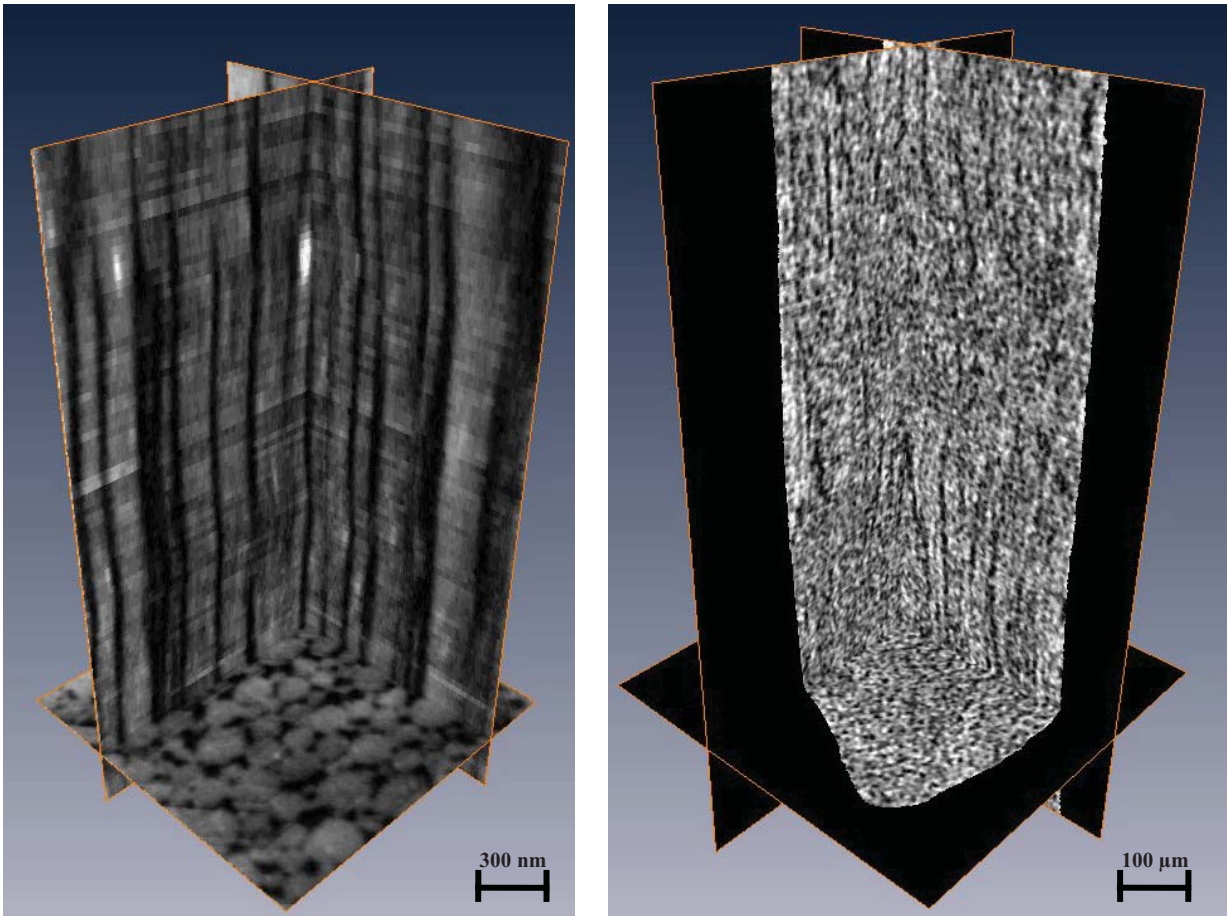

Figure 7.3: 3D microscopy of tendon. (Left) FIB-SEM yielded high resolution image stacks that clearly display the organization of fibrils within a fascicle. (Right) Although the contrast of the MicroCT was not nearly as good as the FIB-SEM, the organization of fibers can still be seen.

Studies utilizing confocal imaging techniques have been able to resolve 2D fiber organizations within fascicles. However, 3D reconstruction has proved problematic. This is primarily due to the strong scattering properties of collagen, which prevents the capture of high resolution images deep within fascicles. MicroCT technology may provide a means of obtaining 3D image sets that could be used to discern the organization of fibers within fascicles. To test the feasibility of this technique, MicroCT imaging was performed on a rat tail tendon fascicle. Tendon fascicles were stained with osmium tetroxide, placed in a pipette tip and embedded in agarose gel. The fascicles were imaged using an SKYSCAN1172 MicroCT imaging system (SKYSCAN, Kontich, Belgium). The voxels were square with an edge length of 630 nm and the FOV was 500×512×512 voxels. A Weiner filter was used to remove noise. Amira was used for 3D visualization. Although the contrast in this preliminary data set was low, individual fibers and crimp structures within the fascicle could be discerned (Fig 7.4 top). Stream traces of fiber organization were extracted from the 3D dataset using digital image correlation. Tracking the fiber organization within the 3D data sets revealed a number of different crimping patterns, ranging from nearly planar to helical (Fig 7.4 bottom). This clearly demonstrated that fiber organization within a fascicle is not two-dimensional, as is often assumed [17,81]. As observed in previous studies, the phase of the crimp was shifted from one side to the other [34, 35]. Operators of the MicroCT indicated that a more appropriate stain (e.g., phosphotungstic acid) may provide better contrast [36]. Although these data are preliminary, they strongly suggest that utilizing FIB-SEM and MicroCT will provide a new means for discerning the nanoscale and microscale structure of tendon and ligament.

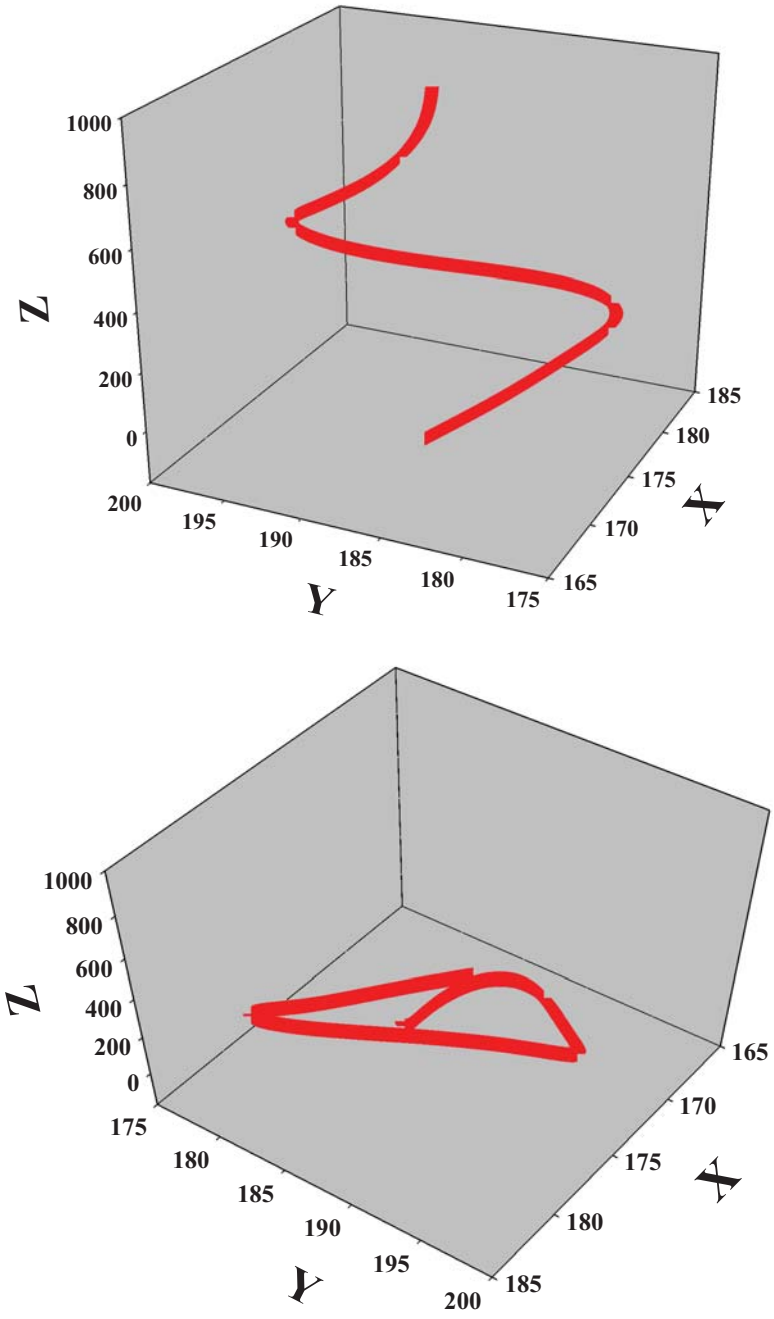

Figure 7.4: Three-dimensional fiber crimp. Fibers tracked within the MicroCT data set revealed complex 3D fiber organizations. A single fiber trajectory is shown from two perspectives. When viewed from the side, the classic crimp pattern is seen (Top). However, when viewed from the top, it becomes evident that the fiber crimp displays a helical organization (Bottom).

References

[1] Lujan, T. J., Underwood, C. J., Henninger, H. B., Thompson, B. M., and Weiss, J. A., 2007, "Effect of Dermatan Sulfate Glycosaminoglycans on the Quasi-Static Material Properties of the Human Medial Collateral Ligament," J Orthop Res, 25(7), pp. 894-903.

[2] Lujan, T. J., Underwood, C. J., Jacobs, N. T., and Weiss, J. A., 2009, "Contribution of Glycosaminoglycans to Viscoelastic Tensile Behavior of Human Ligament," J Appl Physiol, 106(2), pp. 423-31.

[3] Zhang, G., Ezura, Y., Chervoneva, I., Robinson, P. S., Beason, D. P., Carine, E. T., Soslowsky, L. J., Iozzo, R. V., and Birk, D. E., 2006, "Decorin Regulates Assembly of Collagen Fibrils and Acquisition of Biomechanical Properties During Tendon Development," J Cell Biochem, 98(6), pp. 1436-49.

[4] Ruhland, C., Schonherr, E., Robenek, H., Hansen, U., Iozzo, R. V., Bruckner, P., and Seidler, D. G., 2007, "The Glycosaminoglycan Chain of Decorin Plays an Important Role in Collagen Fibril Formation at the Early Stages of Fibrillogenesis," Febs J, 274(16), pp. 4246-55.

[5] Wallace, J. M., Rajachar, R. M., Chen, X. D., Shi, S., Allen, M. R., Bloomfield, S. A., Les, C. M., Robey, P. G., Young, M. F., and Kohn, D. H., 2006, "The Mechanical Phenotype of Biglycan-Deficient Mice Is Bone- and Gender-Specific," Bone, 39(1), pp. 106-16.

[6] Freed, A. D., and Doehring, T. C., 2005, "Elastic Model for Crimped Collagen Fibrils," J Biomech Eng, 127(4), pp. 587-93.

[7] Grytz, R., and Meschke, G., 2009, "Constitutive Modeling of Crimped Collagen Fibrils in Soft Tissues," J Mech Behav Biomed Mater, 2(5), pp. 522-33.

[8] Hurschler, C., 1997, "A Structurally Based Stress-Stretch Relationship for Tendon and Ligament," Journal of Biomechanical Engineering, 119(4), pp. 392-399.

[9] Lanir, Y., 1980, "A Microstructure Model for the Rheology of Mammalian Tendon," Journal of Biomechanical Engineering, 102, pp. 332-339.

[10] Vidal, B. C., 1995, "Crimp as Part of a Helical Structure," C R Acad Sci III, 318(2), pp. 173-8.

[11] Yahia, L. H., and Drouin, G., 1989, "Microscopical Investigation of Canine Anterior Cruciate Ligament and Patellar Tendon: Collagen Fascicle Morphology and Architecture," J Orthop Res, 7(2), pp. 243-51.

[12] Kanouté, P., Boso, D., Chaboche, J., and Schrefler, B., 2009, "Multiscale Methods for Composites: A Review," Archives of Computational Methods in Engineering, 16(1), pp. 31-75.

[13] Yin, L., and Elliott, D. M., 2004, "A Biphasic and Transversely Isotropic Mechanical Model for Tendon: Application to Mouse Tail Fascicles in Uniaxial Tension," J Biomech, 37(6), pp. 907-16.

[14] Banos, C. C., Thomas, A. H., and Kuo, C. K., 2008, "Collagen Fibrillogenesis in Tendon Development: Current Models and Regulation of Fibril Assembly," Birth Defects Res C Embryo Today, 84(3), pp. 228-44.

[15] Haraldsson, B. T., Aagaard, P., Qvortrup, K., Bojsen-Moller, J., Krogsgaard, M., Koskinen, S., Kjaer, M., and Magnusson, S. P., 2008, "Lateral Force Transmission between Human Tendon Fascicles," Matrix Biol, 27(2), pp. 86-95.

[16] Komolafe, O. A., and Doehring, T. C., 2010, "Fascicle-Scale Loading and Failure Behavior of the Achilles Tendon," J Biomech Eng, 132(2), pp. 021004.

[17] Kannus, P., 2000, "Structure of the Tendon Connective Tissue," Scand J Med Sci Sports, 10(6), pp. 312-20.

[18] Ault, H. K., and Hoffman, A. H., 1992, "A Composite Micromechanical Model for Connective Tissues: Part Ii - Application to Rat Tail Tendon and Joint Capsule," Journal of Biomechanical Engineering, 114(1), pp. 142-146.

[19] Hurschler, C., Loitz-Ramage, B., and Vanderby, R., Jr., 1997, "A Structurally Based Stress-Stretch Relationship for Tendon and Ligament," Journal of Biomechanical Engineering, 119(4), pp. 392-9.

[20] Elliott, D. M., and Setton, L. A., 2001, "Anisotropic and Inhomogeneous Tensile Behavior of the Human Anulus Fibrosus: Experimental Measurement and Material Model Predictions," J Biomech Eng, 123(3), pp. 256-63.

[21] Bonet, J., and Wood, R., 1997, *Nonlinear Continuum Mechanics for Finite Element Analysis*, Cambridge University Press, Cambridge, England.

[22] Spencer, A. J. M., 1980, *Continuum Mechanics*, Dover Publications, New York, NY.

[23] Weiss, J. A., France, E. P., Bagley, A. M., and Blomstrom, G., 1992, "Measurement of 2-D Strains in Ligaments under Uniaxial Tension," Trans 38th Meeting Orthop Res Soc, 17(2), pp. 662.

[24] Huang, C. Y., Mow, V. C., and Ateshian, G. A., 2001, "The Role of Flow-Independent Viscoelasticity in the Biphasic Tensile and Compressive Responses of Articular Cartilage," J Biomech Eng, 123(5), pp. 410-7.

[25] Mak, A. F., 1986, "Unconfined Compression of Hydrated Viscoelastic Tissues: A Biphasic Poroviscoelastic Analysis," Biorheology, 23(4), pp. 371-83.

[26] Bonifasi-Lista, C., Lake, S. P., Small, M. S., and Weiss, J. A., 2005, "Viscoelastic Properties of the Human Medial Collateral Ligament under Longitudinal, Transverse and Shear Loading," J Orthop Res, 23(1), pp. 67-76.

[27] Cohen, B., Lai, W. M., and Mow, V. C., 1998, "A Transversely Isotropic Biphasic Model for Unconfined Compression of Growth Plate and Chondroepiphysis," J Biomech Eng, 120(4), pp. 491-6.

[28] Luo, R., and Lytton, R. L., 2010, "Characterization of the Tensile Viscoelastic Properties of an Undamaged Asphalt Mixture," Journal of Transportation Engineering, 136(3), pp. 173-80.

[29] Huang, C. Y., Soltz, M. A., Kopacz, M., Mow, V. C., and Ateshian, G. A., 2003, "Experimental Verification of the Roles of Intrinsic Matrix Viscoelasticity and Tension-Compression Nonlinearity in the Biphasic Response of Cartilage," J Biomech Eng, 125(1), pp. 84-93.

[30] Provenzano, P. P., and Vanderby, R., Jr., 2006, "Collagen Fibril Morphology and Organization: Implications for Force Transmission in Ligament and Tendon," Matrix Biol, 25(2), pp. 71-84.

[31] Birk, D. E., Southern, J. F., Zycband, E. I., Fallon, J. T., and Trelstad, R. L., 1989, "Collagen Fibril Bundles: A Branching Assembly Unit in Tendon Morphogenesis," Development, 107(3), pp. 437-43.

[32] Iwasaki, S., Hosaka, Y., Iwasaki, T., Yamamoto, K., Nagayasu, A., Ueda, H., Kokai, Y., and Takehana, K., 2008, "The Modulation of Collagen Fibril Assembly and Its Structure by Decorin: An Electron Microscopic Study," Arch Histol Cytol, 71(1), pp. 37-44.

[33] Knott, G., Marchman, H., Wall, D., and Lich, B., 2008, "Serial Section Scanning Electron Microscopy of Adult Brain Tissue Using Focused Ion Beam Milling," The Journal of Neuroscience, 28(12), pp. 2959-64.

[34] Kastelic, J., Galeski, A., and Baer, E., 1978, "The Multicomposite Structure of Tendon," Connect Tissue Res, 6(1), pp. 11-23.

[35] Niven, H., Baer, E., and Hiltner, A., 1982, "Organization of Collagen Fibers in Rat Tail Tendon at the Optical Microscope Level," Coll Relat Res, 2(2), pp. 131-42.

[36] Metscher, B., 2009, "Microct for Comparative Morphology: Simple Staining Methods Allow High-Contrast 3d Imaging of Diverse Non-Mineralized Animal Tissues," BMC Physiology, 9(1), pp. 11.

APPENDIX A

PERIODIC BOUNDARY CONDITIONS FOR FE UNIT CELLS FEATURING HEXAGONAL GEOMETRY AND HELICAL COORDINATE SYSTEMS

Periodic boundary conditions state that opposing faces must deform identically. Enforcing these boundary conditions on a finite element mesh requires the application of linear constraints on the boundary nodes, which must be identical in number and placement between opposing faces. For the nodal displacements u_i on the faces (i=1,2,3), the nodal displacements e_i on the edges and the nodal displacements c_i on the corners, the following linear constraints were applied:

$$u_i^+ - u_i^{c_1^+} = u_i^- - u_i^{c_1^-} \tag{A 1}$$

$$e_i^+ - \eta_i \cdot u_i^{c_1^+} - \eta_i \cdot u_i^{c_2^+} = e_i^- - \eta_i \cdot u_i^{c_1^-} - \eta_i \cdot u_i^{c_2^+} \tag{A 2}$$

$$c_i^+ - \eta_i \cdot u_i^{c_1^+} - \eta_i \cdot u_i^{c_2^+} - \eta_i \cdot c_i^{c_3^+} = u_i^- - \eta_i \cdot u_i^{c_1^-} - \eta_i \cdot u_i^{c_2^+} \quad - \eta_i \cdot c_i^{c_3^+} \tag{A 3}$$

To allow for rigid body motion between each face pair, the nodal displacements for the faces (u_i^+ and u_i^-) were subtracted from the center node of each face (u_i^{c1+} and u_i^{c1-}). Likewise, to allow for rigid body motion between each edge pair the nodal displacements for the edges (e_i^+ and e_i^-) were subtracted from the center nodes of each corresponding face that the edge node shared (u_i^{c1+}, u_i^{c2+} and u_i^{c1-}, u_i^{c2-}). Finally, to allow for rigid body

motion between each corner pair the nodal displacement for the corner (c_i^+ and c_i^-) was subtracted from the displacements of the center node for each corresponding face the corner node shared (u_i^{c1+}, u_i^{c2+}, u_i^{c3+} and u_i^{c1-}, u_i^{c2-},u_i^{c3-}). This is shown schematically in Fig A.1. In these equations η_i is a geometry-dependent weighting factor given by

$$\eta_i = \frac{1}{\cos^2\left(\beta_i - 90\right)} \tag{A 4}$$

where $\beta_1 = \beta_2 = 120^o$ and $\beta_3 = 90^o$ for the hexagonal edges in the x-y plane and $\beta_1 = \beta_2 = \beta_3 = 90^o$ for the square edges in the y-z and x-z plane. To our knowledge this formulation of periodic boundary conditions for hexagonally shaped representative volume elements has not been reported in the literature.

For the case of helically transformed models, the nodal displacements were converted to a helical coordinate system described by the following transformation:

$$\begin{bmatrix} \tilde{u}_x \\ \tilde{u}_y \\ \tilde{u}_z \end{bmatrix} = \begin{bmatrix} \cos\left[\theta(\mathrm{z})\right] & -\sin\left[\theta(\mathrm{z})\right] & 0 \\ \sin\left[\theta(\mathrm{z})\right] & \cos\left[\theta(\mathrm{z})\right] & 0 \\ 0 & 0 & 1 \end{bmatrix} \begin{bmatrix} u_x \\ u_y \\ u_z \end{bmatrix} \tag{A 5}$$

where $\theta(\mathrm{z})$ is the transformation angle along the fiber direction given by equation:

$$\theta(\mathrm{z}) = \frac{z}{R \cdot \tan(\alpha)} \tag{A 6}$$

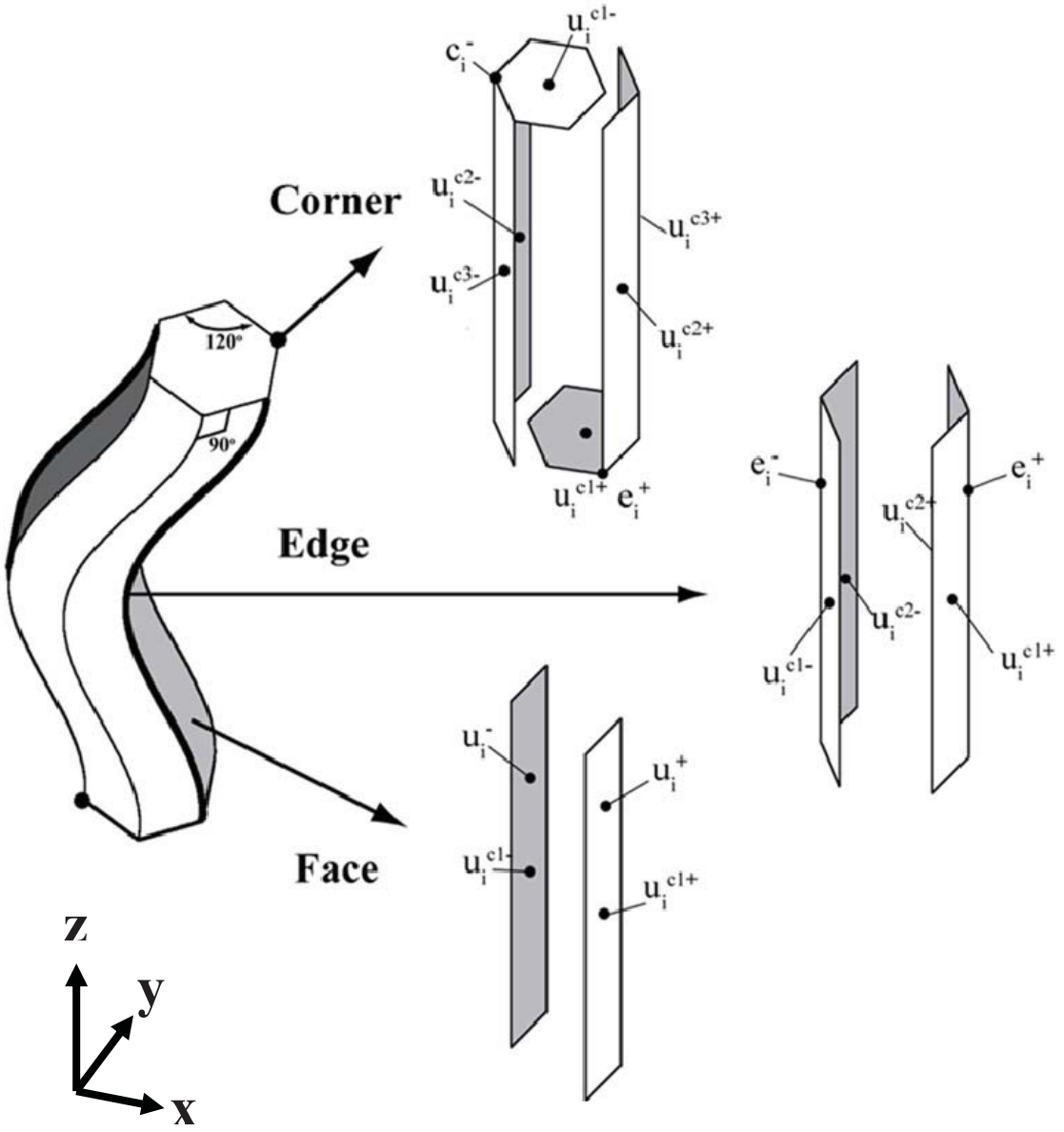

Figure A.1: Periodic boundary conditions. Linear constraints were defined for the boundary nodes such that rigid body motion was allowed between opposing faces, edges and corners. The model on the left shows an opposing face pair (shaded faces), opposing edge pair (edges with a bold line) and an opposing corner pair (large dot) of a crimped fiber model. Arrows point from the face, edge or corner to a schematic of a straight fiber that shows the center nodes that were used in formulating the linear constraints. Note that these constraints were applied to the four face pairs, nine edge pairs and six corner pairs of the hexagonally shaped models.

in which R is the radius, α is the helical pitch and z is the position along the length of the model. It should be noted that the application of the helical transformation removes the periodicity of the model, meaning that it will not repeat itself under simple translations.

There are several practical consequences of applying periodic boundary conditions to the helically transformed models. After transformation into helical coordinates, opposing faces follow the helical twist of the fibrils. The consequence of this is that more lateral strain is to be expected relative to a fully periodic model. The helical rotation does not affect the periodicity in the axial direction. Therefore an infinitely long helical structure is simulated.

The above boundary conditions were verified by running models with homogenous material properties for all elements. Briefly, a model with a full helical twist (2π) and a model with a full helical twist superimposed on a full crimp (a single period) were subjected to uniaxial strain in combination with the helically transformed periodic boundary conditions. The resulting simulations revealed a constant stress and strain throughout all elements. The strain energy was volume averaged throughout the models and found to equal the strain energy computed from the applied displacements and resulting reaction forces, thus indicating that the Hill principle was not violated. This is an important result, as it reveals that a helical transformation of the periodic boundary conditions yields a valid set of boundary conditions when computing the apparent material properties of a helically twisted unit cell.

APPENDIX B

GEL AND FIBER CONSTITUTIVE MODEL AND CURVE FITTING

A constitutive model featuring an elliptical fiber distribution (EFD) embedded within a matrix material was used to describe the mechanical behavior of the collagen gels and extruded fibers [1]. In this formulation, the Cauchy stress is defined as the sum of the fiber and matrix contributions:

$$\boldsymbol{\sigma} = \boldsymbol{\sigma}^f + \boldsymbol{\sigma}^m \tag{B 1}$$

Both stress terms are defined in using a strain energy function:

$$\boldsymbol{\sigma}^f = \int_0^{2\pi}\int_0^{\pi} H\left(\lambda_n - 1\right) 2J^{-1}\mathbf{F}\frac{\partial W^f}{\partial \mathbf{C}}\mathbf{F}^T \sin\phi d\phi d\theta \tag{B 2}$$

$$\boldsymbol{\sigma}^m = 2J^{-1}\mathbf{F}\frac{\partial W^m}{\partial \mathbf{C}}\mathbf{F}^T \tag{B 3}$$

where the fiber stress requires an integration over a unit sphere. The strain energy functions are defined as:

$$W^f\left(\mathbf{n}^r, \lambda_n^2\right) = \xi\left(\mathbf{n}^r\right)\left(\lambda_n^2 - 1\right)^{\alpha\left(\mathbf{n}^r\right)} \tag{B 4}$$

$$W^m\left(I_1\right) = \frac{E}{2\left(1+\nu\right)}\left(I_1 - 3\right) \tag{B 5}$$

The fiber stretch, λ, is defined as:

$$\lambda_n^2 = \mathbf{n}^r \mathbf{C} \mathbf{n}^r$$

where **C** is the right Cauchy deformation tensor and $\mathbf{n}^r$ is the major axis of the elliptical fiber distribution, which determines the fiber modulus ξ and the power law coefficient α:

$$\xi\left(\mathbf{n}^r\right) = \left(\frac{\cos(\Theta)^2 \sin(\Phi)^2}{\xi_1^2} + \frac{\sin(\Theta)^2 \sin(\Phi)^2}{\xi_2^2} + \frac{\cos(\Phi)^2}{\xi_3^2} \right)^{-1/2} \tag{B 6}$$

$$\alpha\left(\mathbf{n}^r\right) = \left(\frac{\cos(\Theta)^2 \sin(\Phi)^2}{\alpha_1^2} + \frac{\sin(\Theta)^2 \sin(\Phi)^2}{\alpha_2^2} + \frac{\cos(\Phi)^2}{\alpha_3^2} \right)^{-1/2} \tag{B 7}$$

and

$$\mathbf{n}^r = \cos\Theta \sin\Phi \mathbf{a}_1 + \sin\Theta \sin\Phi \mathbf{a}_2 + \cos\Theta \mathbf{a}_3 \tag{B 8}$$

A coordinate transformation must be made between the local coordinate basis ($\mathbf{a}_i$) and the global basis ($\mathbf{e}_i$) to relate (Φ,Θ) and (ϕ,θ). Note that the coefficients α_1, α_2, α_3 and ξ_1, ξ_2, ξ_3 represent the major and minor axis of an ellipsoidal distribution (Fig B.1). Because of the Heaviside function, $H(\lambda_n - 1)$, the fibers only contribute in tension. The model has a total of eight coefficients: E, ν, α_1, α_2, α_3, ξ_1, ξ_2 and ξ_3. Note that the coefficients *E* and *v* are redundant, as the term $\frac{E}{2(1+v)}$ in the matrix strain energy function is actually the shear modulus. Therefore, the matrix Poisson's ratio ν can be set to zero and *E* will remain as the only independent matrix coefficient. Further simplifications can be made if information is known regarding the fiber distributions for the material. SEM imaging of

collagen gels reveals an isotropic distribution of fibrils (Fig B.2). The precise organization of the gel can be obtained by finding the angular fiber distribution via the use of a polar FFT [2]. The anisotropy of SEM images of collagen gels ranged between 0.05-0.15, indicating a nearly random distribution (Fig B.2). Given this assumption, the power law coefficients can be set equal: $\alpha_{1=}\ \alpha_{2=}\ \alpha_{3=}\ \alpha_{gel}$. Similarly, the fiber modulus coefficients can be set equal: $\xi_1 = \xi_2 = \xi_3 = \xi_{gel}$. Thus, for the collagen gel, three unique coefficients must be determined: E_{gel}, α_{gel}, and ξ_{gel}. For the extruded collagen fiber, FFT analysis of SEM images revealed an anisotropic fiber distribution (Fig B.2), in which the anisotropy ranges between 0.6-0.8. The ratio of the major and minor axis of these fiber distributions is ~4. Thus, the ξ coefficients were given a transversely isotropic distribution, $\xi_{1=}\ \xi_{2=}\ \xi_{xy}$, $\xi_z = 4\xi_{xy}$. The power law coefficients were taken to be isotropic, $\alpha_{1=}\ \alpha_{2=}\ \alpha_{3=}\ \alpha_{fiber}$. As with the gels, for the extruded fibers, a total of 3 unique coefficients must be found. A nonlinear, constrained global optimization routine (a pattern search algorithm) was implemented in Matlab that found the coefficients that minimized the sum of squares difference between the experimental curves and the fit curves. Two data sets were simultaneously used for the curve fits: stress-strain data and axial strain-transverse strain (the 2D) data. The fit results were relatively insensitive to the starting values. Curve fits were performed on the test data for each individual fiber and gel, as well as for the average test data. Table B2 shows the fit parameters and the R^2 values.

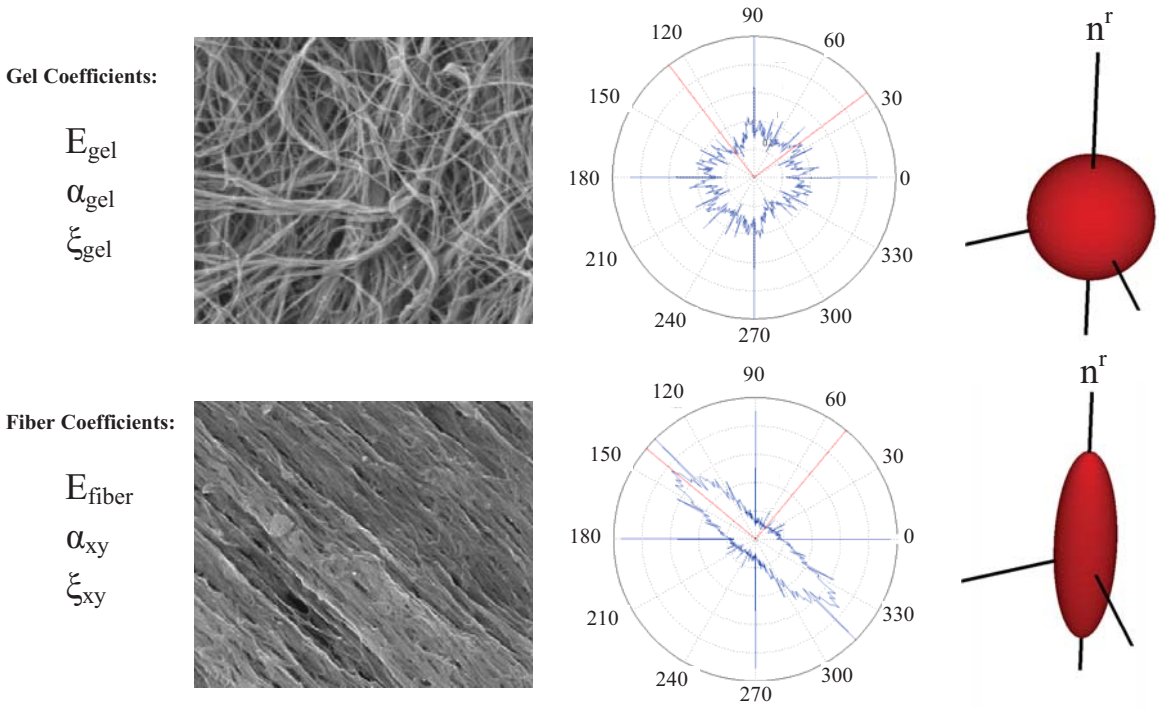

Figure B.2: EFD constitutive model. Three unique coefficients were needed to describe the gel and fiber behavior (Far left). SEM imaging revealed a random orientation of fibrils within gels (Top, center left) and an aligned orientation within fibers (Bottom, center left). FFT analysis was used to generate polar plots of the fiber distribution as well as the magnitude of the minor and principle axis. For the collagen gels, the ratio of the major to minor principle axis was nearly 1 (Top, center right), which is consistent with the assumption of a spherical fiber distribution (Top, far right). For the extruded fibers, the ratio of the major axis to the minor axis was approximately 4:1 (Bottom, center right), which is consistent with the assumption of an elliptical fiber distribution (Top, far right). The local fiber direction, $\mathbf{n}^r$, is shown on the fiber distribution plots.

Table B.1: EFD best fit coefficients. The best fit coefficients for the gel and fiber are given to three significant figures. Note that the parameter ξ_z was not independently fit, but rather computed from ξ_{xy}.

Fit	**E**	**α**	ξ_{xy}	ξ_z	R^2
Gel	0.00160±.00060	3.02±.093	0.136±0.096	0.136±0.096	0.98
Fiber	2.67±1.79	2.24±.042	18.8±3.05	75.2±12.2	0.99

APPENDIX C

DERIVATION OF THE STRESS FOR THE NEW VOLUMETRIC STRAIN ENERGY FUNCTION OF LIGAMENT

The full strain energy function presented in Chapter 7 is:

$$W = W_{fiber} + W_{matrix} + W_{volume} \tag{C 1}$$

$$W_{fiber} = \frac{1}{2}\frac{c_1}{c_2}\left(e^{c_2\left(\sqrt{I_4}-1\right)^2} - 1 \right) \tag{C 2}$$

$$W_{matrix} = \frac{\mu}{2}\left(I_1 - 3\right) - \mu Log\left(\sqrt{I_3}\right) + \frac{\lambda}{2} Log\left(\sqrt{I_3}\right)^2 \tag{C 3}$$

$$W_{volume} = \ln\left[\frac{\left(I_5 - I_1 I_4 + I_2\right)}{\left(1 - v_{31}\left(\sqrt{I_4}\right)\left(\sqrt{I_4}-1\right)\right)^4} \right]^2 \tag{C 4}$$

where $\mathbf{e}_1$ is the initial fiber axis and $v_{31}\left(\sqrt{I_4}\right)$ was given a linear form:

$$v_{31}\left(\sqrt{I_4}\right) = m\left(\sqrt{I_4}-1\right) + v_0 \tag{C 5}$$

The Cauchy stress is found by taking the push forward of the first derivative of the strain energy function with respect to the right Cauchy deformation tensor:

$$\boldsymbol{\sigma} = \chi^* \left(2 \frac{\partial W}{\partial \mathbf{C}} \right) \tag{C 6}$$

in which $W = W\left(I_1, I_2, I_3, I_4, I_5\right)$ and the push forward operator on the contravariant 2nd Piola Kirchoff stress tensor is:

$$\chi^*(\ ) = \frac{1}{J} \mathbf{F}(\ ) \mathbf{F}^t \tag{C 7}$$

Note that $J = \sqrt{I_3}$. This derivative can be found using the chain rule:

$$\frac{\partial W}{\partial \mathbf{C}} = \sum_{m=1}^{5} W_m \cdot \chi^* \left(\frac{\partial I_m}{\partial \mathbf{C}} \right) \tag{C 8}$$

where W_m is the derivative of W with respect to the invariant I_m. The invariant derivatives and their push forwards are:

$$\chi^* \left(\frac{\partial I_1}{\partial \mathbf{C}} \right) = \frac{1}{J} \mathbf{b} \tag{C 9}$$

$$\chi^* \left(\frac{\partial I_2}{\partial \mathbf{C}} \right) = \frac{1}{J} \left(I_1 \mathbf{b} - \mathbf{b}^2 \right) \tag{C 10}$$

$$\chi^* \left(\frac{\partial I_3}{\partial \mathbf{C}} \right) = \frac{1}{J} I_3 \mathbf{I} \tag{C 11}$$

$$\chi^* \left(\frac{\partial I_4}{\partial \mathbf{C}} \right) = \frac{1}{J} I_4 \left(\mathbf{a} \otimes \mathbf{a} \right) \tag{C 12}$$

$$\chi^* \left(\frac{\partial I_5}{\partial \mathbf{C}} \right) = \frac{1}{J} I_4 \left(\mathbf{a} \otimes \mathbf{ba} + \mathbf{ba} \otimes \mathbf{a} \right) \tag{C 13}$$

In these equations the symbol $\otimes$ represents an outer product. The final expression for the Cauchy stress is then:

$$\boldsymbol{\sigma} = \frac{2}{J}\left[I_3 W_3 \mathbf{I} + \left(W_1 + I_1 W_2\right)\mathbf{b} - W_2 \mathbf{b}^2 + I_4 W_4 \left(\mathbf{a}\otimes\mathbf{a}\right) + I_4 W_5 \left(\left(\mathbf{a}\otimes\mathbf{ba} + \mathbf{ba}\otimes\mathbf{a}\right)\right)\right] \tag{C 14}$$

Prior to defining the derivatives, the following constants are defined:

$$A_r = I_2 - I_1 I_4 + I_5 \tag{C 15}$$

$$\lambda = \sqrt{I_4} \tag{C 16}$$

$$\varepsilon_\lambda = \lambda - 1 \tag{C 17}$$

$$\nu\left(\lambda\right) = \left(\lambda - 1\right) m + \nu_0 \tag{C 18}$$

$$\Sigma = Log\left(\frac{A_r}{\left[\varepsilon_\lambda \nu\left(\lambda\right) - 1\right]^4} \right) \tag{C 19}$$

where A_r is the area ratio perpendicular to the fiber direction **a**, λ is the fiber stretch, ε_r is the engineer strain in the fiber direction, $\nu(\lambda)$ is the linear Poisson's function and Σ is the volumetric penalty term, which enforces the Poisson's ratio. The derivatives W_m are:

$$W_1 = \frac{\mu}{2} - \frac{2}{A_r}\lambda^2 \Sigma \tag{C 20}$$

$$W_2 = \frac{2\Sigma}{A_r} \tag{C 21}$$

$$W_3 = \frac{1}{4 I_3}\left(\Lambda Log\left[I_3\right] - 2\mu\right) \tag{C 22}$$

$$W_4 = c_1 \varepsilon_r e^{c_2 \varepsilon_r^2} - \frac{2\Sigma\left[2A_r \nu(\lambda) + I_1 \lambda\left(\varepsilon_r \nu(\lambda) - 1\right)\right]}{A_r \lambda\left[\varepsilon_r \nu(\lambda) - 1\right]} \quad \text{(C 23)}$$

$$W_5 = \frac{2\Sigma}{A_r} \quad \text{(C 24)}$$

References

[1] Ateshian, G. A., Rajan, V., Chahine, N. O., Canal, C. E., and Hung, C. T., 2009, "Modeling the Matrix of Articular Cartilage Using a Continuous Fiber Angular Distribution Predicts Many Observed Phenomena," J Biomech Eng, 131(6), pp. 061003.

[2] Chang, C. C. K., L; Nunes, S S; Church, K H; Edgar, L T; Boland, E D; Weiss, J a; Williams, S K; Hoying, J B 2011, "Determinants of Microvascular Network Topology in Implanted Neovasculatures," Arteriosclerosis, Thrombosis, and Vascular Biology, 32(1), pp. 5-14.